

**Textural and mineralogical characterization of
the late Pliensbachian–early Toarcian sediments
of the Cleveland Basin, Yorkshire, U.K.**

René de Vos

Abstract

The compositional characteristics of shales are inherently variable and the governing controls and depositional processes resulting in different facies can be expressed by the texture and mineralogy of sediments. The development of quartz grain size and mineralogy over the late Pliensbachian–early Toarcian shale succession of the Cleveland Basin is investigated using Scanning Electron Microscopy combined with Energy Dispersive X-ray analysis (SEM-EDX) to determine the distribution and overall content of quartz grains, while the clay mineral composition, in both qualitative and (semi-) qualitative sense, is determined by X-ray diffraction analysis (XRD). Due to the small grain size and difficulties of processing well cemented shales, no full evaluation of quartz grain size distributions over the course of the entire succession, and their relationship to the clay mineralogy, has ever been established. The results indicate that the current lithostratigraphic subdivisions yield no resemblance to the variability of the sedimentological properties of the shales, as determined on basis of quartz grain size distributions and clay mineralogy.

Contents

1. Introduction	4
2. Geological setting	4
2.1 General background: Early Jurassic regional evolution	4
2.2 Cleveland basin – structural setting	5
2.3 Stratigraphic framework	8
2.4 Paleoenvironmental setting	10
3. Materials and Methods	12
3.1 Rationale	12
3.2 Quartz silt analysis – sample preparation	13
3.3 Quartz silt analysis – acquisition and image analysis	13
3.4 Quartz silt analysis – statistical processing	15
3.5 Clay mineralogy – XRD sample preparation	16
3.6 Clay mineralogy – XRD measurements and interpretation	17
3.7 Clay mineralogy – quantifying relative abundances	17
4. Results	20
4.1 Grain size measurements from image analysis	20
4.2 Grain size distributions – Statistical analysis	22
4.3 Clay mineralogy – qualitative determination	23
4.3 Clay mineralogy – quantitative analysis	25
5. Discussion	27
5.1 Grain size distributions – process and reliability	27
5.2 On the determination of grain size parameters by moments	28
5.3 Clay mineralogy – notes on qualitative analysis	30
5.4 Clay mineralogy – notes on quantitative analysis	30
5.5 Provenance of quartz grains	31
5.6 Origin of clay mineral assemblage	33
5.7 Quartz content and clay mineralogy versus geochemistry	34
5.8 Paleoclimate interpretation from clay mineralogy	36
5.9 Depositional environment and sequence stratigraphic perspectives	37
6. Conclusion	41
7. References	42
8. Appendices	52
8.1 Appendix A – key to Figure 1	52
8.2 Appendix B – SEM images	53
8.3 Appendix C – Grain size distributions	64
8.4 Appendix D – XRD patterns	75
8.5 Appendix E – Summary of results	83

1. Introduction

The Cleveland Basin, located in NE England, is home to the excellent exposures of the Yorkshire coast, renowned for its fossils and Jurassic sediments. The late Pliensbachian–early Toarcian succession exposed along these shores is one of the most complete stratigraphic records of Early Jurassic sediments in Europe, and, as such, has been studied extensively (Powell 2010). A major environmental perturbation occurred during this interval, documented by a pronounced (c. -7‰) carbon isotope excursion combined with an extinction event (Little & Benton 1995; Little 1996), rapid warming of seawater (McArthur et al. 2000; Bailey et al. 2003; van de Schootbrugge et al. 2005), increased silicate weathering rates (Cohen et al. 2004), and elevated atmospheric CO₂ levels (McElwain et al. 2005). Closely associated to these perturbations are the organic-rich deposits of the Toarcian oceanic anoxic event (T-OAE) (Jenkyns 1988; Hesselbo et al. 2000), of which the ultimate causes remain highly controversial (e.g., Wignall et al. 2005; Gröcke et al. 2011). Due to the exceptional biostratigraphic control provided by ammonites, the late Pliensbachian–early Toarcian interval of the Cleveland Basin is one of the best successions available to enhance understanding of the responsible processes and the associated depositional environments.

The Lower Jurassic sediments of the studied interval consist mainly out of mudstones with incidental input of fine-grained sandstones and oölitic ironstones. Previous work on the same section focused on the inorganic geochemistry (Atar 2015), and serves as a comparative complement to this research, which targets the sedimentological properties of grain size and clay mineralogy. Overall, mudrocks contain 30% more detrital quartz than sandstones (Blatt 1970; Blatt & Schultz 1976), and its presence in pelitic sediments has been previously applied to indicate shoreline positions in epicontinental seas (Blatt & Totten 1981), as a record of relative sea-level change (Williams et al. 2001), and in terms of sequence stratigraphy (Macquaker & Taylor 1996; Macquaker et al. 1998). However, full grain size distributions have never been determined over the course of a complete section due to the difficulty in separating different constituents of shales (see section 3.1). This study therefore employs Scanning Electron Microscopy combined with Energy Dispersive X-ray analysis (SEM-EDX), to make in-situ measurements of the quartz grain size distribution, while the relative compositional abundance of the clay fraction is determined by XRD to combine both sedimentological (grain size) and climate (composition) derived properties of the shales.

Multiple studies have shown that there is great variability in the textural and compositional characteristics of shales, both vertically, through time, and laterally in space. The objective of this research is to determine the distribution of quartz grain size and clay mineralogy in shales to investigate and/or establish a link between the geochemical nature and texture of the sediments, and identify whether these parameters can be used to define the depositional environment of the late Pliensbachian–early Toarcian succession of European shales. The subsequent final goal of the study is, if different facies can be assigned according to variability present in the succession, to interpret these in terms of their depositional processes (local paleogeographic conditions) and controlling forcing mechanisms (tectonics, climate, and eustasy).

2. Geological Setting

2.1 General background: Early Jurassic regional evolution

During the Jurassic, Central and Northwestern Europe consisted of a variety of smaller basins which together constituted a system of shallow epeiric seas in the Peritethyan Realm. The sub-tropical paleogeographic position of the region during the Early Jurassic probably lay about 10° south of present latitudes, in an area of overlap of Tethyan and Boreal marine realms (Bradshaw et al. 1992). The region was connected to the northern Boreal Ocean and to the southern Tethys Ocean by the 'Hessian Seaway' and 'East Carpathian Gate', respectively, so that sedimentation during the Early Jurassic was influenced by both warm-water Tethyan inflow from the South and cold-water marginal-

marine Boreal influxes from the North (*Lott et al. 2010*). In the Late Triassic and Early Jurassic tectonic activity intensified along the Tethys–Central Atlantic–Caribbean rift/wrench system (*Ziegler 1990*), eventually leading to the breakup of the Pangean supercontinent during the Mid-Jurassic. Pre-existing faults and shear zones inherited from Variscan and Caledonian deformation phases governed to a large degree the configuration and development of the region's major structural trends during the Early Jurassic (*Simms et al. 2004; Doré et al. 1999*). Although major sedimentary basins developed due to the extensional stresses associated with the breakup of Pangea (*Simms et al. 2004*), the Early Jurassic was a period characterized by relative quiescent tectonic subsidence (*Doré et al. 1999; Lott et al. 2010*) and only minor volcanic activity (*Ziegler 1990*).

During the Early Jurassic large parts of Europe became flooded due to overall sea-level rise and continued subsidence, replacing arid Triassic deposits by large scale transgressive shallow to deep marine deposition, and resulting in late–Pliensbachian and Toarcian deposition dominated by shallow epeiric to mesopelagic sedimentation. Sedimentation during the Jurassic was controlled by extremely low slopes over large areas and characterized by facies belts of vast extent, dampened tidal range, few sediment gravity flows, and extensive storm influence in the setting of a wide-spread epicontinental sea which has no modern equivalent (*Hallam 1981a, 1997; Sellwood 1986*).

The consistent overall appearance of the paleo-environment and associated facies, suggests relatively constant conditions over the course of the Late Pliensbachian and successive Toarcian both in terms of climate and paleogeography. This conception initially led to the belief that the climate was consistently warm and appreciably more equable latitudinally than today (*Hallam 1975, 1985*). Present-day interpretations, however, fuelled by oxygen and carbon isotope data combined with elemental ratios (i.e., Sr/Ca, Mg/Ca, Na/Ca) from belemnites, bivalves, and brachiopods, suggest a substantially more variable climate. Sharp transitions between cold and hot 'events' (*Korte et al. 2015*), icehouse-greenhouse cycles (*Korte & Hesselbo 2011*), astronomically forced changes in climate (*Kemp et al. 2005a*), and a sudden 6–7 °C rise in seawater temperature (*Bailey et al. 2003*) have all been inferred for the late Pliensbachian–Toarcian interval.

A generic overview of Europe during the middle–Toarcian is provided by Figure 1 illustrating the controlling structural framework, paleogeographic distribution of landmasses and general depositional types during middle–Toarcian times in regard to present day coastlines in Early Jurassic configuration.

2.2 Cleveland basin – structural setting

Positioned at about 30° north of the equator during the late Pliensbachian (*Powell 2010*), the Cleveland Basin of northeastern England was one of the several relatively small extensional basins that existed in the region during the Early Jurassic (Figure 2). Formation of the basin possibly originated in response to differential movement across eastern England during the late Triassic (Rhaetian), combined with the more or less simultaneous flooding of the area by a transgressive shallow sea (*Rawson & Wright 1995*). The Market Weighton High acted as a hinge bounded northwards by the E–W trending Howardian Flamborough Fault Belt, separating the southern East Midlands Shelf from the northern Cleveland Basin (*Rawson & Wright 1995; Simms et al. 2004*). The basin was linked to the North Sea Basin complex towards the east via the Sole Pit Trough and appears to have been asymmetrical with thickest sediment accumulation towards the south (*Simms et al. 2004*). Towards the NE and west, the basin was bounded by respectively the Mid–North Sea High and the Pennine High (*Powell 2010*), suggesting that the main source of detrital influx must have been the southern foothills of the NE based Scotland Massif (i.e., Pennine High). The basin continued to subside during the Early Jurassic under influence of general mild extensional tectonism and thermal subsidence on the NW European Atlantic margin (*Doré et al. 1999*), providing for the accommodation space required to accumulate an over 450 m thick succession of predominately mudrocks in the north-eastern part of the basin (*Rawson & Wright 1995*). The emplacement of a

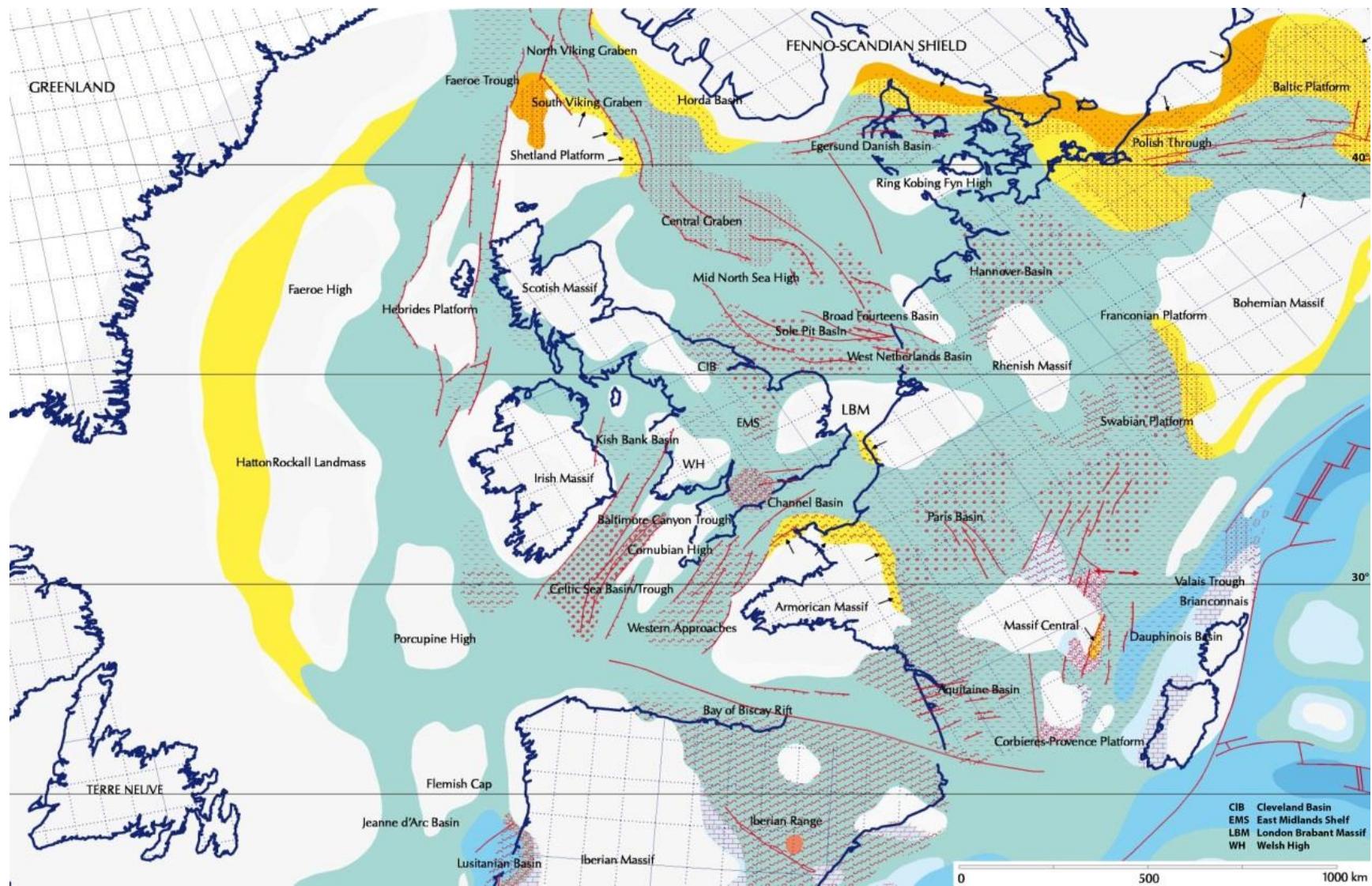


Figure 1) Paleogeographic overview and major structural elements of the western Peri-Tethys region during the Middle-Toarcian (180–178 Ma). Emergent land masses during this period in white. Full legend is listed in App. A (Modified from Thierry & Barrier 2000 in Dercourt 2000).

broad thermal dome in the central North Sea during the late Aalenian and Bajocian caused regional uplift resulting in the truncation of sediments up to even Permian age over the crest of the dome (Ziegler 1992). The development of this inferred transient plume head at the base of the lithosphere is suggested to have been initiating regional uplift as early as late Toarcian times (Underhill & Partington 1993). Due to the large extent (>1250 km diameter) of uplift and the location of the Cleveland Basin on the western edge of the North Sea Basin complex (Gatcliff 1994; Simms et al. 2004), the development of this elliptical to concentric thermal dome is believed to be responsible for a widespread shift in facies and perhaps compressional folding, causing the truncation of uppermost Toarcian sediments throughout the basin (Underhill & Partington 1993; Powell 2010). Although the studied section is from an earlier date, the late Toarcian uplift inferred by Underhill & Partington (1993), combined with the profound regional expression of this thermal dome, could possibly have had subtle effects on, for instance, sea level and bathymetry, even during earlier Toarcian times.

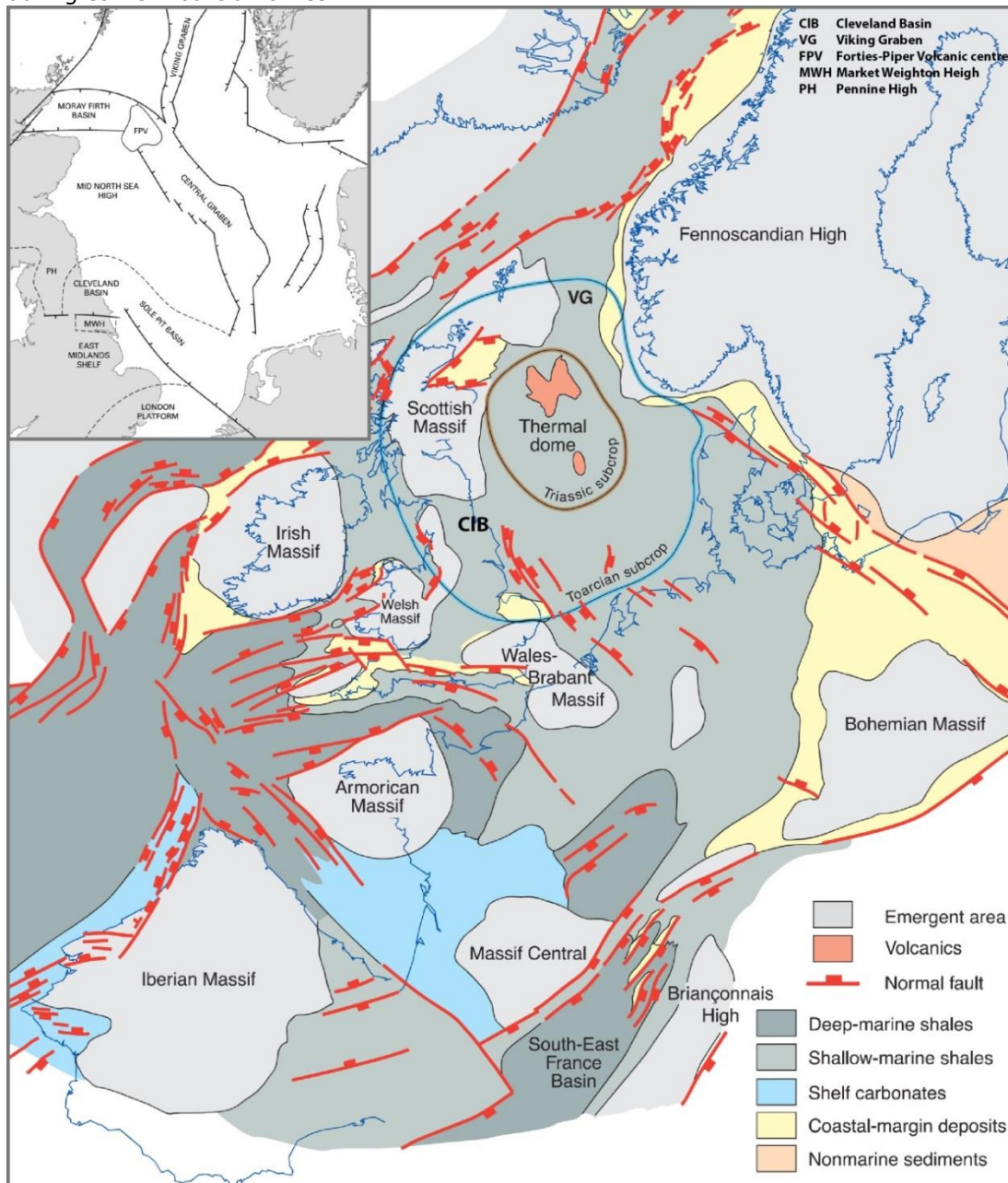


Figure 2) Distribution of active structures and sediment facies for the Early Jurassic (modified from Coward et al. 2003). Inlay displays major structural elements during the Jurassic as discussed in the text (Powell 2010 after Knox et al. 1991).

2.3 Stratigraphic Framework

The studied section consists of 92.88 meters of Lower Jurassic Upper–Pliensbachian and Toarcian sediments from the Cleveland basin. The selected section of core runs from 219.06–126.18 m depth and consists of a succession of Middle and Upper Lias sediments. The following stratigraphic overview combines the actual thicknesses of the lithostratigraphic units from the studied section with sedimentological descriptions of various studies from nearby equivalent sections along the Yorkshire coast.

The Pliensbachian part of the section comprises the uppermost 8.78 m of the Staithes Sandstone Formation combined with the 24.38 m thick Cleveland Ironstone Formation. The Staithes Sandstone Formation consists of bioturbated fine- to medium-grained sand-rich tempestite deposits interbedded with striped siltstones (Powell 2010). The Cleveland Ironstone Formation is stratigraphically subdivided in the 18.54 m thick Penny Nab Member and 5.84 m thick Kettleless Member. Overall, the formation is dominated by shale, argillaceous siltstone, and silty sandstone with interbedded thin seams of sideritic and chamositic (or berthierene) oolitic ironstone (Howard 1985). Sediments from the Penny Nab Member include up to five upward coarsening (shoaling) parasequences capped by transgressive ironstones (Simms et al. 2004). These ironstone beds are interpreted as marking the interval, or sequence boundary, between progradational and retrogradational units, while phosphate-rich horizons possible represent maximum flooding surfaces across shallow lagoons (Powell 2010). The Kettleless Member succession marks a basin-wide shallowing phase (Powell 2010) and is separated from the Penny Nab Member by an erosional surface (Simms et al. 2004). Deposition in the north and west Cleveland basin entirely consists out of chamositic and sideritic oolitic ironstone and displays a lateral facies change into siliciclastic silty shale, siltstone and very fine sandstone towards to east and southeast (Howard 1985).

The studied Toarcian interval consists of 59.72 m of Whitby Mudstone Formation. The interval contains three of the five members of the Whitby Mudstone Formation. The lowermost 14.64 m thick Grey Shale Member consists of grey to dark grey fossiliferous mudstone and siltstone with thin siltstone beds and bands of carbonate concretions (Powell 1984). The Grey Shales are overlain by 30.23 m of Mulgrave Shale Member consisting of 7.19 and 23.04 meters of the so called 'Jet Rock' and 'Bituminous Shales' respectively. Overall, the Mulgrave Shales consists of fissile bituminous silty mudstone with abundant ammonites (Powell 1984, 2010). The Jet Rock contains comparatively more regular bands of calcareous concretions, whereas the Bituminous Shales contain many more pyritic masses and crushed fossils preserved in pyrites and fossil wood is common (Howarth 1962). Furthermore, the Jet Rock displays very fine laminations, each representing fining upwards seasonal layers, and is associated with peak anoxic conditions (Rawson & Wright 1995; Pye & Krinsley 1986). The succession is topped by 14.85 m of the Alum Shale Member and contains the lower two informal units. The Alum Shales consist of relatively soft and light-grey, non-bituminous fossiliferous mudstone and silty mudstone with bands of calcareous nodules and doggers (Howarth 1962; Powell 1984). The subdivision between the lower 6.18 m thick Hard Shales and upper 8.67 m thick Main Alum Shales is based only on the relative hardness of the lower part and a higher proportion of carbonate concretions in the main/upper part (Powell 1984).

The Pliensbachian–Toarcian boundary is placed at 185,44 m depth at $182,7 \pm 0,7$ Ma (Cohen et al., 2013 – updated v.2015; Gradstein et al., 2012) and displays a subtle mismatch with the top of the Cleveland Ironstone Formation and *Pleuroceras spinatum* ammonite Zone. The vertical distribution of ammonite zones in the studied section is inferred from the work of Howarth (1955, 1962) on sections from Staithes and northwest of the Peak Fault at Ravenscar. Laterally these sections are located approximately 17 km northwest and 8 km southeast of the studied Dove's Nest core. Because these coastal sections display similar comparative thicknesses of their lithostratigraphic units in both absolute and relative sense, the more inland positioned core from Dove's Nest is presumed to have a high level of correlativity. Most zonal boundaries are easily defined as they

coincide with the subdivision of lithostratigraphic members. Probable depth estimates for the *P. spinatum*–*Dactyloceras tenuicostatum* boundary, as well as the downwards extent of the *Amaltheus margaritatus* Zone and the upwards extent of the *Hildoceras bifrons* Zone are deduced from Howarth (1955, 1962). Through careful comparison of the two sections, it is estimated that the lower 54% of the Alum Shale Member and the top 32% of the Staithes Sandstone Formation are present, at least in regard to the sections of Howarth (1955, 1962).

The assigned ages for the ammonite zone boundaries originate from strontium isotope analysis on belemnites collected from various sites within a few km of Whitby (McArthur et al., 2000). However, whereas McArthur et al. (2000) uses a tie-point age of 186,6 Ma for the P/T boundary (Pálffy et al. 1999), here the assigned ages are modified to equal the more commonly accepted age of 182,7 ± 0,7 Ma for the Pliensbachian–Toarcian boundary (Cohen et al. 2013 – updated v. 2015; Gradstein et al. 2012). Although an evident mismatch between the P/T boundary and both litho- and bio-stratigraphy still exists, these ages provide some constraint on the relative ammonite zone durations and the total time involved in deposition of the equivalent lithostratigraphic members.

The stratigraphic framework is completed by the addition of total organic carbon (TOC) and $\delta^{13}\text{C}_{\text{org}}$ curves, so that chrono-, litho-, and bio-stratigraphy combined with paleo-environmental indicators and their inherent links are captured in one single overview (Figure 3). The curves are adopted from previous analysis on the Dove’s Nest core conducted by Atar (2015), and clearly display both the negative carbon ($\delta^{13}\text{C}_{\text{org}}$) isotope excursion of the Early Toarcian, as well as the enhanced preservation of organic material associated with the Toarcian ocean anoxic event (T-OAE).

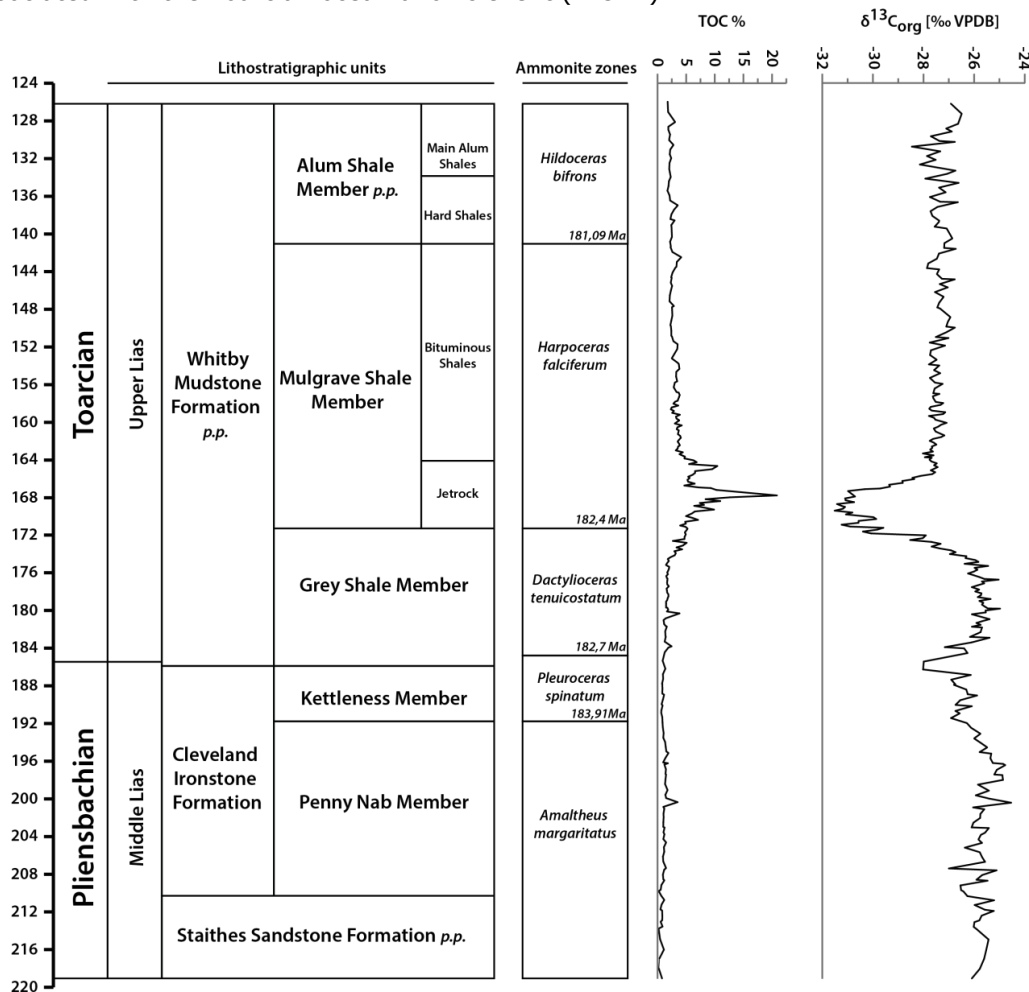


Figure 3) Stratigraphic overview of the studied section combined with total organic carbon (TOC) and $\delta^{13}\text{C}_{\text{org}}$ curves (Atar 2015). Depth in meters, see text for derivation of assigned ages.

2.4 Paleoenvironmental setting

Compared to modern times, the climate conditions during the Jurassic were warmer and more equable with wider tropical and subtropical zones, while temperate conditions characterized the polar regions in the absence of ice caps (Hallam 1975, 1985). CO₂ levels were probably around four times higher than present day (Bernier 1990) and global temperatures were possibly 5–10 °C higher than at present (Chandler *et al.* 1992). Deduced from sediments, climate conditions in western Europe changed from arid to humid during the transition from the Triassic to the Jurassic (Hallam 1981b). Substantiated by evidence from evaporites and the distribution of reefs, it has been suggested that the early Jurassic was cooler and more humid than the preceding Triassic (Frakes 1979), with frost intolerant ferns indicating subtropical and warm temperate conditions extending 50° to 60° north and south of the equator (Barnard 1973).

The precise paleogeographic setting and evolution of the Cleveland Basin is largely unknown due to the uncertainty of coastline positions, emergent landmasses and bathymetric profiles. These uncertainties are largely a consequence of widespread deposition of uniform facies belts at unknown depths, associated with an epeiric setting where landmasses are prevalently submerged. Sea levels were considerably higher than today as documented by the vast geographic distribution of transgressive deposits over continental Europe and the UK. Because paleogeographic elements such as the position of shorelines and topography of Early Jurassic 'islands' are uncertain (e.g., cf. Figures 1 & 2) or even unknown, considerable ambiguity exists about the sea-level conditions.

The studied section is part of a subordinate second-order cycle within the major Jurassic first-order transgressive/regressive Ligurian Cycle, which begins in the uppermost Norian Stage (upper Triassic) and ends at the base of upper Aalanian (middle Jurassic) (Jacquin & Graciansky 1998; Graciansky *et al.* 1998). Against the backdrop of an estimated net amount of sea-level rise of 75 m to 110 m over the course of the early Jurassic (Hallam 1981a), periods of maximum regression and transgression for the studied interval were probably the lower Penny Nab Member (middle A. *Margaritatus* Zone) and the Alum Shale Member (lower *H. bifrons* Zone) (Bradshaw 1992).

Water depths have been estimated as ranging between several meters to about a hundred meters (Hallam 1978) and are believed to have been probably in the range of a few tens of meters (Hallam 1975). In truth, no finite constraints exist on the exact depth and depositional setting of the sediments present in the studied section. Consequently, quantitative reconstructions of regional sea level fluctuations are inherently uncertain as deposits can only be assessed with respect to under- and overlying sediments. Separate relative sea-level curves for the area have been published by employing facies analysis (Hallam 1981a; Haq *et al.* 1987; Hesselbo & Jenkyns 1998). Although they agree on increasing water depths during deposition of the Whitby Mudstone Formation in response to a phase of major basin subsidence during deposition of the Grey Shale Member (Powell 2010), as well as a regressive episode towards the Pliensbachian–Toarcian boundary, they also vary considerably concerning the Upper Pliensbachian and in respect to onsets and rates of sea-level change (Figure 4).

The late Pliensbachian–early Toarcian interval ranks as one of the major Mesozoic paleoecological disturbances as c. 20% of the marine and continental families went extinct (Dera *et al.* 2011). This profound drop in diversity affected a variety of marine groups including ostracods, foraminifers, brachiopods, bivalves and cnidarians (Dera *et al.* 2010 and references therein). Over the years, the regional and global varying expression and timing of this Early Jurassic 'minor' extinction event has led to considerable debate and somewhat contesting views, ranging from a single protracted event over 7.5 m.y. divided into zones (Little & Benton 1995; Little 1996) to multi-phased with six distinct extinction pulses (Caruthers *et al.* 2013). Concerning NW Europe and the Cleveland Basin the general consensus appears to be that the pinnacle of the event, at least on a species level, is located at the *D. tenuicostatum*–*H. falciferum* Zone boundary (Hallam 1987; Harries &

Little 1999; Caswell et al. 2009), coinciding with a brief period of overlap in the distribution of black shale facies throughout Europe, indicating an intimate link between widespread marine anoxia and the Toarcian mass extinction (Wignall et al. 2005). Focussing in on the Cleveland Basin, the late Pliensbachian displays a diverse range of benthic and nekton species including infaunal and epifaunal bivalves, brachiopods, crinoids, belemnites and ammonites (Little 1996). The trend of gradually rising diversity over the course of the Early Jurassic was sharply reversed in the early Toarcian (Hallam & Wignall 1997), with an 84% drop in species richness among the bivalves at the end of the Pliensbachian as the most striking example (Hallam 1986). The few species of bivalves that endured into the Toarcian Grey Shales were accompanied by abundant belemnites and *D. tenuicostatum* and *D. semiculatum* ammonites (Hallam 1967). The subsequent onset of black shale deposition (Jet Rock, *H. falciferum* Zone) culminated in an extinction event where species diversity dropped by 77%, killing all infauna and 87% of benthos species (Little 1996). As a result, the *H. falciferum* Zone displays impoverished invertebrate fauna restricted in variety and dominated by ammonites, belemnites and two species of bivalves, and substantial new fauna with Middle Jurassic affinities (Hallam 1967).

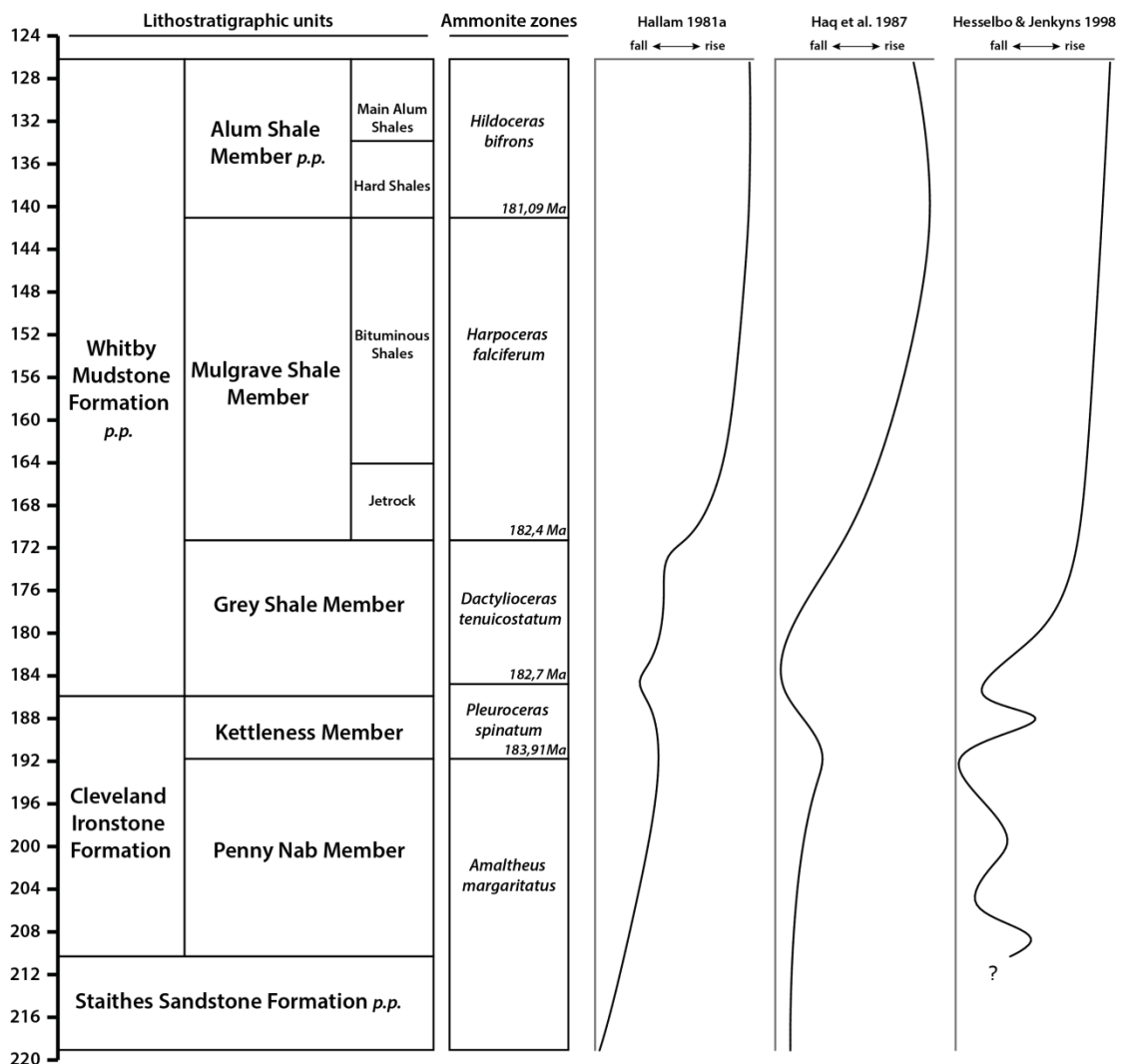


Figure 4) Comparative illustration of different relative sea level curves. Curves of Hallam (1981a) and Haq et al. (1987) redrawn based on ammonite Zones. Curve of Hesselbo & Jenkyns (1998) is redrawn by converting curve tipping points to depth estimates for the studied section based on relative thickness of ammonite Subzones (Howarth 1955) and corresponding lithostratigraphy (Howard 1985). Bottom core continuation into the Staithe Sandstone Formation is unresolved due to unknown extent of the *Amaltheus stokesi* Subzone.

3. Materials and Methods

The Dove's Nest core was drilled in February 2013, by Fugro, for York Potash Limited, about 5.5 km south of Whitby, North Yorkshire (54.436502, -0.624797). In 2013, Atar (2015) and Trabucho Alexandre et al. (2017) collected a total of 280 samples from the northern shaft of the core at 20–50 cm intervals between 126.18 and 219.06 m depth. For this study, 21 samples at approximately 4 meters spacing were selected (Table 1), spanning Upper Pliensbachian and Toarcian sediments of the Lower Jurassic.

The sampled interval corresponds to the interval between "bed" 17 in the Staithes Sandstone Formation (*A. margaritatus* Zone) and "bed" 64 in the Alum Shale Formation (*H. bifrons* Zone, Main Alum Shales). Atar (2015) correlated the succession cored at Dove's Nest, Yorkshire, with the succession exposed along the Yorkshire coast on the basis of lithostratigraphy and carbon isotope stratigraphy. Although there are some important lateral facies changes, namely not all ironstone horizons can be correlated between the Yorkshire coast and the core (see Hemingway & Rayner 1974, fig. 43), the thickness of the Lias Group formations in the core appears to be similar to that exposed on the Yorkshire coast. The shape and thickness of the lower Toarcian carbon isotope excursion in the core are the same as those of the curves of Hesselbo et al. (2000) and Kemp et al. (2005), which come from the Yorkshire coast, namely the lower Toarcian outcrops at Hawsker Bottoms and Port Mulgrave. Thus, unlike in the Felixkirk Borehole, the succession cored at Dove's Nest is not attenuated.

Sample preparation and Scanning Electron Microscopy (SEM) were conducted at the Gemeenschappelijk Milieulaboratorium (GML) of Utrecht University. The preparation of oriented mounts and X-ray diffractometry were carried out by Ms. Atar at the Department of Earth Sciences of Durham University.

Sample	Depth (m)				
DN01	130.75*	Toarcian	Whitby Mudstone Fm.	Alum Shale Mb.	
DN02	135.10			Main Alum Sh.	
DN03	139.25			Hard Shales	
DN04	143.65			Mulgrave Shale Mb.	Bituminous Shales
DN05	147.32				
DN06	151.55				
DN07	155.30				
DN08	159.54			Grey Shale Mb.	Jet Rock
DN09	163.52				
DN10	167.31			Pliensbachian	Cleveland Ironstone Fm.
DN11	171.41				
DN12	175.46	Penny Nab Mb.			
DN13	179.57				
DN14	183.38	Stait. Sst. Fm.			
DN15	187.33				
DN16	191.41				
DN17	195.68				
DN18	199.61				
DN19	203.58				
DN20	207.37				
DN21	211.75				

Table 1) Samples and corresponding depth. Due to insufficient sample availability, sample DN01 corresponds to 130.75 m for the grain size measurements, while the clay DN01 sample corresponds to 131.75 m. Sampling interval (~4 m) was chosen to include all different lithostratigraphic members and informal units present.

3.1 Rationale

To determine the overall quartz (silt) content and grain size distribution per sample, a new method has been developed to circumvent uncertainties and problems associated with the analysis of grain size distributions in shales. Standard practice for this type of measurements involves the crushing of shale rock fragments and the successive removal of the carbonate fraction and organic compounds from the samples. Although these techniques are well established and widely applied, they also bring about uncertainties and sample requirements that are not always present or taken into account. Samples will fully disaggregate by adding hydrochloric acid (HCl) or acetic acid (CH₃COOH) to achieve

carbonate dissolution and hydrogen peroxide (H₂O₂) for the removal of organic compounds. However, this only works when samples are completely cemented by exclusively, or a combination of, carbonate and organic material, which is not always the case. Furthermore, the pre-treatment of samples commonly involves the crushing of rock fragments into a powder of 'individual grains'. This technique provides no process control and potentially breaks-up aggregates and larger particles into smaller ones or may fail to fully separate strongly cemented grains, making it impossible to determine whether the particle distribution of the resulting powder is representative of the original sample.

To avoid these issues, this study applies microscopic methods previously predominately applied to thin sections to determine a wide range of petrographic characteristics of shales (e.g., Krinsley *et al.* 1983, 1993; Pye & Krinsley 1984, 1986; O'Brien 1990, 1996; Tovey & Krinsley 1991; Macquaker & Taylor 1996; Francus 1998; Houben *et al.* 2013, 2016). Although polished thin sections are in principle ideal for petrographic analysis, their preparation is challenging due to the wide range in hardness of constituent minerals, general lack of cementation, and difficulties in polishing soft clay minerals (Schieber & Zimmerle 1998). To minimize the damaging effects of mechanical polishing on soft-shale samples, 2 mm thick sample blocks mounted on stubs were used. After the standard mechanical polishing of the surface, the samples were mounted in a Precision Ion Polishing System (PIPS) for a final polish with argon ions. By using thick sample blocks instead of 30 µm thin sections in combination with the PIPS procedure, any effects and artefacts from the mechanical polishing are mitigated, reduced or even removed from the sample, producing sample surfaces of superior quality in regards to standard shale thin sections. This relatively simple and effective procedure of sample preparation combined with the ever increasing capabilities in image analysis, provides for a range of new opportunities to analyse this type of deposits in a potentially more reliable and accurate manner, without the necessity for time consuming and destructive techniques as crushing and partial sample dissolution by acid treatments.

Besides determining the overall quartz silt content and grain size distributions through image analysis, this study also attempts to establish a link with the variation in clay mineralogy by using standard X-ray diffraction techniques and quantification analysis described in detail in sections 3.6 and 3.7.

3.2 Quartz silt analysis - sample preparation

Sample blocks were glued onto 8 mm diameter SEM stubs with the bedding facing upwards perpendicular to the stub's surface. Epoxy-resin was added to fill out the unused stub area and permanently anchor the rock fragment to the stub's surface. The samples were then cut parallel to the surface of the stub at 2 mm height and fine polished mechanically using 1 µm and 0.3 µm aluminium oxide abrasive to create an initial smooth surface. To acquire the best possible surface, the samples were then placed in a SEM Mill (Fischione Instruments; model 1060) and 'stripped' using a 4.0 kV beam at a current of 1.2 µA for 2 hours. This technique applies two Ar-ion beams at a 2° angle to give a final polish of the surface, while the sample is rotated at 3 RPM to avoid striations due to prolonged exposure and ensure a uniform finish. Because electron-beam instruments rely on an emitted signal, nonconducting samples require a conductive coating to increase the bulk electrical conductivity before examination (Goldstein *et al.* 2007). Therefore, the polished surfaces were coated with an 8 nm thick platinum coating, reducing or eliminating image distortion due to complex image artefacts caused by charging phenomena in the process.

3.3 Quartz silt analysis – acquisition and image analysis

To determine the overall quartz silt content and grain size distribution of the shales a procedure involving scanning electron microscopy examination (JEOL JCM-6000 Bench top SEM) combined with an energy dispersive X-ray analysis system (EDX) was applied. First a back scattered electron (BSE) image of the sample to ensure the reliability of the EDX mapping program by comparing features that are clearly distinguishable independently of the applied technique (e.g., pyrite framboids). The resulting data, produced by subsequent

EDX mapping, consists of elemental maps displaying distributions and abundances of the selected elements. The assembly of selected elements for EDX mapping is based on expected occurrences in the samples (i.e., elements associated with quartz silt, clays, carbonate, pyrite, and organic material) and include carbon, oxygen, sodium, magnesium, aluminium, silicon, sulphur, potassium, calcium, titanium, and iron. This selection incorporates all elements required to differentiate between all primary constituents of shale-type deposits, making it possible to isolate quartz silt from clay-bound silicon and other constituents by image analysis. To ensure the acquired image captures enough sample area to produce a representative and viable grain size distribution, a compromise between the total grain population and the minimal detectable grain size is made. Furthermore, to avoid unnecessary uncertainties related to detection limits, the lower limit, or cut-off, for unequivocal identification of quartz grains (i.e., grains over 2 μm diameter) is determined to be least 4 pixel squared. The resulting maps have an image resolution of 1024 x 768 px, representing a sample area of 0.803 by 0.602 mm and a pixel area of 0.615 μm^2 at 150x magnification. This setup meets all previous requirements as 4 px² equals 2.461 μm^2 , corresponding to a grain size (particle diameter) of 1.770 μm , while still providing enough sample area for adequate grain population numbers.

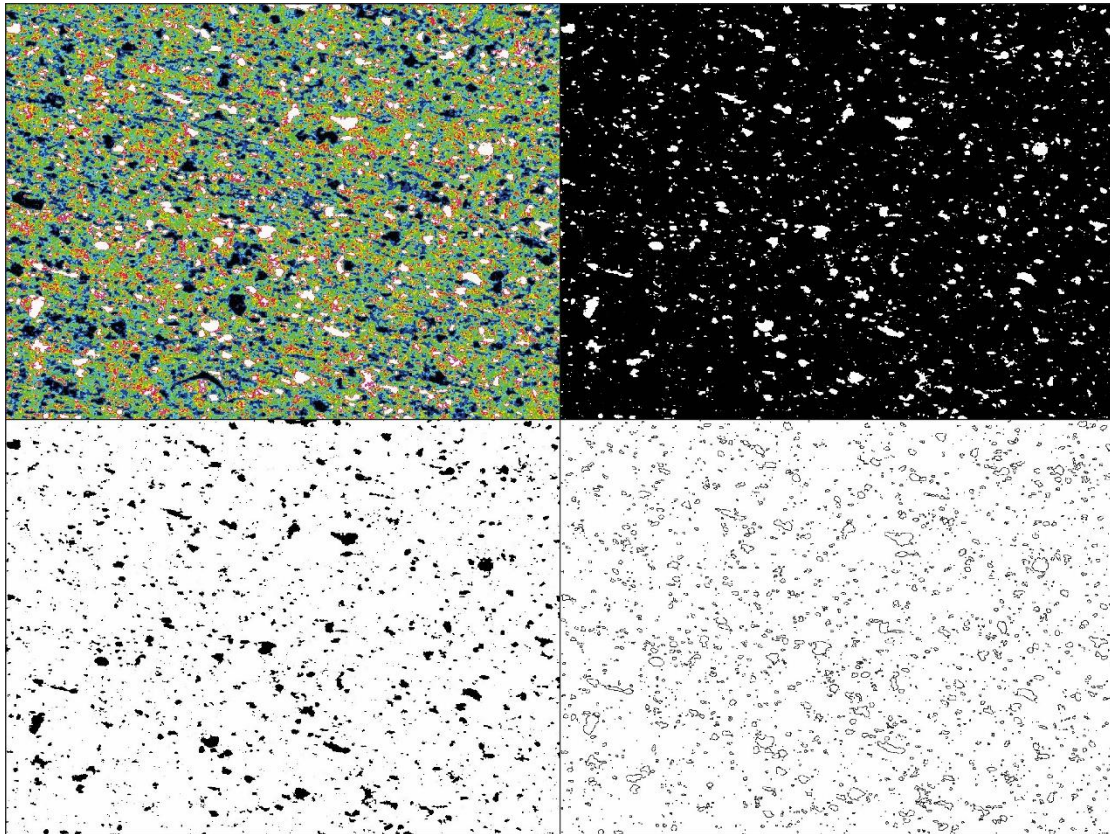


Figure 5) Example of consecutive images used from initial to final (sample DN10; true size for each image: 0.803 x 0.602 mm). Top-left: original EDX Si-map. Peak readings in white, complete absence of silicon in black. Top-right: peak silicon occurrences (in white) isolated from background by thresholding. Bottom-left: inverted binary image for determination of total silt-quartz percentage. Grains touching image edge included. Bottom-right: Edited image for grain size measurements displaying grain outlines. Touching grains separated, partial grains touching image edge excluded.

Diagnostic image analysis is performed by converting the images into grey-scales, so that the different elemental maps are uniform and suitable for manipulation. Because all clays are hydrous aluminium silicates, and hence all contain aluminium, it is possible to distinguish between clay bounded silicon and quartz silt by carefully comparing the elemental aluminium and silicon maps to confirm high silica concentrations as true quartz

grains. By doing so, it is confirmed that all peak readings from the silicon elemental map indeed represent quartz, validating the use of the raw silicon map (i.e. the original coloured image) for further analysis (Figure 5). The remaining maps were used to check against the BSE image and confirm the accuracy of the EDX mapping procedure. To measure the quartz grain size distribution the grains are isolated from their background by image thresholding, creating a binary image where the quartz fraction is effectively isolated from the bulk composition, so that only well-defined high silicon concentrations associated with pure quartz grains are included in the measurements. The binary image is subsequently measured using Fiji's ImageJ image processing package to determine the area percentage quartz. The final step before grain size measurements are generated involves the manual segmentation of touching particles through careful editing of the grain boundaries, after which the software produces an area per detected grain while excluding any grains that are undefinable due to contact with the image's edge. Subsequent analysis requires the exclusion of grains below the threshold value of 4 px², as well as the conversion of grain area to grain diameter. This procedure involves the conversion of measured areas of irregularly shaped grains (see Figure 5) to area-equivalent spherical grains to determine grain diameters (i.e., diameter = $2 \cdot \sqrt{(\text{area}/\pi)}$). By doing so, quartz grains are consistently assessed in similar fashion to produce practical distributions, while complex measurements of unknown grain dimensions (due to unknown grain orientations and surface exposure) are avoided.

Due to the difficulty of direct comparison between multiple samples when working with subtle-deviating grain size distributions in shales, the resulting data is made suitable for interpretation by subdividing the distributions into grain size classes according to Udden (1914) and Wentworth (1922). The finest part of the distribution, the bottom clay-sized class, encompasses any grain above the lower detection limit and below the size of very fine silt (1.770–3.906 μm).

3.4 Quartz silt analysis – statistical processing

Grain size analysis is completed by applying the moments method for unequal class intervals of Camp (1931) and Krumbein (1936) to determine the mean, standard deviation, skewness, mean cubed deviation, and kurtosis of the distributions. These parameters are computed using statistical moments, which, in turn, are derived from mechanics. By replacing the mechanical force with a frequency function, the moment force around a point of rotation from mechanics now represents a moment of the frequency function around an arbitrary point, in this case the mode of the distribution (Friedman & Sanders 1978; Friedman 1979). The use of statistical moments is considered to produce more representative measures of the obtained parameters in regard to their graphical analogous, as the entire grain population (i.e., quartz grains >1.77 μm) is employed instead of a selection of graphically derived points (McManus 1988).

In order for the moments method to work, and because the measured distributions are open ended, an additional class of 0,02 μm containing zero particles is added to create the required closed distribution. Furthermore, grain sizes in micrometres (μm) had to be converted to the phi-scale by $\Phi = -\log_2(d/d_0)$, where d is the measured grain size and d_0 is the diameter of a 1 μm grain. This conversion produces a logarithmical based dimensionless grain size distribution suitable for statistical analysis (McManus 1963, 1988; Krumbein 1964), and hence, allows the determination of parameters such as standard deviation, skewness, and kurtosis, according to equations listed below (Table 2).

The resulting principal statistical parameters provide measures for environmentally-controlled characteristics such as sorting (standard deviation), symmetry (skewness), and peakedness (kurtosis) of the grain size distributions, allowing qualitative description and comparison of the samples in terms of their sedimentological characteristics (Friedman 1962, 1967).

Moment	Parameter	Computation
1 st	Mean	$\bar{x} = \frac{\sum f \cdot m}{n}$
2 nd	Standard deviation	$\sigma = \sqrt{\frac{\sum f(m - \bar{x})^2}{n}}$
3 rd	Skewness	$\alpha_3 = \frac{\sigma^{-3} \cdot \sum f(m - \bar{x})^3}{n}$
4 th	Kurtosis	$\alpha_4 = \frac{\sigma^{-4} \cdot \sum f(m - \bar{x})^4}{n}$
	Mean cubed deviation	$\alpha_3 \sigma^3 = \frac{\sum f(m - \bar{x})^3}{n}$

Table 2) Measured parameters and their respective computations

f = area percent of each grain size class present

m = midpoint of each grain size class in phi values

n = total number of particles which is 100 when f is in percent

3.5 Clay mineralogy – XRD sample preparation

Measuring clay mineralogy by X-ray diffraction (XRD) requires the separation of the clay fraction from the bulk sample. Bulk powder samples were produced by crushing the samples with a pestle and mortar, which is the preferred method as mechanical crushing or grinding adds far more non-clay minerals to the clay-size fraction (Moore & Reynolds 1989; McManus 1991). The removal of carbonate from the samples is achieved by the addition of 0,3 M acetic acid (CH₃COOH), which, in contrast to hydrochloric acid (HCl), preserves the clay minerals. Organic compounds are removed from the samples by adding 6% hydrogen peroxide (H₂O₂). The subsequent separation of the clay fraction from other constituents is performed by adding a dispersion agent (Na₄P₂O₇·10H₂O+Na₂CO₃) to neutralize the particle charges and prevent clay flocculation, after which the samples are centrifuged (Heraeus Megafuge 40 Centrifuge) for 5 min at 400 RPM. The required centrifugal time and RPM are determined by Stokes's Law for particle settling velocity and proved to effectively separate the below 4 μm fraction from the coarser sample constituents (Figure 6). Although it is common practice to use even finer fractions for the determination of clay mineralogy by X-ray diffraction techniques (i.e., <2 μm), this study deliberately uses a slightly coarser selection of <4 μm to avoid loss of any potential coarser clay particles from the samples. Phyllosilicates are known to grow to silt sized particles, meaning they technically no longer classify as clay despite being clay minerals (Weaver 1980; 1989). Including particles up to 4 μm therefore prevents the potential loss of near silt-sized clay particles, which in turn could lead to errors with the quantification of relative clay abundancies.

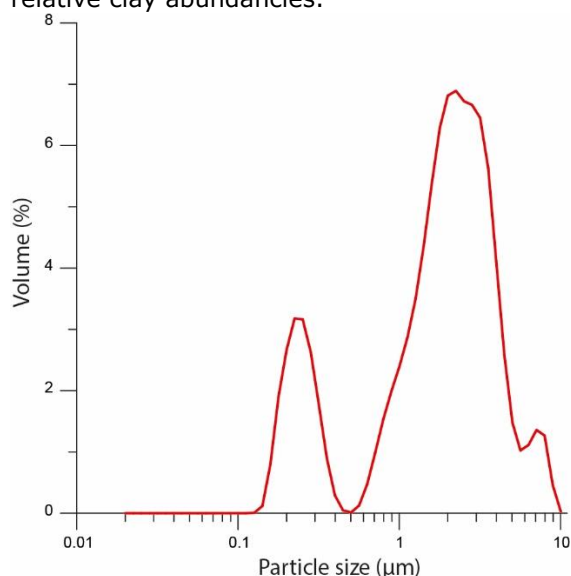


Figure 6) Particle size distribution of separated fraction measured with a Malvern Mastersizer 2000 laser diffraction particle size analyser showing the successful removal of >4 μm particles. Only one reference sample (DN21) is measured to confirm the method as all samples were prepared in a single batch.

To exclude mineral d-spacing variability of the minerals due to the cation population on their exchange complex (*Barshad 1950; Mielenz et al. 1955*), it is required to create a monoionic exchange complex by controlling the cation saturation, so that mineral characteristics can be inferred from d-spacings (*Harris & White 2008*). This is achieved by saturating the samples with a 0,1 M MgCl₂ solution, after which the samples were washed with deionized water, centrifuged, and decanted three times to produce a neutral fluid. Preparation is concluded by transferring 0,5 ml of the resulting fully saturated clay suspensions onto glass slides by using a pipette, after which the samples are ready for measurement.

3.6 Clay mineralogy – XRD measurements and interpretation

X-ray diffractometry measurements was performed by using a Bruker d8 Advance diffractometer (Cu Ka, 40 kV, 40 mA) at Durham University, UK. The samples are measured air-dried, ethylene glycol solvated, and after being heated to 550 °C. Air-dried samples mounts were scanned between 2° and 50° 2θ at steps of 0.02°. Ethylene glycol solvated and 550 °C heated mounts were scanned between 2° and 30° 2θ at steps of 0.02°.

The identification of minerals requires XRD measurements of the samples at different conditions designed to yield a specific response of the minerals d-spacing composition. Although a mineral may be recognized due to a specific set of peaks, definite identification generally follows from the comparative interpretation of the results for each treatment. This is warranted due to fixed responses and simple exclusion principles based on the predicted response of a mineral species. Minerals with overlapping d-spacing regions (e.g., smectite, vermiculite, and chlorite) can be identified accordingly by specific diffraction peak shifts following solvation with specific ions and/or heating treatments (*Moore & Reynolds 1989; Dixon & Weed 1989; Bergaya & Lagaly 2013*).

3.7 Clay mineralogy – Quantifying relative abundances

The quantification of sample constituents based on X-ray diffraction patterns has been subject for debate for decades. Although during this time many methods have been developed, the unsolved problems of peak interference and standard suitability have led to the belief that no invariant methodology is possible for quantitative analysis (*Moore & Reynolds 1989*). Besides the lack of a uniform approach for quantification, most methods are by definition semi-quantitative as, although expressed in terms in of quantity, the uncertainty (i.e., accuracy) is not known or unreasonably large (*Hillier 2003*).

Quantitative analysis by XRD techniques relies on the estimation of peak intensities above background by peak integration. Hence, the first fundamental step in analysis is the determination and subtraction of the background radiation from the diffraction pattern, so that only the peak area superimposed on the background pattern remains. A typical background, or baseline, for a silicate clay fraction is nonlinear and rises sharply toward the low angle region of the pattern, while also forming a broad swell beneath the 3.35 Å (26.6° 2θ) quartz peak (*Carver 1971*). Because the region of interest (~ 6–20 Å) for the produced diffraction patterns in this study lies beyond this quartz-peak swell, the fitting of the background curves is focussed on the sharp increase at low angle regions while assuming a constant background for the high angle regions. To obtain a realistic background and to make the data suitable for semi-quantitative analysis, the following four step procedure is performed for each sample (Figure 7). The first step is drawing a baseline minimum corresponding with the minimum counts per second measured, providing a horizontal 'cut-off' of the patterns from which to build on. Step two is combining the high angle part of this baseline minimum with a low angle partial selection of the diffraction pattern, so that a 3rd order polynomial curve can be fitted through the data. Step three subsequently combines the assumed high angle baseline minimum with the nonlinear background best-fit curve for the low angle region, producing a composite baseline for the entire pattern. The final step is baseline subtraction from the original diffraction pattern resulting in the background corrected data required for analysis.

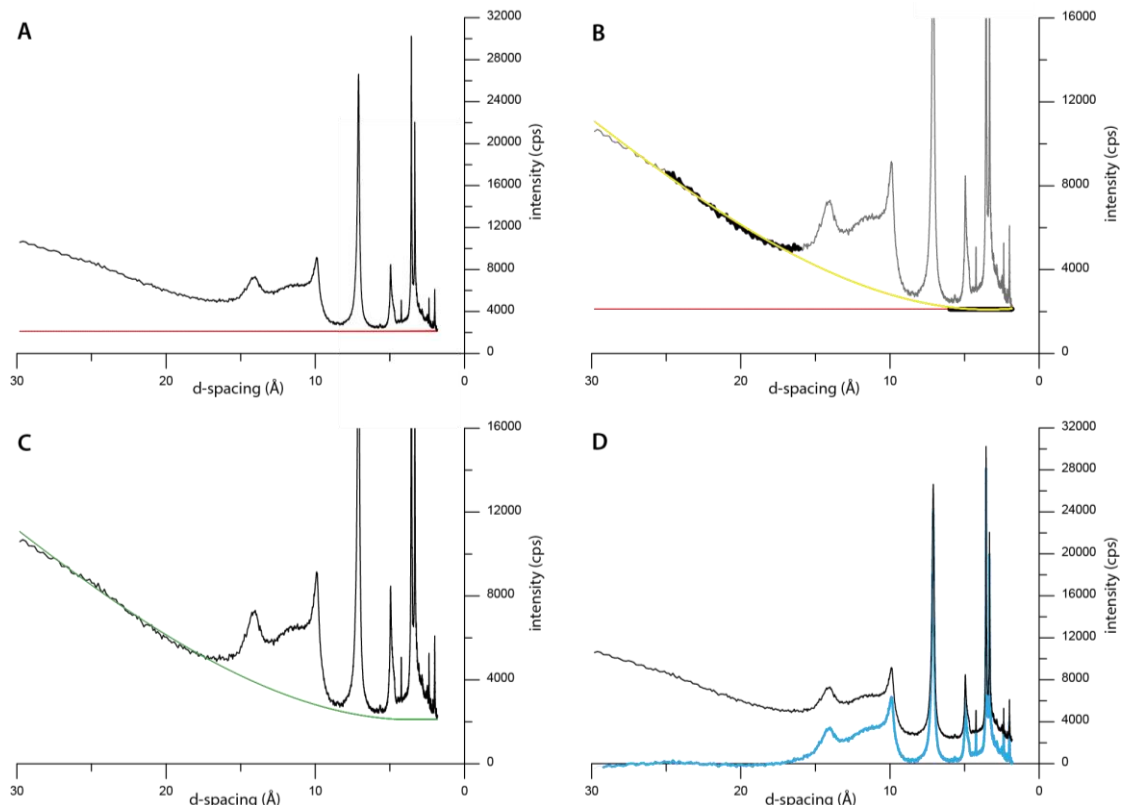


Figure 7) Illustration of stepwise process for background determination and subtraction (exemplified by sample DN09), see text for detailed explanation. A: air-dried data (black) and baseline minimum (red). B: selected data used for baseline curve fitting (bold-black) and trendline through selected data (yellow). C: composite baseline (green) D: original pattern (black) and background corrected data (blue).

Because of the large variety in (semi-) quantitative methods, and their inherent errors in accuracy, this study adopts the use of two different techniques. The first involves the combined application of Peak-area Integration with peak-Height Ratios (henceforth referred to as "PIHR method"), while the second uses the Peak-Height Half-Width (PHHW) method for peak-area determination (Figure 8). The PIHR method is designed to incorporate the theoretically more accurate comparison of peak areas (Carver 1971) by the use of peak-height ratios to differentiate between the (interstratified) clay endmembers. Peak interference causes apparent pattern overlapping and/or diffuse diffraction, complicating otherwise straight forward measurements as in case of well-defined peaks. By measuring the area below these two separate reflections as one and subsequently determining the specific contribution of each endmember by peak-height ratios, complex pattern fitting and time consuming mathematical integrations are avoided. In practice the PIHR method thus produces two area measurements, one well defined (blue area; Figure 8) and one composite area (green area; Figure 8), which is subsequently subdivided using peak-height ratios. The cumulative measured area is then normalized to represent 100% to determine the relative contribution of each endmember. In contrast to the PIHR method, the easy to apply PHHW method requires no complex integration of ill-defined peak areas and supposedly produces superior results as it is less sensitive to background related error (Moore & Reynolds 1989). Application of this method is complicated by peak distortion in case of a large 'saddle' between peaks, resulting in peak asymmetry and preventing the determination of the full-width at half maximum (FWHM). To circumvent this issue it is assumed that the peaks in question (b & c) are distorted towards the saddle, but represent their true symmetrical profile away from the saddle. Computation of FWHM follows from measuring full-width/2 at half maximum from the symmetrical part, which is then doubled to obtain FWHM (Moore & Reynolds 1989). Relative quantities finally results from multiplying FWHM with peak-height for each endmember and summing the products to match 100%, after which each endmembers contribution to the total can be determined.

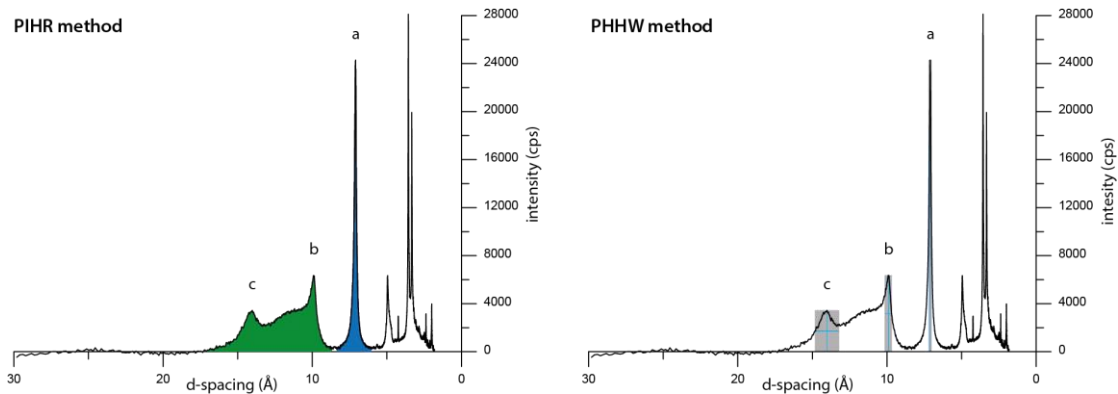


Figure 8) Outline of combined Peak-area Integration with peak-Height Ratios (PIHR) method and Peak-Height-Half-Width (PHHW) method. Diffraction pattern is background corrected data of sample DN16. See text for detailed descriptions. Note the computation of full-width at half-maximum by doubling the half-width of the assumed symmetric right limb of peak b and left limb of peak c.

Although the measurement of peak intensity is considered the most difficult problem in quantitative analysis and for some sample peak interferences impossible (*Moore & Reynolds 1989*). The use of modern software tools has made it less time consuming to perform integration of complex patterns (this study for example employs OriginPro). However, analysis of broad diffuse diffraction patterns with interstratified and/or mixed constituents remains difficult at best. The use of two different methods for semi-quantitative analysis in this study is therefore aimed at providing some constrains on the precision and accuracy of the results.

4. Results

4.1 Grain size measurements from image analysis

The maps from which the distributions have been derived are listed in appendix B. Original measurements, normalized distribution (against total grain count), and the Udden-Wentworth based distribution for each sample are listed in appendix C. The Udden-Wentworth based distributions are presented below as trends over the extent of the core, including mean grain size and the total quartz present per sample (Figure 9).

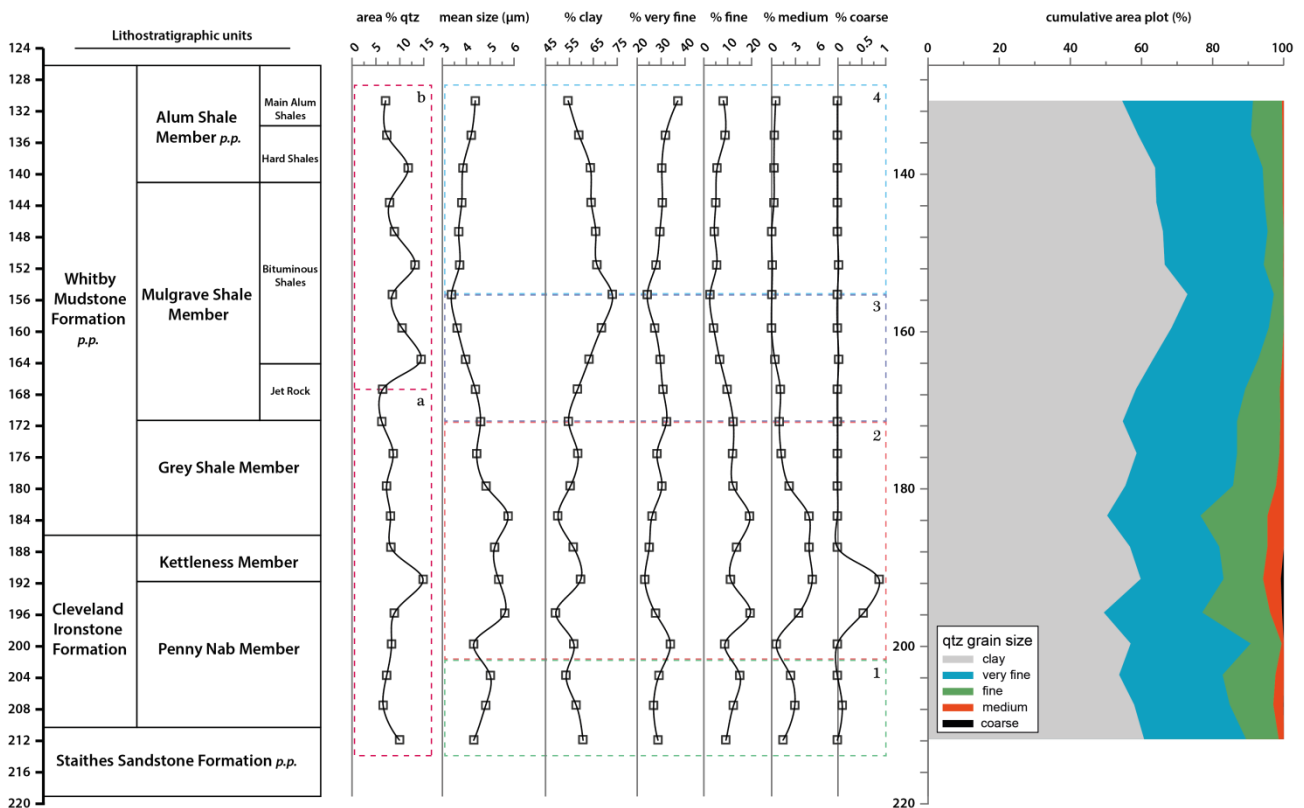


Figure 9) Graphic representation of grain size measurements versus depth (m) and lithostratigraphy. Area % qtz refers to total area of quartz particles measured per sample. Relative contribution of each grain size class is expressed as percentage of total quartz grains, trends are visualized by smoothed lines. The designation 'clay' represents quartz particles in the 1.770–3.906 µm size range, all other refer to silt-sized subclasses corresponding to the Udden-Wentworth scale. See text for description of the highlighted boxes. Overall distribution of grains per size class versus depth is displayed by cumulative area plot.

The results for the total influx of quartz ("area % qtz") display an almost dichotomized character between the relatively stable lower half (section a) and the much more pronounced fluctuations of the upper half (section b) of the core. The bottom part shows a general decrease of total quartz with only minor variability, except for a pronounced increase at the base of the Kettleness Member (uppermost Pliensbachian). The top part of the core, starting somewhere just below the transition between the Jet Rock and Bituminous Shales, displays a clearly recognizable larger degree of variability superimposed on an overall higher total input on average. At first glance, a clear relation between the total influx of quartz and the corresponding grain size distribution seems to be absent. However, when the data is examined more closely (Table 3) it shows that three out of four increases in area % quartz over the 'normal' trend are accompanied by the occurrence of coarse silt particles, suggesting elevated levels of hydrodynamic energy during episodes of increased quartz input.

depth	area % qtz	mean size (μm)	% clay	% very fine	% fine	% medium	% coarse
130.75	7.07	4.39	54.53	36.77	8.14	0.56	0
135.10	7.33	4.22	59.03	31.69	8.89	0.40	0
139.25	11.77	3.88	63.81	30.23	5.61	0.36	0
143.65	7.90	3.83	64.14	30.42	5.10	0.34	0
147.32	8.89	3.70	66.00	29.42	4.50	0.07	0
151.55	13.18	3.74	66.50	27.85	5.48	0.15	0.02
155.3	8.48	3.40	72.89	24.29	2.74	0.09	0
159.54	10.48	3.63	68.42	27.33	4.20	0.06	0
163.52	14.45	3.98	63.25	29.55	6.71	0.46	0.03
167.31	6.46	4.40	58.45	30.69	9.73	1.13	0
171.41	6.29	4.61	54.70	32.14	12.16	1.00	0
175.46	8.66	4.45	58.60	28.25	11.93	1.23	0
179.57	7.27	4.84	55.45	30.26	12.09	2.20	0
183.38	8.09	5.76	50.30	26.25	18.83	4.62	0
187.33	8.17	5.20	56.73	25.10	13.55	4.62	0
191.41	14.87	5.37	59.75	23.31	11.09	5.01	0.85
195.68	8.88	5.62	49.37	27.67	19.08	3.35	0.52
199.61	8.31	4.32	56.92	33.72	8.72	0.63	0
203.58	7.29	5.02	53.69	29.08	14.86	2.37	0
207.37	6.57	4.83	57.91	26.87	12.24	2.89	0.10
211.75	9.97	4.33	60.71	28.66	9.19	1.45	0

Table 3) Area % quartz, mean size, and grain size distribution in percentage of total (see caption Figure 9 for details). Note occurrence of coarse silt quartz during elevated influx of total quartz at 191.41, 163.52, and 151.55 m depth.

The remaining curves are closely interdependent, as they (i.e., the grain size classes expressed in percentage of total) required to be normalized to validate sample-to-sample comparison. Consequently, when the grain size classes are considered in terms of overall trends, it is within reason to include the mean size curve as all curves globally comply to the same trend. By doing so, four distinctly different sections are identified, illustrated by boxes 1–4 in Figure 9, that show no correlation to the stratigraphic subdivisions.

The bottom of the core (box 1) shows a slight increase of the mean size accompanied by a gradual decrease and increase of the clay and fine fractions. Although the other grain size fractions show a more 'curved' development, no major perturbation of the trend takes place, suggesting fairly constant sedimentological conditions moving upward from the uppermost Staithes Sandstone Formation into the lower regions of the Cleveland Ironstone Formation.

The most wavering and deviating development over the course of the core is displayed in the second section of the core (box 2). Moving upwards from the Penny Nab Member into the Kettleless Member, mean grain size increases and stays relatively high throughout the transition into the Toarcian Whitby Mudstone Formation, before dropping back to lower values towards to the top of the Grey Shale Member. The most substantial influx of coarse particles over the extent of the core is at the top of the Penny Nab Member and it seems no chance occurrence that total influx of quartz during this episode also displays a maximum. The medium fraction also displays increases values towards the base of the Kettleless Member, but retains these elevated levels considerable longer before returning to the lower values observed in the Grey Shale Member. Looking at the overall development of both the mean size and medium sized fraction, it is plausible to infer that the raised average mean size during much of this period can be attributed to the increased contribution of medium sized grains to the grain size distribution.

The transition into the third section (box 3) of the core is immediately below the base of the Jet Rock; the sample marking the transition is 15 cm below the boundary between the Grey Shale and Mulgrave Shale Members. In this section, mean size decreases slowly until overall minimum value is reached at the top of the section at approximately halfway through the Bituminous Shales. Both the clay and fine fraction match this development

displaying maximum and minimum values respectively. No major fluctuations occur during this period, suggesting low and constant (decreasing) energetic conditions, although a slight input of medium, and incidental coarse-sized, particles is observed.

The top part of the core (section/box 4) shows an almost mirrored development compared to the third section. Throughout the upper part of the Bituminous Shales and Alum Shale Member the mean size displays a generally increasing trend, consistent with similar trends for the very-fine, fine, and medium fractions. However, whereas the third section displayed a gradual and consistent trend for almost all curves, section four shows a more wavering development with values deviating from the overall imposed trend. The switch in tendency and inconsistent development suggests slightly more variable conditions in comparison with section three. Although the clay fraction decreases over the course of the section, resulting in a shift to a coarser grain size distribution, it is questionable whether this can be attributed to higher energetic conditions due to the lack of medium and coarse sized influx as observed in in the second section.

4.2 Grain size distributions - Statistical analysis

To complement the standard grain size distributions resulting from image analysis, statistical parameters have been computed using the moments method (Figure 10). When looking at the overall appearance of the curves, a distinct difference is observed between the fairly stable top part of the core (section d) and the fluctuations of the lower part (section c). Although placement of the boundary is somewhat arbitrary, it matches the subdivision between bottom and top core sections of the area % quartz (cf. Figure 9). Despite this similarity, none of the determined parameters show any apparent relationship with variations in quartz influx.

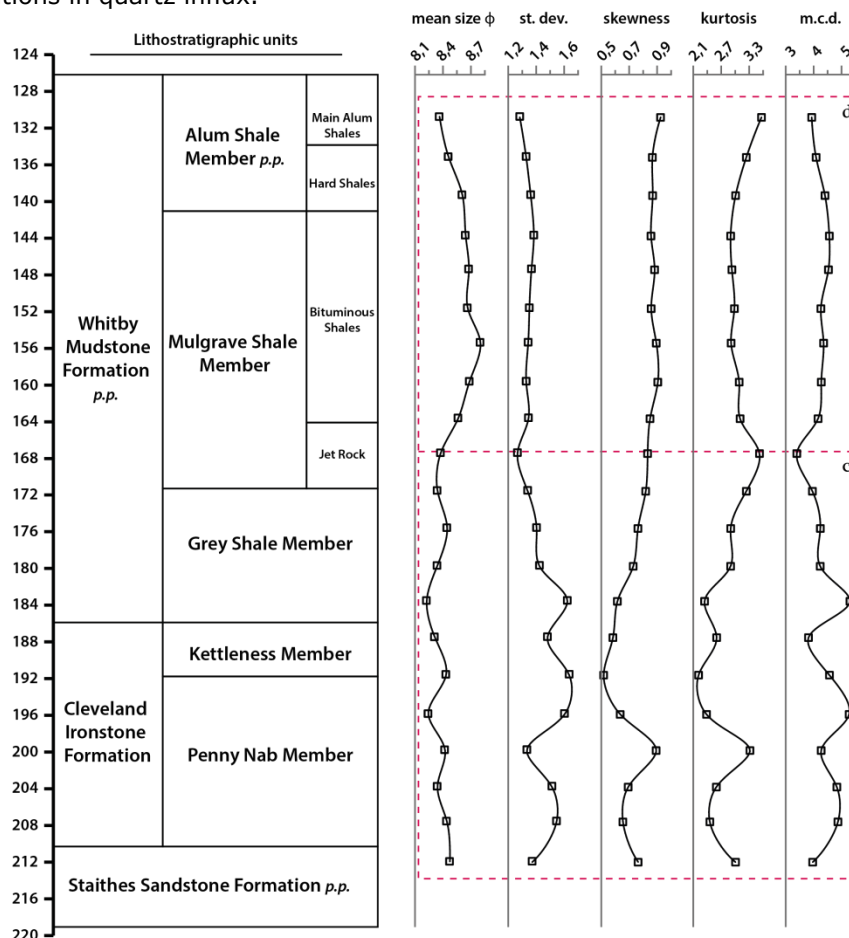


Figure 10) Statistical parameters versus lithostratigraphy and depth. All parameters measured in Φ . Abbreviations: st.dev. = standard deviation; m.c.d. = mean cubed deviation.

The standard deviation, as a measure of sorting, defines the dispersion in the central 2/3 of the distribution curve, while kurtosis provides a comparison of the sorting in the tails of the distribution relative to the central portion. The curves for standard deviation and kurtosis display a near mirror image of each other, meaning that the relative proportion of particles in the tails decreases when sediments become better sorted. In the top part of the core the standard deviation ranges from 1.27Φ to 1.39Φ , while in the lower part it ranges from 1.34Φ to 1.63Φ . The best sorting (i.e., lowest standard deviation) occurs at Jet Rock level. Below this level the quartz grains appear to be less well-sorted and subject to more variability in regards to the sediments deposited above the Jet Rock. This is supported by the results for the skewness of the distributions, displaying its minimum value at the base of the Kettle Member (in agreement with peak input of coarse particles), followed by a gradual increase until no more significant variation occurs in the top section. Furthermore, the consistently positive expression of skewness indicates an excess of fine particles throughout the core, which, of course, is to be expected of quartz input in neritic shales. The mean cubed deviation is a simple parameter in regard to skewness as the former divided by the cube of the standard deviation computes the latter. The mean cubed deviation is however believed to be more effective than any other parameter in separating sands from various origins (*Friedman 1979*), although a similar capability in regard to shales is yet to be established.

4.3 Clay mineralogy - qualitative determination

The identification of specific clay minerals depends on the careful examination of X-ray diffraction patterns. The applied preparations comprise: air-dried, ethylene glycol solvated, and heating to $550\text{ }^{\circ}\text{C}$, of which the results are listed for each individual sample in appendix D. The initial inspection of the results revealed a large degree of similarity in diffraction patterns, indicating comparable mineral composition throughout the core, and enabling an almost 'bulk-identification' type of approach. Presented below are all measured diffraction patterns per preparation type (Figure 11).

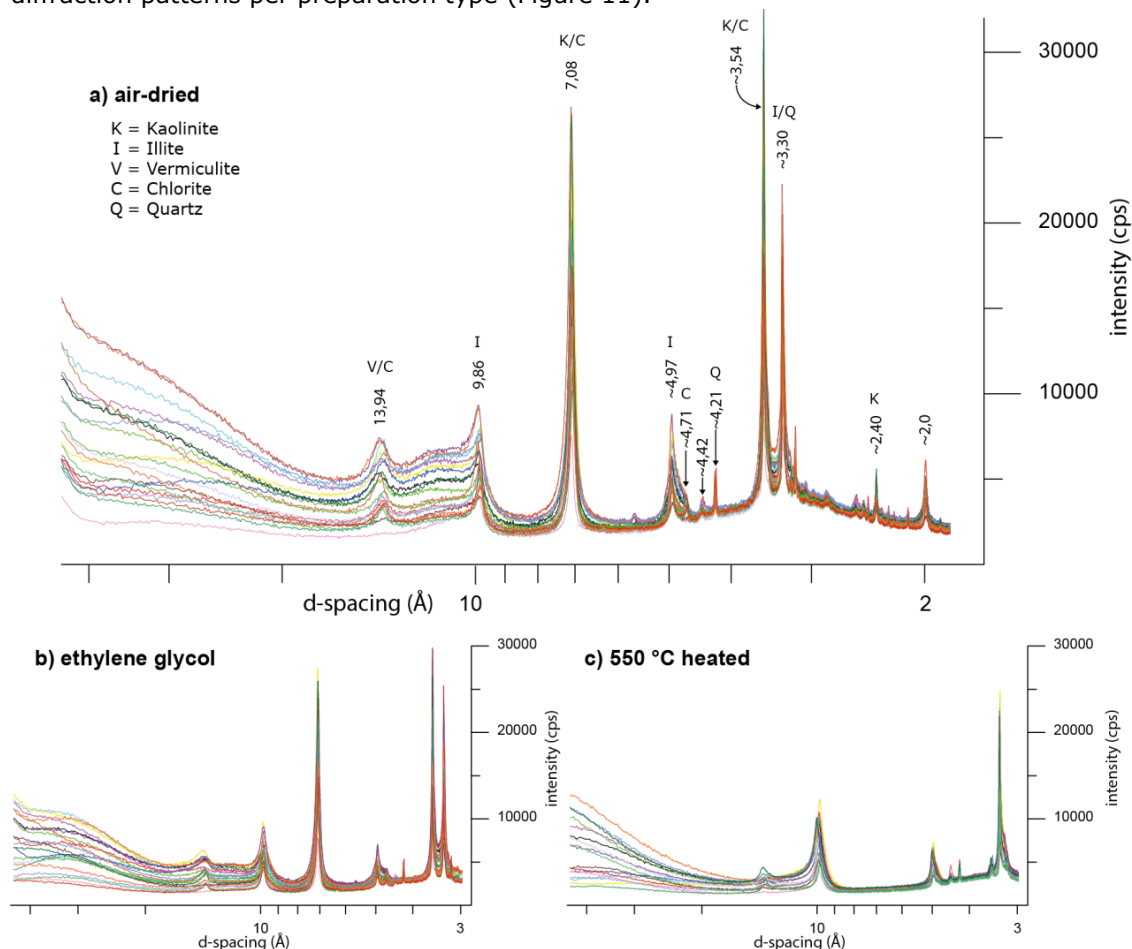


Figure 11) Single plots of all measured X-ray patterns grouped according to preparation type. The air-dried patterns (plot a) display the average peak position in Å for the first order low angle peaks. Higher angle peak positions have been approximated (indicated by ~). Plots b and c show diffraction pattern response to ethylene glycol solvation and 550 °C heating of samples, respectively.

Standard diagnostic analysis of X-ray diffraction patterns relies on the identification of peaks assigned to specific minerals. The first step is to identify any non-clay components from the pattern, after which the remaining peaks are used for the identification of the individual clay components. The most common non-clay constituent is quartz and its presence in the clay fraction is confirmed by the occurrence of a reflection peak at 4.21Å and an intense (shared) 3.3Å peak.

The most prominent peaks correspond to d-spacings of approximately 14, 10, 7, 5, 3.54, and 3.3 Å. The most distinct and high intensity set of peaks is located at c. 7.08Å and 3.54Å and can be associated either with the first and second order reflections of kaolinite or the second and fourth order basal spacings of chlorite. Differentiation between the two is based on reaction upon heating, occurrence of (003) reflections, and kaolinite (002)/(003) ratios. When heated to 550 °C kaolinite becomes amorphous to X-rays and its diffraction pattern disappears, while chlorite (002), (003) and (004) reflections are heavily reduced but not eliminated (*Moore & Reynolds 1989*). Positive identification of kaolinite follows from the (003) reflection at 2.384Å, which is often present in case of very strong first and second order peaks (*Biscaye 1964*), while a chlorite displays a (003) peak at c. 4.74Å. The intensity ratio for kaolinite's (002)/(003) peaks should, according to Moore & Reynolds (*1989*), be about 10. Any higher and a significant contribution of chlorite's (004) peak to kaolinite's (002) peak is to be expected. The measured patterns all appear to comply with the above criteria. The 7.08Å and 3.54Å peaks are totally and near-totally collapsed upon heating, kaolinites (003) reflection is present, and the intensity ratio of the (002)/(003) peaks (above background) is approximately 10. However, despite the positive identification of kaolinite, small amounts of chlorite are likely to be present considering the small peak at c. 4.71Å corresponding to chlorite's (003) reflection and the persistence of a minor peak at 3.54Å after heating.

The second set of reflections at c. 9.86, 4.97 and 3.30 Å are associated with the first, second and third order basal reflections of illite. These reflections remain unaltered upon glycolation and heating, implying the presence of a non-expandable micaceous mineral. The intensity ratios for the 10Å (001) and 5Å (002) reflections ($I_{(001)}/I_{(002)}$) are consistently above 1 and weaker than 2, which is presumed to be indicative of a Mg-rich dioctahedral illite, while simultaneously excluding the possibility of muscovite given its more intense 5Å (002) reflection, resulting in a ratio between 0.7 and 1 (*Thorez 1975*). Although the intensity ratios and relatively broad and asymmetric appearance of the reflections are generally attributed to illite, small amounts of muscovite are probably present, especially given the presence of the undesignated peaks at 4.42Å and 2Å (Figure 11), which might well be an expression of this minor addition.

The peak at c. 13.98Å displays an inconsistent response upon glycolation and heating (i.e., not all samples exhibit the same behaviour). The peak is observed throughout the core, with the exception of the Jet Rock sample at 167.31 m. Apart from a generally slight reduction in intensity, the peak appears to be unaffected by ethylene glycol solvation, indicating the presence of vermiculite and/or chlorite. The distinction between the two minerals is based upon the unique and extensively applied dehydroxylation behaviour of chlorite (*Śröder 2006*). When heated to 550 °C, the (001) reflection of chlorite shifts to a slightly lower spacing and its intensity increases by a factor of 2 to 5 times, while simultaneously higher order (00l) reflections decrease in intensity (*Bailey 1975; Barnhisel & Bertsch 1989*). Vermiculite on the other hand collapses to a spacing of c. 10Å when heated as the lattice contracts due to the exclusion of the interlayer water (*Walker 1975*). Both behaviours have been observed in the core. The upper part of the core (131.75–

171.41 m) shows full collapse of the 14Å reflection upon heating, whereas in the lower part of the core (175.46–211.75 m) these reflections display a minor shift towards lower spacings and a slight reduction in intensity (Figure 12).

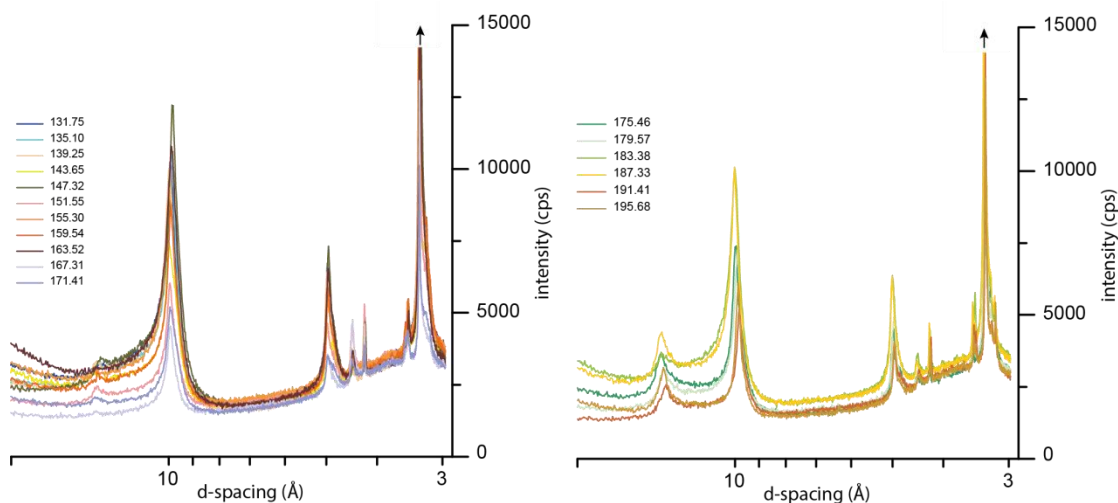


Figure 12) 550 °C heated X-ray diffraction patterns separated according to response upon heating. Samples DN01 to DN11 (131.75–171.41 m depth) on the left show no well-defined peak at 14Å, while samples DN12 to DN21 (175.46–211.75 m depth) show reflections at c. 13.7Å associated with the presence of minor amounts of chlorite.

Although one might be tempted to conclude that the 14Å reflection in the lower part of the core must be assigned to chlorite, vermiculite is probably still the major constituent responsible for this reflection. Because of reasons outlined above, combined with the general reduction in intensity upon heating and the previous indication of the presence of minor chlorite, the expression of the 14Å reflection upon heating in the lower half the core is probably due to a strongly enhanced (001) chlorite peak which usually can be seen even for small percentages of chlorite (*Bailey 1975, 1988*). Therefore, the 14Å is ascribed to vermiculite, with the addition of minor chlorite for samples in the lower part of the core.

The qualitative analysis thus far has revealed that the principle clay constituents, or endmembers, are kaolinite, illite and vermiculite with minor additions of chlorite and muscovite. However, the most striking feature observed in the air-dried patterns (Figure 11) is the 'diffraction band' between the vermiculite 14Å and illite 10Å (001) reflections, indicating the existence of a structure causing an irrational series of reflections over a range of d-spacings. Upon glycolation this diffraction band appears to partially collapse, enhancing the symmetry of the 10Å peak in the process, while heating produces a further enhancement of the symmetry as well as an increase in intensity compared to the natural (air-dried) 10Å reflections. *Thorez (1975)* refers to this type of behaviour as being characteristic of degraded or open illite and indicative of mixed layer structures: some layers have retained their original illitic character while the interlayers behave according to the characteristics of the intermixed component, in this case vermiculite, resulting in the observed resistance to expansion upon glycolation and collapse upon heating. Furthermore, the lack of a superstructure reflection corresponding with a d-spacing equal to the sum of the reflections of the composing minerals, combined with an ill-defined irrational series of reflections expressed in the form of a diffraction band, clearly indicates a randomly interstratified structure (*Thorez 1975; Środoń 2006*) involving illite and vermiculite.

4.3 Clay mineralogy – quantitative analysis

Two different methods have been employed to generate a quantitative estimation of the relative contribution of the kaolinite, illite, and vermiculite endmembers (see section 3.7). The PIHR method is a two-step process which initially determines the contribution of kaolinite and the interstratified species, after which the latter is separated according to peak-height ratio's into contributions of illite and vermiculite. The PHHW method applies

the product of peak-height and width at half-maximum as an estimate for each peak area, after which the total interstratified contribution is determined by the sum of its components. Presented below are the results for both methods (Figure 13).

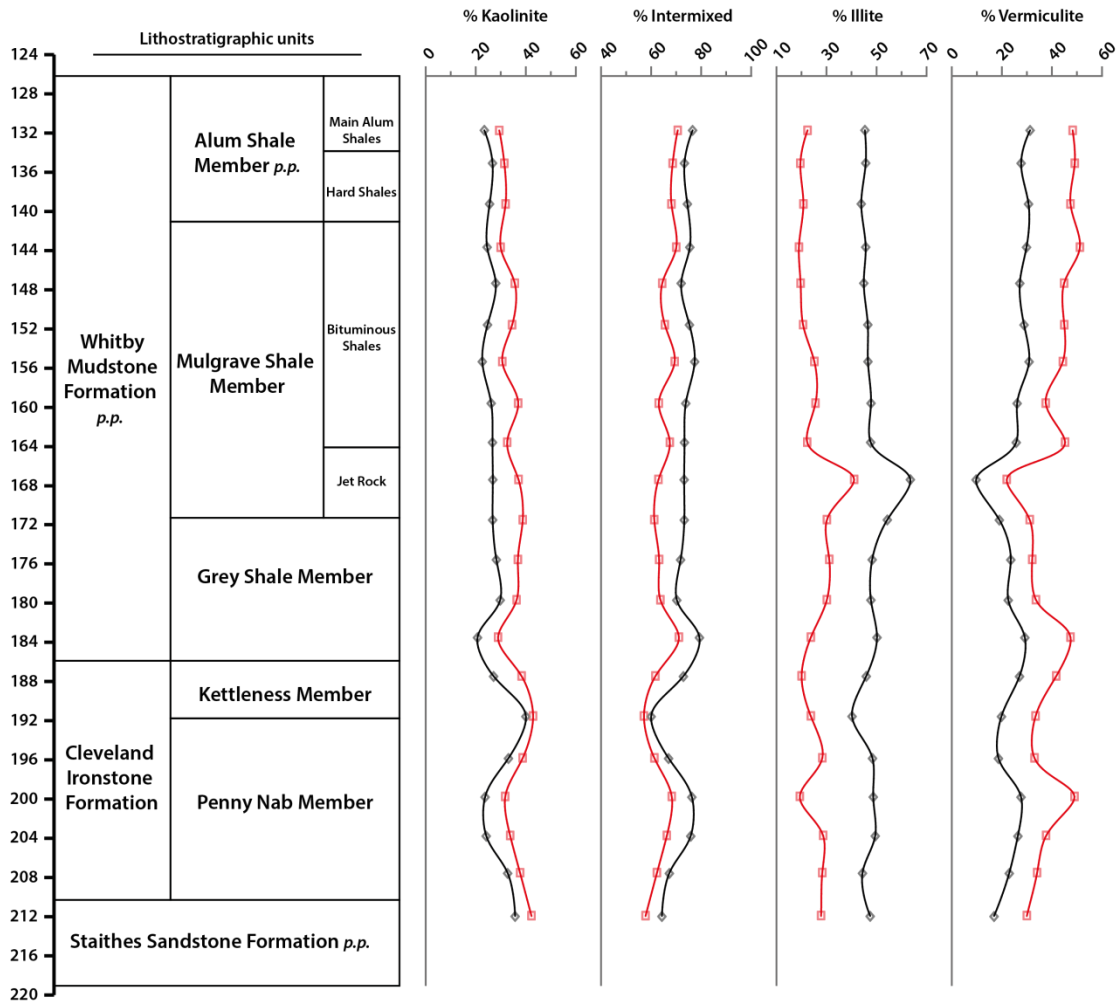


Figure 13) Relative contributions of clay endmembers in percentage of total clay content versus depth and lithostratigraphy. PIHR method in black, PHHW method in red. Note: $\Sigma(\text{kaolinite, interstratified}) = 100\%$ and $\Sigma(\text{illite, vermiculite}) = \text{percentage interstratified}$.

The most immediate and important conclusion from the above results is that both PIHR and PHHW methods closely match in terms of development over the course of the core. The amounts of kaolinite and interstratified species not only display matching trends, but also show similar values. The mean difference between both methods is limited to just 7.51% with a maximum difference of 11.91%, suggesting a fairly precise determination of their respective relative amounts (Table 4). For illite and vermiculite, however, significantly larger deviations are observed. The results for illite display a difference in excess of 22% on average, while the mean difference between both methods for vermiculite approaches 15%. The PIHR method identifies illite as the dominant interstratified species, while the PHHW method denotes vermiculite as the primary interstratified constituent. Although both methods produce similar trends, the standard deviations of the curves show a larger variance for kaolinite and the interstratified species for the PIHR method, while the PHHW method displays larger deviations from the mean for illite and vermiculite (Table 4). Despite these differences, the fluctuations of the clay endmembers are predominately observed in the lower part of the core. From the Bituminous Shales upwards into the Alum Shale Member, kaolinite, illite, and vermiculite fractions remain fairly stable considering the more wavy development in the lower section, culminating in a distinct increase of illite and decrease of vermiculite during Jet Rock deposition.

	PIHR				PHHW				PHHW-PIHR		
	K	IS	I	V	K	IS	I	V	K/IS	I	V
Minimum %	20.74	60.09	40.21	9.85	28.89	57.24	19.13	21.97	2.85	-29.13	8.49
Maximum %	39.91	79.26	63.35	31.22	42.76	71.11	41.04	50.95	11.91	-15.94	21.24
Mean %	27.47	72.53	47.68	24.84	34.98	65.02	25.24	39.78	7.51	-22.45	14.94
St.Dev.	4.46	4.46	4.41	5.31	3.93	3.93	5.29	7.83	2.33	3.64	3.69

Table 4) Minimum, maximum and mean percentages for kaolinite (K), interstratified (IS), illite (I) and vermiculite (V), grouped by method and difference between methods.

Standard deviations (σ) calculated by:
$$\sqrt{\frac{\sum(x-\bar{x})^2}{n}}$$

5. Discussion

5.1 Grain size distributions – process and reliability

The derivation of grain size distributions from thin sections has been a topic of debate since the method was first applied over eight decades ago (*Krumbein 1935*). Discussion on the precise application of the method (e.g., *Chayes 1950, 1951; Krumbein 1950, Greenman 1951a, 1951b*), the relation to other methods, such as sieving (e.g., *Friedman 1958, 1962, 1996; Folk 1966; Johnson 1994, 1996*) and the effects of particle shape and orientation (e.g., *Kellerhals et al. 1975; Schäfer & Teyssen 1987*) has persisted over the years. Although research has been exclusively focussed on sands and sandstones, there is no fundamental reason why the same principles, and limitations, should not also apply to quartz grains found in shales. In regard to this study, the most important issues to be addressed are the effects of: image thresholding, editing of images, grain shapes and the preferred orientation of grains, and the minimum number of particles required to produce reliable grain size distributions.

The process leading up to grain size measurements involves thresholding and editing of the image (i.e., the elemental map). Both are meant to isolate grains, either from the surrounding matrix or from each other. The same threshold was used consistently for all images analysed to ensure uniform data management, while closely spaced grains were separated by making the threshold as 'tightly fitting' as possible, preventing overestimation of grain areas in the process. Any clusters or sets of touching grains remaining had to be edited manually, and although maximum effort is made to prevent multiple grains being analysed as one, it is impossible to guarantee full segmentation of all 'composite grains'. For this reason, maximum grain size measurements are not included in the results, despite their ability to indicate peak hydraulic energy, as editing directly affects the individual determination of the coarsest particle present.

Observations and measurements are performed using a 2D surface and are subsequently converted to 3D grain diameters. This type of area-volume conversion assumes that particles are spherical and randomly organized, disregarding elongated grain shapes and preferred orientation due to mode of transport. Thus, the way the interbedded grains are intersected by the observation surface controls the amount of areal exposure of the grains and hence the accuracy of the resulting apparent grain size. Because the samples of this study are cut perpendicular to their bedding (or at least attempted to do so, as bedding was often unidentifiable), there might be a bias in the grain size distribution depending on the direction of transport in relation to the observed surface. However, *Chayes (1954)* argues that "the estimation of volume composition from areal measurement of randomly chosen samples is entirely free of bias" and that inaccuracy of the results is never related to the basic theory of relating area to volume. In addition, *Kong et al. (2005)* claim that when grains are approximately spherical and the surface of intersection is completely random, a conversion ratio of 1.273 ($4/n$) is valid to convert the 2D mean size of a population to estimate the actual 3D mean size (this relationship is preserved even when using the method of moments). Considering that the mode and direction of transport is unknown, essentially making all intersection surfaces random, and assuming spherical grain shapes, the resulting grain size distributions are most likely a slight underestimation of true size (as no conversion factor was used), while still reflecting a precise represen-

tation of the true shape of the distribution. Although the assumption of spherical grains is obviously not valid (Figure 5), probably due to a lack of mechanical abrasion during transport (i.e., not part of the bedload) of quartz grains smaller than 3Φ (Blatt 1970), it is the most practical way to assess large quantities of grains. The choice to not use the conversion factor of Kong et al. (2005) is philosophical: data should be presented in the most principle form.

To obtain a reliable grain size distribution an adequate sample, in terms of number of grains, is required. For basic analysis, such as the determination of the mean size, 'reasonable estimates' range between 100 to 500 grains (Krumbein 1935; Johnson 1994). However, for more detailed analysis and/or in case of complex distributions, obtaining a reliable distribution may require 1,000 to 1,500 grains (Carver 1971; Kennedy & Mazzullo 1991). The populations obtained from image analysis range from 823 grains on the low end to 4,033 grains on the top end (App. E), meeting the requirements of the above statements for nearly all samples. Taking into account that the same size area was analysed for all samples, there is a striking difference between the top and bottom part of the core. Above Jet Rock level (sample DN10, depth 167.31 m), a significantly higher count is observed than in and below the Jet Rock (Figure 14). Although in the top part the area percentage quartz increases and fluctuates in correspondence with higher grain counts, the mean grain size remains relatively stable, indicating that the increase in grain population is predominately controlled by the influx of material at the finest end of the spectrum (cf. Figure 9).

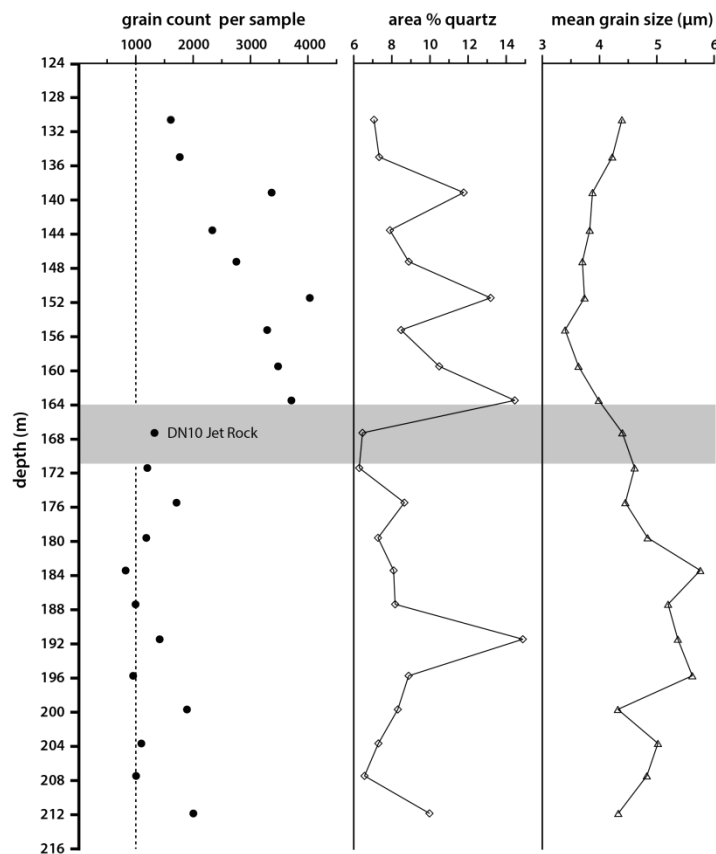


Figure 14) Population numbers (grain count) for all samples versus area percentage quartz silt and mean grain size. Dashed line indicates estimated minimum grain count required for detailed analysis of complex distributions. Grey shaded area indicates the extent of Jet Rock deposits.

5.2 On the determination of grain size parameters by moments

As mentioned in the methods section, the addition of an empty grain size class to close the open distributions is required for the determination of moments. McManus (1988) stresses

that the reliability of the moments decreases rapidly as the proportion of undefined materials increases, and that the method should not be used if a total of more than 1% of the population is unknown, at the risk of obtaining misleading or meaningless results. In light of the previous statement, an attempt is made to test the reliability of the moments method by comparing the mean grain size obtained from direct observation with the mean grain size derived from moments (Figure 15). Unsurprisingly, the mean sizes derived from both methods are different, as the results from direct observation represent a number-length mean, whereas the results from the moments method represent a surface area moment mean (Sauter mean diameter). Nevertheless, the resulting difference between the two measurements might reveal some indication of the accuracy of the moments method and the reliability of parameters derived thereof. Although similar mean grain size trends are obtained by both methods, the difference between the two methods increases with depth. However, this difference may be misleading as the applied methods measure essentially something else. Therefore it may be better to express the mean grain size trends in terms of deviation from their respective preceding samples, that is, as a percentage of fluctuation relative to the sample directly below. The resulting curves show similar development, suggesting that the parameters obtained by moments provide reliable measures. The increased difference with depth and the more pronounced mismatch of the 'fluctuation' curves in the lower part of the core are tentatively linked with reduced grain counts, but these are clearly not solely responsible as neither the deviations nor fluctuations of trends match the development of the grain count. A probably more dominant controlling factor is the increased and fluctuating input of coarser grain size classes with increasing depth, which affects all aspects of the grain size distribution, and

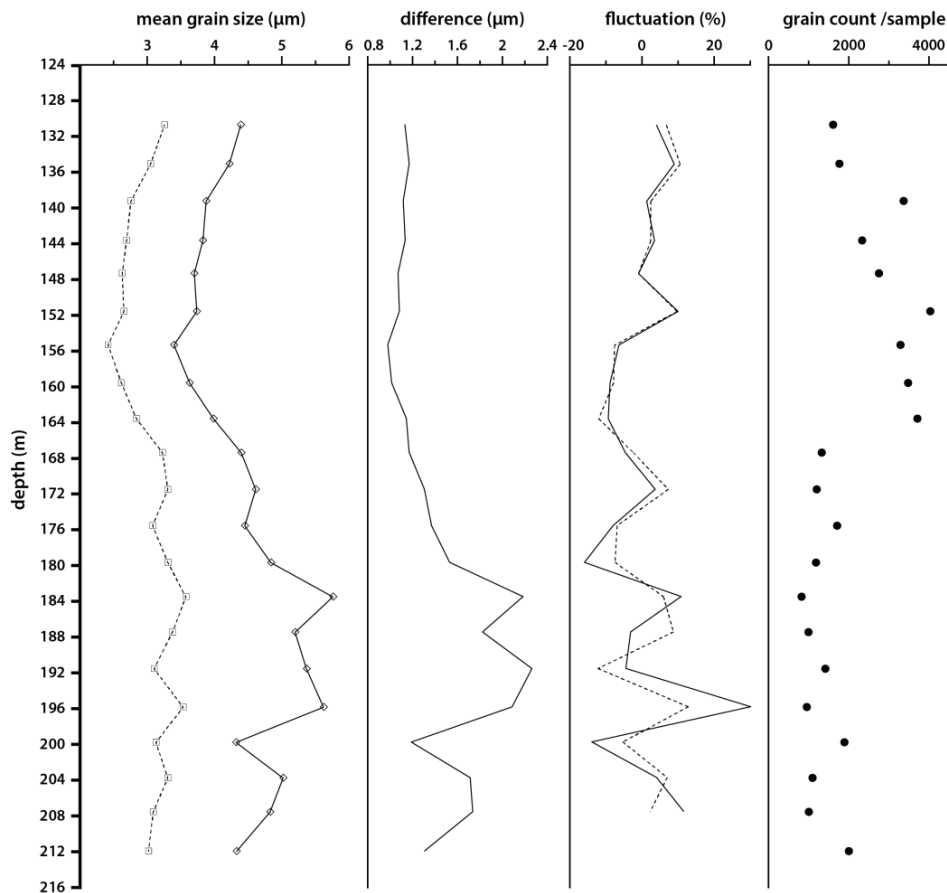


Figure 15) mean grain size measurements from grain size distributions from moments method (dashed line) and observation (solid line) (calculated by: $\frac{\Sigma(\text{grain sizes})}{\text{number of particles}}$).
Grain size in Φ from moments has been converted to microns. Second plot displays difference between methods, third plot the fluctuation with respect to the preceding sample, fourth plot the corresponding population numbers.

hence the parameters derived from moments, as well as the determination of the number-length mean. That being said, sample to sample comparison of grain size parameters seems to be viable and reliable, although the uncertainty increases slightly below approximately 180 meters depth.

5.3 Clay mineralogy – notes on qualitative analysis

Qualitative clay mineral determination resulted in the identification of kaolinite, illite, and vermiculite as the principle components of the clay fraction (<4 μm). Muscovite and chlorite (in the lower part of the succession), are present in minor amounts. Randomly interstratified illite-vermiculite, expressed by a 10–14Å diffraction band, is also present. This type of disordered system is usually examined using Méring's model (1949), which states that the (00l) reflections of mixed-layer minerals are located between the diffraction peaks of their components and positioned according to the relative contribution of each component to the mixed-layer system, resulting in a composite or compromise of the two endmember reflections (Moore & Reynolds 1989; Sawhney 1989). However, due to the wide angular range between the 10Å illite and 14Å vermiculite peaks, only a broad band is observed and a clear apex is missing. In such case (regions broader than $c. 3^\circ 2\theta$), changing proportions of layer types cause one of the endmember reflections to diminish, and the other to increase in intensity, while no intermediate peak is observed (Reynolds 1980). Furthermore, Reynolds (1988) argued that, Méring's principle of peak position behaves best at the middle of the compositional range between endmembers, rendering Méring's principles incompatible for diagnostic quantitative analysis when one endmember is significantly more dominant or when a well-defined peak is missing.

Although Méring's method is thus unsuited for quantitative analysis concerning this study, it can be used to determine whether the chlorite in the lower ten samples (DN12–DN21; Figure 12) is part of the interstratified structure or present as a discrete mineral. Most interstratified systems usually only consist of two components, but three-component systems have been reported (e.g. Weaver 1956; Drits et al. 1997) and might even be very common (Sakharov & Lanson 2013). Because vermiculite has only one primary reflection at 14Å, while illite and chlorite both have series of basal (00l) reflections, higher-order reflections of illite should be affected by chlorite interference, if chlorite were to be part of the interstratified structure. However, no such effect has been observed. Hence, the absence of displaced reflections and occurrence of just one diffraction band in the 14Å–10Å region indicates two-component interstratification of illite with vermiculite. Chlorite can be excluded as a third component, due to the lack of displaced higher order illite reflections, and is thus present as a discrete mineral non-interfering with the interstratified structure.

5.4 Clay mineralogy – notes on quantitative analysis

As mentioned above, Reynolds (1980) found that the intensities of endmember reflections are inherently linked to the relative contribution of each species to the interstratified structure. The procedure of the PIRH method for quantifying the relative contributions of illite and vermiculite exploits this link, as contributions of illite and vermiculite to the total interstratified structure are based on peak-intensities. Although the PHHW method also employs peak-intensities, it perceives the interstratified structure as discrete phases, and fails to utilize the entire interstratified 'structure' or interconnected zone (Figure 8). The difference between the two methods is pointed out by the identification of the dominant interstratified species: the PHHW method indicates vermiculite to be more abundant, while the PIRH method accredits illite. Closer inspection of the background corrected data shows that the bulk of the area of the interconnected zone, or diffraction band, between illite and vermiculite is concentrated at the higher-angle region of the pattern (Figure 16). Apparently, more of the random stratified layers (and interlayers) produce reflections in the vicinity of illite than vermiculite, indicating that illite is the main controlling phase of the interstratified structure (in agreement with Méring's principles). It is therefore presumed that the PIRH method in this context is the most accurate, as it succeeds to identify the primary constituent: illite.

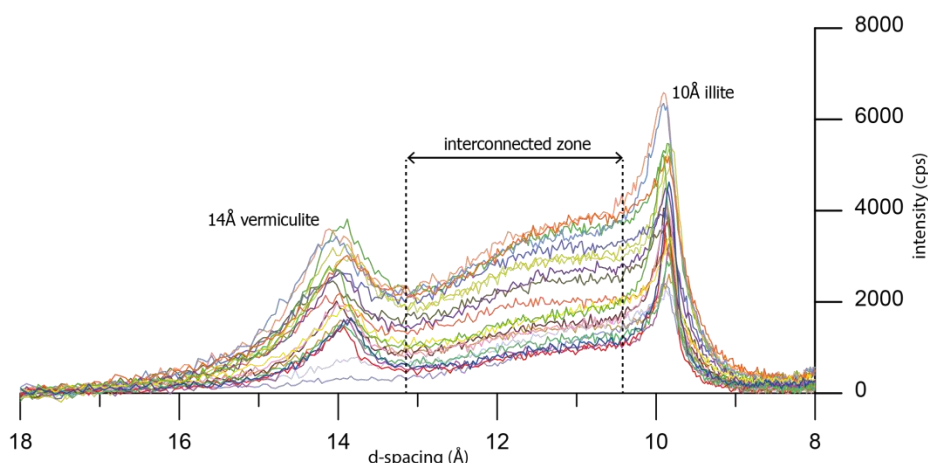


Figure 16) Zoom in of background corrected diffraction band (all samples). The interconnected zone between illite and vermiculite swells towards the high-angle region, indicating that the irrational series of reflections produced by random interstratification of the two pure phases is of predominant illitic character.

The use of two different methods for quantitative analysis was aimed at providing some constraint on the precision and accuracy of the results. Although the PIHR method is considered to be more accurate than the PHHW method, it remains unclear how much (if any) the results deviate from the absolute quantitative amounts. However, as argued by Hughes et al. (1994), there is often no need to know the absolute quantities of the minerals present, as semi-quantitative analysis (or “quantitative representation”) is perfectly suitable for obtaining relative properties of soils and reliable estimates of weathering intensities, as long as the precision of the method is high. The precision, or reproducibility of results, is represented by the relative sample to sample comparison, or trend, obtained by each method. Thus, although discrepancy exists between the two methods in terms of accuracy and there is no measure of uncertainty, the precision of both methods is validated by the matching trends produced by both the PIHR method and the PHHW method (Figure 13).

5.5 Provenance of quartz grains

For the purpose of environmental interpretation, the most primary determination is the differentiation between silica particles from biogenic, authigenic and detrital origin. As only allochthonous grains are of interest in respect to depositional processes, other sources have to be either excluded or quantified before accurate assessment of depositional environment is possible. The authigenic origin of quartz is usually assessed by cathodoluminescence differences with respect to quartz from detrital origin (e.g., Milliken 1994; Schieber et al. 2000; Milliken et al. 2016). However, given the high recycling rate of sedimentary rocks (Blatt & Jones 1975), even authigenic formed quartz grains may be indicative of sedimentary processes, as their erosion and subsequent redeposition makes them essentially detrital (Blatt 1987). The following discussion is meant to point out the principle detrital origin of quartz in the studied shales, although minor additions from other sources cannot fully be excluded.

Biogenic (opaline) silica is derived from biota constructing siliceous skeletons and are produced by diatoms, silicoflagellates, siliceous sponges and radiolaria (DeMaster 2002). Although the earliest reported diatoms are of Toarcian age (Rothpletz 1896), and today they are present in almost all aquatic and most wet terrestrial habitats (Sims 2006), they are an unlikely source of silica in regard to the studied section. Despite their Toarcian aged first occurrence, the first well defined diatoms are of Early Cretaceous age following an explosive Lower Cretaceous radiation, while only four species are known from the Jurassic (Philippe et al. 1994). It seems therefore implausible that diatoms are contributing on any significant scale to the observed silica particles, especially given the lack of reported large-scale diatom populations during the Early Jurassic. Silicoflagellates can be easily excluded

as a source of biogenic silica as their first known occurrence is reported to be from the late Lower Cretaceous Albian stage (*McCartney et al. 1986*). Siliceous sponges are another unlikely source of silica. In contrast to the peak sponge diversity of the Late Jurassic and major build-up of reefs over a vast area spanning from the northern margin of the western Tethys (present day Spain) to SE France, Switzerland, SW Germany, Poland and Romania (*Rigby 1971; Ghiold 1991*), siliceous sponges from the Early Jurassic are considered uncommon (*Schubert et al. 1997*) and only few occurrences (High Atlas, Morocco, Western Lombardic Alps and Turkey) have been reported (*Hartman et al. 1980*). This geographic distribution and lack of Early Jurassic 'sightings' combined with the rapid burial required to prevent dissolution before preservation (*Mock and Palmer 1991*), suggests that the probability of any significant biogenic input of silica derived from siliceous sponges is highly remote. Contrary to biota described thus far, radiolaria have existed since the Cambrian and were subject to an extinction interval during the Late Pliensbachian to Early Toarcian (*Goričan et al. 2013*), suggesting reduced abundances as species extinction out-paced the speciation of new species. The skeletons of radiolaria range in size from 50 to 200 µm and where more robust and of higher average weight during the Mesozoic compared to their Cenozoic counterparts, as competition for dissolved silica with diatoms is suggested to have had a major impact on radiolarian evolution since the Cretaceous (*Casey 1993*). Although radiolaria show widespread global presence during Late Pleinsbachian to Toarcian times, they appear to be simply too large to account for particles in the grain size distribution as reported species are all in excess of a 100 µm in size (*Plate 1 Carter et al. 2010*). Furthermore, the shallow water epicontinental setting of the Cleveland basin during the Jurassic contrasts with the preferred oceanic environments of radiolaria, which appears to have been the cause for an absence of radiolaria in the Jurassic deposits of the UK area (*Cox 1990*). A final biogenic source of silica-silt is proposed by Pike and Kemp (*1996*), claiming that silt aggregates might not be detrital but are actually (collapsed) agglutinated groups of foraminifera. However, the BSE images provided by Pike and Kemp (*1996*) show very different textures compared to the elemental silica maps produced by SEM-EDX for this study (App. B), hence the wrongful identification of detrital quartz due to the presence of agglutinated foraminifera appears improbable.

With biogenic sources of silica eliminated, the only remaining source besides detrital silica from authigenic origin. Although precipitation of quartz is generally associated with the dissolution of unstable opaline silicon from biogenic sources, pore waters may also contain silica from alteration of volcanic ash, dissolution of silicate minerals, and diagenetic transformations of smectite to illite or recrystallization of illite to muscovite (*Schieber 1996*). Since no volcanic ash layers are reported from the studied succession, any authigenic quartz must be derived from either, or a combination of, dissolving feldspars, pressure solution of quartz, or clay mineral transformations. The latter is commonly viewed as the most important source of silica release in shales and mainly involves the transformation of smectite to illite (*Hower et al. 1976*). Since no smectite is currently present in the succession, either all smectite is transformed to illite, or it was never part of the initial clay mineral assemblage. To complete the transformation for 95–99%, sediments have to experience burial temperatures over 200–300 °C (see *Merriman & Frey 1999, Figure 3.4*). This is far in excess of even the deepest burial estimates of Lias deposits in the Cleveland Basin under a 'normal' geothermal gradient of 35 °C/km (see section 5.6) and simultaneously disqualifies the recrystallization of illite to muscovite as a possible silica source on the same basis (i.e., requires even higher temperatures; *Merriman & Frey 1999*). Clay mineral transformations can therefore be excluded as a source of authigenic silica, which is in concurrence with previous findings that the lack of smectite in Lias sediments is due to depositional absence, rather than due to removal by diagenetic processes (*Hallam & Sellwood 1968; Sellwood 1972*). This leaves the dissolution of feldspar and quartz as the only remaining source of authigenic silica, and, due to their omnipresence in shales, the most probable. Boles & Franks (*1979*) found that the apparent breakdown of K-feldspar takes place between 100–120 °C, which is well within the range of estimated burial depths for the studied sediments. The associated potential silica release is 40–45 wt. % of the dissolved feldspar, while the dissolution of quartz results in a silica

loss of about 4–9% at temperatures up to 200 °C (*van de Kamp 2008*). It is therefore probable, if not inevitable, that at some point the pore waters contained dissolved silica. Whether the secondary quartz precipitated within the shale itself (closed system; *Hower et al. 1976*), or was expelled to interlayered silty laminae (e.g., *van de Kamp 2008*), is unknown. However, according to *Blatt (1987)*, diagenetic quartz seems to crystallize as particles below 2 µm in size, meaning that they are unlikely to significantly affect the measured grain size distributions as the lower limit is set at 1.77 µm. Furthermore, the angular shapes of quartz grains means that grain modification due to quartz overgrowth is unlikely and indicates a predominately detrital origin (*Pye & Kringley 1986; Schieber et al. 2000; Williams et al. 2001*).

5.6 Origin of clay mineral assemblage

The required general assumption in the application of clays deposited in the marine environment as indication of source-area climate, is that the clay mineral assemblage formed in continental soils is eroded, transported, deposited, and preserved, while maintaining its original composition even during diagenetic processes with burial. The assumptions, processes, and difficulties associated with this general concept are extensively reviewed (e.g., *Singer 1980, 1984; Eberl 1984; Curtis 1990; Wilson 1999; Thiry 2000*), and for that reason, will not be discussed here, but are referred to if required. To infer paleoclimate conditions from the clay content of the studied sediments, it is imperative to establish whether the determined clay mineral assemblage represents the original detrital input or the altered products of post-depositional changes (*Singer 1980, 1984*). Since clay mineral modifications during transport and deposition are thought to account for only minimal changes in composition in response to transformation and neoformation (*Eberl 1984, and references therein*), the following discussion will focus on the burial history of sediments to verify the principal detrital origin of the clay mineral assemblage.

The burial depth of the Cleveland Basin Lias sediments was recently investigated and reviewed by *Kemp et al. (2005)*, combining regional variations in clay mineral assemblages and smectite-illite reaction progress with data of Middle Jurassic fluid inclusion micro-thermometry from sphalerite grains (*Hemingway & Riddler 1982*), vitrinite reflectance (*Barnard & Cooper 1983*), and detailed modelling (*Holliday 1999*). The results indicate that the Lias Group of the Cleveland Basin was buried to a minimum of c. 2.7 km (*Hemingway & Riddler 1982*) and maximum of c. 4 km depth (*Kemp et al. 2005b*), implying that the temperatures endured by the sediments, using a geothermal gradient of 35 °C/km, range between c. 95–140 °C. Although these temperatures are high enough to induce clay mineral transformations, obscuring or even destroying any paleoclimatic signal potentially preserved, there is one fundamental difference: the smectite-illite reaction progress employed by *Kemp et al. (2005b)* to infer temperature and depth cannot be applied to the sediments of this study, as no (illite-interstratified) smectite is present in the succession. In addition, there is no diagenetic reaction pathway known, other than the transformation of vermiculite to illite through a mixed-layer phase in alkaline conditions mentioned by *Shaw (1981)*, that may explain the dominance of irregularly interstratified illite-vermiculite as a product, or diagenetic evolution (*Środoń 1999*), of its discrete phases or transformation of other minerals. In fact, most studies regard the Lias Group sediments as being detrital (e.g., *Sellwood & Sladen 1981; Deconick et al. 2003; Jeans 2006; Dera et al. 2009*). Although some evidence exists that diagenetic development of authigenic kaolinite took place in the Cleveland Basin (*Pye & Kringsley 1986*), diagenetic changes are considered to be subordinate to depositional environment in affecting the nature of the Mesozoic clay assemblage (*Shaw 1981*). Therefore, it can be concluded that the clay mineral assemblage mainly reflects weathering intensity and pedogenesis of the source area, and can be used as a paleoclimatic proxy, as it predominately represent soil detritus eroded from adjacent emergent land masses.

5.7 Quartz content and clay mineralogy versus geochemistry

The detrital input of the late Pliensbachian–early Toarcian sedimentary succession of this study has previously been evaluated by determination of detrital flux using silicon, titanium, and zirconium elemental concentrations normalized to aluminium (Atar 2015). The resulting proxies are associated with input of detrital quartz or biogenic silica (Si/Al), and the input of clay and heavy mineral fractions of the sediment (Ti/Al, Zr/Al). The comparative results from both studies are listed below (Figure 17).

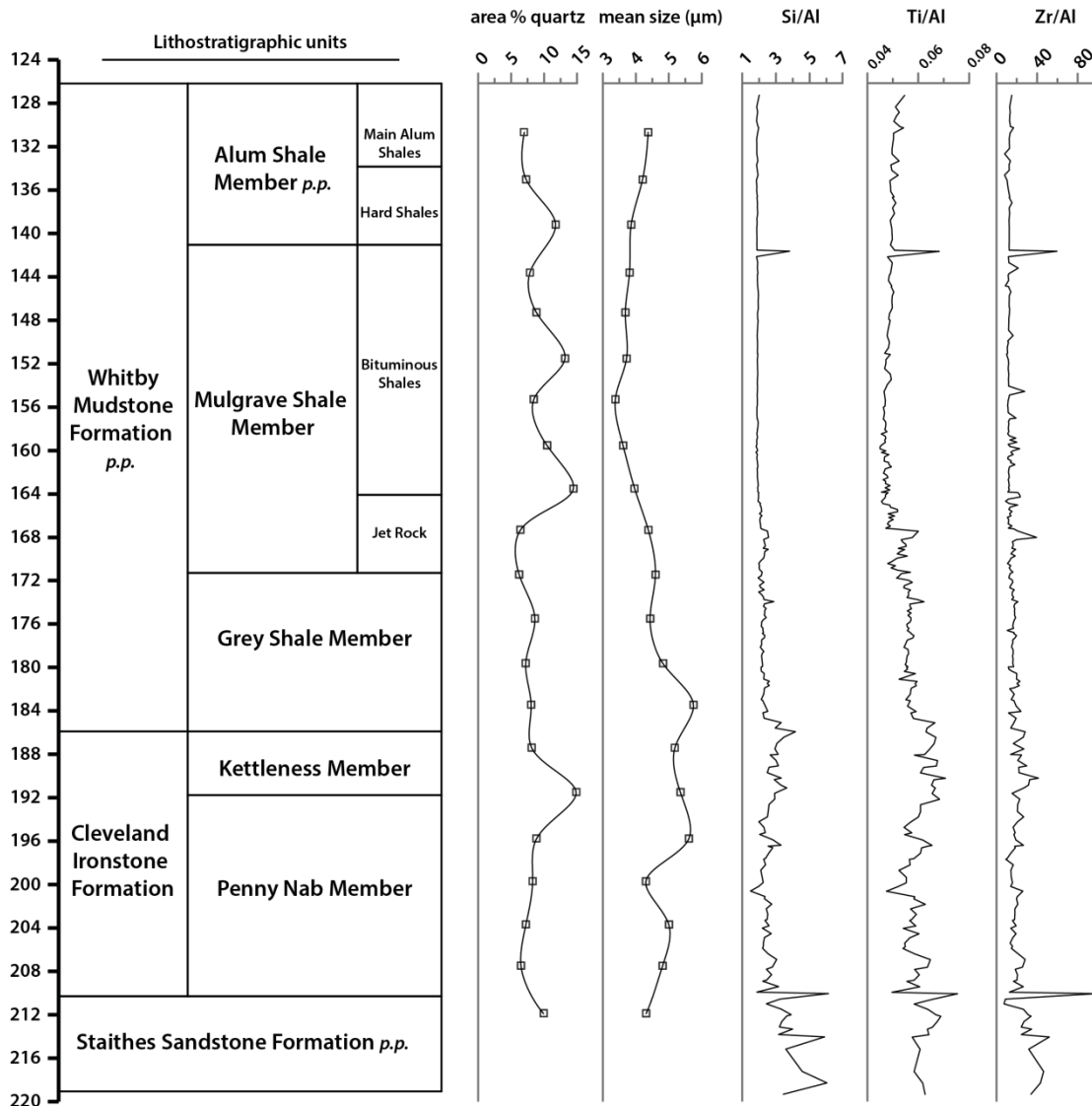


Figure 17) Area % quartz and mean grain size versus detrital proxies of Atar (2015).

What immediately becomes clear, is that, although in principle both data sets should display matching trends in regards to detrital flux, there is no apparent link between the measurements performed by Atar (2015) and the quartz input (area % quartz, Figure 17) observed in this study. Whereas the detrital proxies show most variation in the lower section of the core followed by a distinct reduction in concentrations and increased stability from approximately 168 m depth upwards, the quartz input observed in this study shows increased values and enhanced variability for the same sediments. This discrepancy between the two datasets is difficult to reconcile, but probably originates from the fundamentally different approaches used for their determination: they essentially measure different things. The geochemical proxies represent the bulk chemical composition of the sediments normalized to an 'immobile' component (aluminium), whereas the area % quartz is a direct observation of the shales components, that is, the SiO₂ content exclusively associated with quartz grains. Another possible explanation is that the

fluctuations in quartz content (area % quartz) may be due to quartz concentration in thin discrete layers (Atar 2016, personal communication). However, considering that the fluctuations show periodicity and similar amplitudes, it seems unlikely that the sampling process would repeatedly encounter discrete silt horizons within a succession of uniform shales. In addition, there is no complementary evidence from the grain size distribution to support such a conclusion, other than some minor input of coarse quartz silt particles at 151.55 and 163.52 m depth (Table 3). In regard to the objective of this study, Williams et al. (2001) states that, with respect to sequence-stratigraphic interpretation, the direct and quantitative measure of grain size of the terrigenous component alone (in this case the SiO₂ of quartz grains) is superior to a proxy. Despite the difference between the two datasets, a common characteristic is a change in bottom versus top core behaviour in trends, dividing sediments preceding the T-OAE (~Jet Rock level) from sediments succeeding the event. This is a clear indication that, whatever the cause for the incongruity between the datasets, evidently some major change occurred in the depositional environment that persisted even well after the conclusion of the T-OAE.

As part of the geochemistry, Atar (2015) also determined the abundance of redox-sensitive trace metals. A selection of the associated proxies (normalized against aluminium) are listed and compared to the clay mineralogy (Figure 18), to investigate their potential interdependency. The results are in agreement with the previously presumed minimal effect of transformation and neoformation on the clay mineral composition (section 5.6), as none of the trends displayed by the redox proxies show resemblance to the development of the clay mineral assemblage. The suggestion that the clay minerals are unrelated to the redox state of the water column and sediment pore waters, further underlines the detrital origin of the clays, and strengthens the interpretation that the clay composition is the unaltered product of eroded soil detritus from the source area.

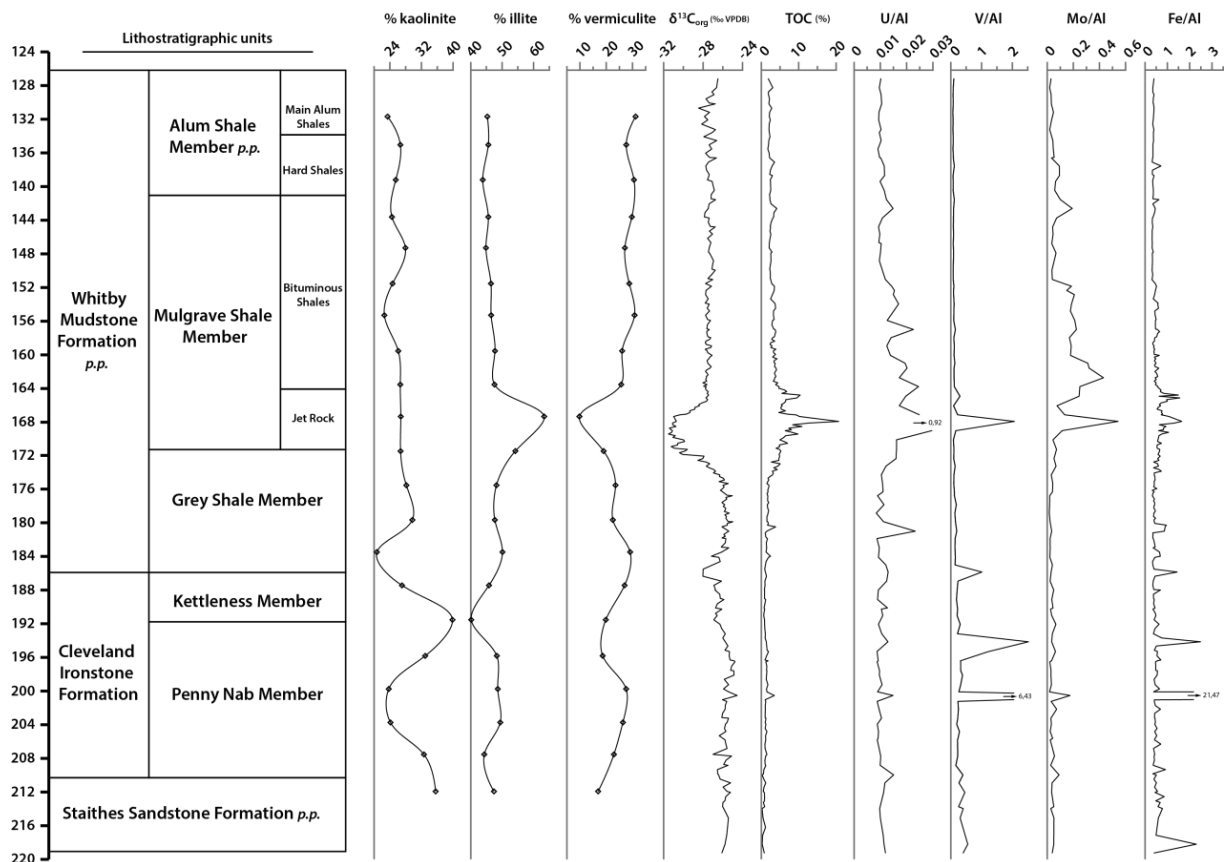


Figure 18) Clay mineralogy (from PIHR method) versus carbon isotopes ($\delta^{13}C_{org}$), total organic carbon (TOC), and redox proxies of Atar (2015).

5.8 Paleoclimate interpretation from clay mineralogy

The main components of the investigated late Pliensbachian–early Toarcian clay mineral assemblage are kaolinite and irregularly interstratified illite-vermiculite (I/V), with a notable minor addition of chlorite at 175.46–211.75 m depth. This is in a broad sense consistent with other studies concerning the Upper Lias sediment of the Cleveland Basin (*Sellwood & Sladen 1981; Jeans 2006*), although they fail to explicitly point-out the dominance of the I/V phase. The exception is the study of *Kemp et al. (2005b)*, who identified illite-smectite as the interstratified species, although they acknowledged that their modelling of XRD traces was hindered by almost complete overlap of peaks from different clay mineral species.

According to *Chamley (1989)*, the relative abundance of kaolinite in Jurassic rocks suggests warm temperatures and near constant annual humid conditions on landmasses, as kaolinite has a strong climatic dependence controlled by the intensity of continental hydrolysis. Consequently, kaolinite variation during the Pliensbachian–Toarcian period is believed to be related to the latitudinal zonation of hydrolysing conditions and is considered a reliable paleoclimatic proxy for the Early Jurassic, showing enrichment during warm episodes due to enhanced weathering and depletion during cool and dry conditions in response to diminished hydrolyses and leaching (*Dera et al. 2009*). Following this line of reasoning, the climate varied between warm-wet and cold-dry during the late Pliensbachian and start of the Toarcian, after which it stabilized at c. 180 m depth (Figure 18). This is in contradiction with the general view that during the T-OAE (~Jet Rock) a severe climate perturbation took place, evidenced by major TOC enrichment and a profound carbon isotope excursion (Figure 18). Since the variation in kaolinite does accurately reflect the cooling event during the Pliensbachian–Toarcian transition (*D. Spinatum Zone; Dera et al. 2009*), the lack of kaolinite fluctuation pre- and during the T-OAE probably reflects increasing distance to shore due to differential settling and in response to transgression (Figure 4; *Sellwood 1972*). Therefore, it appears, at least for the section above c. 180 m, that kaolinite is no valid paleoclimatic proxy for the studied succession, and any interpretation of paleoclimate should be based on (the more dominant) presence of I/V and the respective variation of its endmembers.

Illite and irregular interstratified clays, including vermiculites, are commonly associated with weathering of granitic and acid metamorphic rocks under cool to temperate climate (*Chamley 1989*). Illite abundance is associated with weak weathering intensities (i.e., weak pedogenesis) and increased levels of mechanical weathering, implying continental erosion (*Singer 1984*). From the perspective of illite, the climate is thus fairly stable over the course of the succession, except for a profound increase during the carbon isotope excursion. The implied increased levels of continental erosion during this event match the increase of continental weathering rates suggested by *Cohen et al. (2004)* based on osmium isotopes. Apparently, the relative amount of illite in the interstratified structure with vermiculite is still able to preserve a paleoclimatic signal despite not being present as a discrete mineral. The reason for this must be contained within the process of I/V formation itself, as the signal is clearly terrestrial in origin.

The formation of vermiculite most likely results from the transformation of illite and/or chlorite through a phase of interstratification, which is supported by soil profiles showing increasing vermiculite content towards the surface accompanied by a simultaneous decrease of illite (e.g., *Millot & Camez 1967; Lin et al. 2002*). Since the full transformation process also involves the development of montmorillonite from discrete vermiculite (e.g., *Jackson et al. 1952; Millot 1970*), the absence of both of these clay phases probably indicates more temperate and less intense weathering (*Millot & Camez 1967*). This means that the I/V clays either resulted from conditions that favour the formation of metastable intermediates of interstratified I/V (*Hong et al. 2014*), or that soil erosion and pedogenic formation of I/V occurred at similar rates, preventing the transformation process to proceed to a more advanced phase. Thus, if the abundance of vermiculite is taken as a measure of the degree of completeness in the transformation from illite, indicating more

intense weathering (i.e. warmer climate) with abundance, the climate varied slowly over the course of the late Pliensbachian and beginning of the Toarcian, while indicating stable and warmer climate on average during the top part of the succession. The profound reduction of vermiculite during the T-OAE coincides with the increased rate of erosion inferred from illite and probably signifies deeper erosion of soil profiles, meaning that I/V clays less advanced in the transformation from illite were exposed and subsequently eroded and deposited in the marine environment. Therefore, there is no need to invoke a change to colder climate during the major environmental perturbation of the Toarcian.

More specific climatic constraints can potentially be derived from the present day distribution of I/V mixed clays. Contemporary I/V clays are present in soils from China (*Jackson et al. 1952*), the United States (*Rich 1958*), France (*Millot & Camez 1967*), New Zealand (*Churchman 1980*), Scotland (*Bain et al. 1990*), Russia (*Bonifacio et al. 2009*), and the local (sub-) alpine soils of Taiwan (*Lin et al. 2002; Liu & Cheng 2004*). The soil type encountered at all of these sites are podzols or spodosols, depending on the classification system of use. The apparent suggestion is that, since I/V is almost exclusive found in this single soil type, fairly specific climate condition may be ascribed to their formation. The combined suggestion from the studies listed above, it that I/V typically forms from the transformation of illite and/or chlorite due to the release of interlayer potassium in temperate acidic soils under cool temperature regimes with high precipitation rates. More specifically, *Lin et al. (2002)* reported soil temperatures between 8–15 °C with precipitation exceeding 3000 mm/y, while *Bonifacio et al. (2009)* reported mean annual temperatures of 4 °C with a precipitation of 731 mm/y. Thus, although these conditions vary considerably, the importance of significant precipitation rates for the formation of I/V is evident (*Barshad 1966*). However, clay mineral composition depends on a complex interplay between local petrography, precipitation, drainage, and temperature, meaning that podzolization is not limited to cool and humid climates, but may also develop under temperate and warm climates providing that siliceous substrate and sufficient drainage is present (*Chamley 1989*).

Summarized, the clay mineralogy of the late Pliensbachian–early Toarcian Cleveland Basin suggests that the paleoclimate was characterized by temperate-warm temperatures with high precipitation rates and podzols as the main soil type. During the late Pliensbachian and start of the Toarcian, the climate varied slowly until the initiation of the T-OAE. After this event (c. 164 m depth), the climate stabilized at, presumably, warmer and more humid conditions than prior to the climatic perturbation. Although its origin is unknown, the minor addition of chlorite in the lower part of the core, and its subsequent disappearance, is probably an expression of the climatological transition, suggesting that the boundary between variable and 'stable' climate is located somewhere between 175.46–171.41 m depth.

5.9 Depositional environment and sequence stratigraphic perspectives

The change in environment and climate between the lower and upper part of the succession identified above (sections 5.7, 5.8), is supported by the parameters derived from the moments method. Cross plots of these results show an apparent differentiation between samples from the lower and top part of the section, although the boundary is placed slightly lower than before (see Figure 10, section 4.2, and Figure 9) beneath Jet Rock level in the range of 171.41–175.46 m depth (Figure 19).

The pronounced grouping in the top part of the succession shows that the sediments are generally better sorted (standard deviation <1.4) and grain size distributions are less symmetrical (skewness >0.8), than the sediments found in the lower part of the core. The consistent presence of sample DN18 (199.61 m depth) in the grouping suggest temporary similar depositional conditions during the Penny Nab Member as in the top of the succession. The isolated appearance of DN10 (167.31 m depth) in plots C, E, and F, is due to lower values for the mean cubed deviation. The higher environmental sensitivity of this parameter in sands suggested by *Friedman (1967, 1979)* therefore also seems to apply to

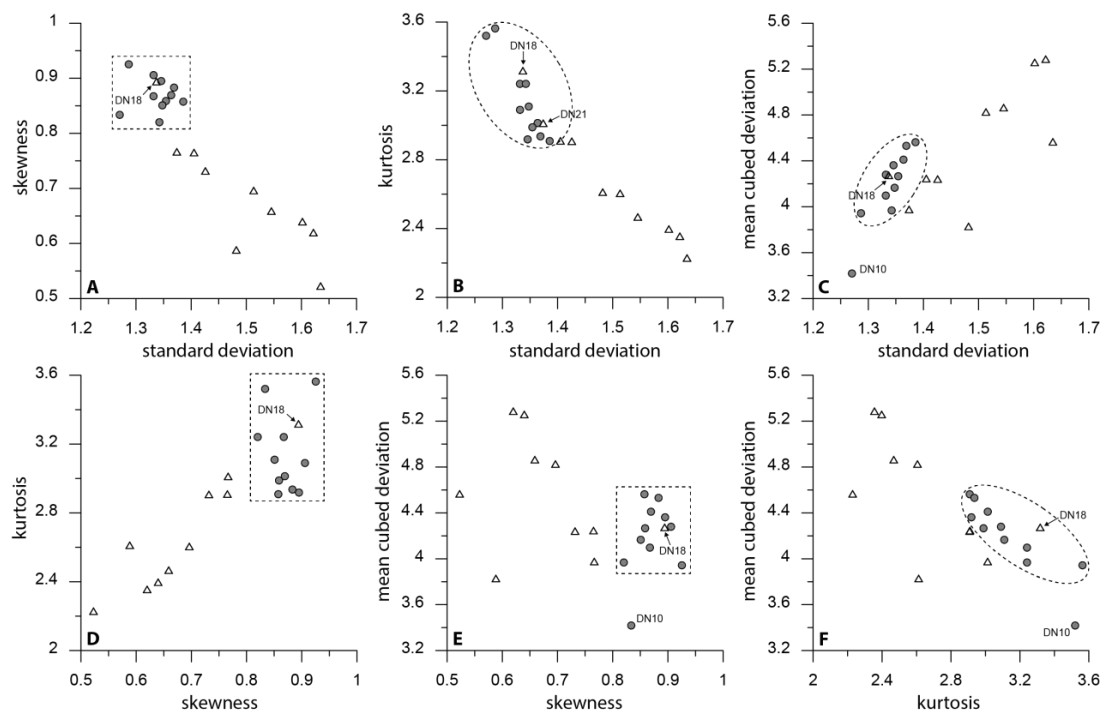


Figure 19) Cross plots of parameters derived from moments method. Circles indicate top core samples (130.75–171.41 m depth), triangles bottom core samples (175.46–211.75 m depth). Consistent outliers are sample DN18 (199.61 m depth) and, in lesser extent, sample DN10 (167.31 m depth; Jet Rock) as indicated in the plots.

shales, since sample DN10 corresponds with the deposition of elevated levels of total organic carbon during the T-OAE (Jet Rock, Figure 3). Combined, the resulting implications are: (i) the quartz fraction in the lower part of the succession resulted from depositional processes that were inherently variable, (ii) a shift occurred to a stable depositional setting, (iii) this switch took place before the onset of the T-OAE (Jet Rock) between 175.46–171.41 m depth, and (iv) the Jet Rock depositional setting is similar to the other sediments of the top part of the succession, but environmentally different.

The quartz content and mean grain size of shales has been suggested to yield meaningful indications of shoreline proximity and sequence stratigraphy (Blatt & Totten 1981; Macquaker & Taylor 1996; Macquaker et al. 1998; Williams et al. 2001). Although some have implied that quartz content and mean grain size are closely connected (Blatt & Totten 1981; Williams et al. 2001), the results of this study appear to be completely unrelated. The uncontested consensus that a phase of major transgression took place during the early Toarcian (Figure 4) is reflected best by the development of the mean grain size, and hence, may be applied as an indication of relative sea-level change (Figure 20). Three different major trends can be derived from the mean grain size: (i) a stage of coarsening upward quartz size towards the Pliensbachian–Toarcian boundary, (ii) an interval of fining upward quartz size during the start of the Toarcian, and (iii) a renewed stage of coarsening upward quartz size towards the top of the succession. The implied sequence of regression-transgression-regression broadly matches the development regularly inferred for the late Pliensbachian–early Toarcian interval, although the indication that sea-level fall commenced halfway through the Mulgrave Shale Member (155.30 m) is significantly earlier than commonly thought (e.g., Haq et al. 1987). Additionally, it seems that Jet Rock deposition and the associated major TOC enrichment during the T-OAE is initiated roughly at the midpoint of the transgressive interval. If the implied sea-level curve is truly sinusoidal, this would coincide with the inflection point of the curve, and indicate the phase of highest rate of sea-level change sometimes associated with the formation of condensed sections. This observation correlates well with the interpretation of McArthur et al. (2000) that the Jet Rock is condensed in relation to adjacent strata. Thus, it appears that the

mean grain size of quartz is a good indicator of water depth and sequence stratigraphic cyclicity.

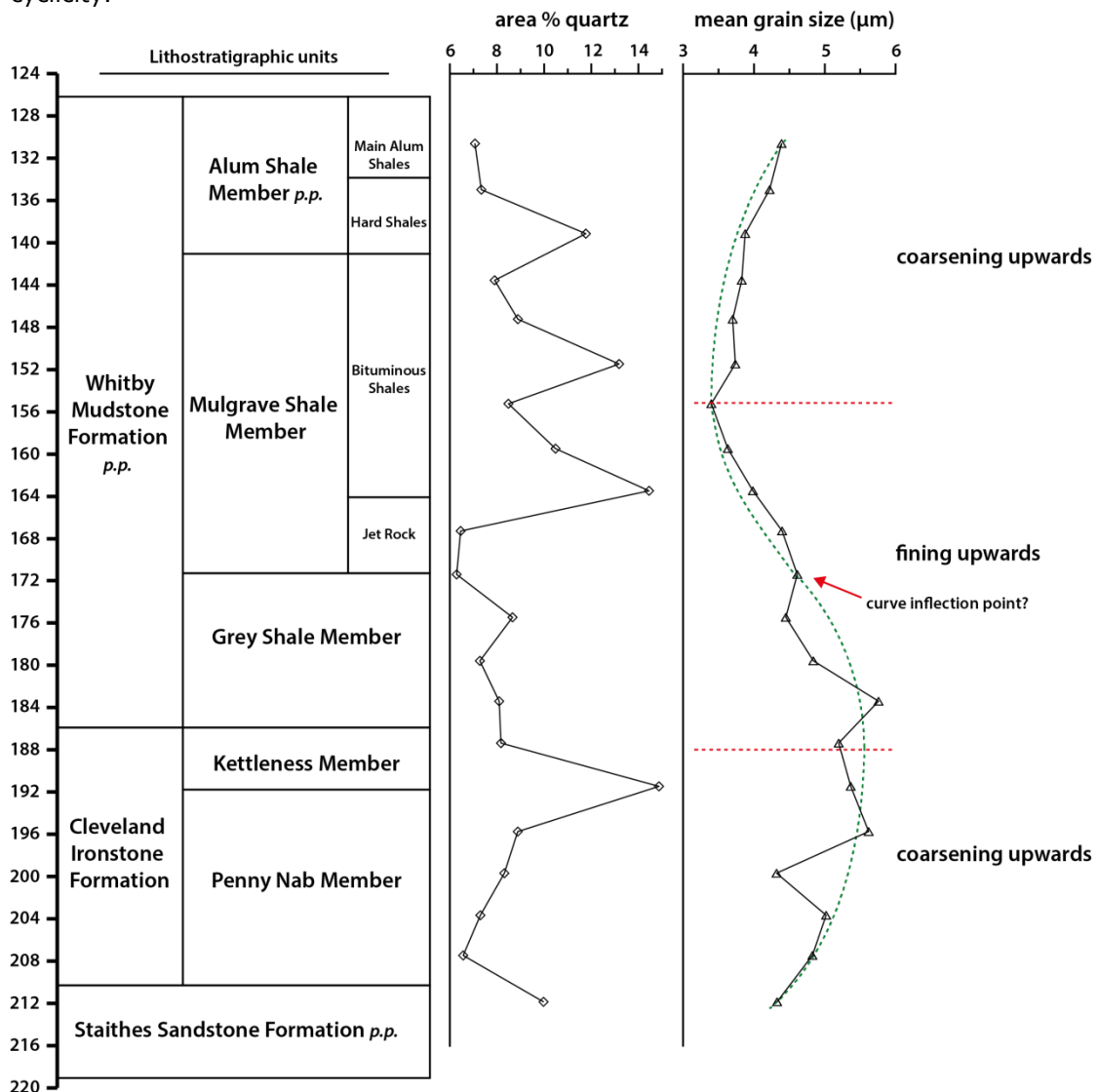


Figure 20) Interpretation of sequence stratigraphy based on mean grain size

The quartz content (area % quartz) fluctuates autonomously from the mean grain size (Figure 20). Therefore, it apparently reflects a different depositional control. Proposed controls, apart from sea-level change, include intensified weathering, local tectonic uplift, and sediment source switching (Macquaker et al. 1998; Williams et al. 2001). Of these proposed controls, local tectonic uplift is unquantifiable, while intensified weathering and a switch in sediment provenance seem unlikely due to the consistency of the clay mineral record and inferred stabilization of climate during the upper part of the succession (section 5.8). Since sediment grain size in shales typically does not reflect distance to shore (Trabucho-Alexandre 2015), shoreline proximity is a potential candidate to explain quartz content fluctuations. Circumstantial evidence for this claim is derived from the quartz grain size distributions. Although the absence of coarse-silt input at 139.25 m depth is inconsistent with the interpretation of increased proximity to the shoreline, and the amounts are minimal (Table 3), the appearance of grains in the coarse-silt size class at three out of four of the distinct peaks in quartz content (151.55, 163.52, and 191.41 m depth) indicates increased hydrodynamic conditions and a reduction of distance to the point of entry of sediments in the basin.

Supplementary evidence for the hypothesis of quartz content controlled by shoreline proximity is derived from the quantitative distribution of the clay minerals. The abundance

of kaolinite (of lack thereof), has previously been linked to transgression (section 5.8). Present day abundance of kaolinite in coastal regions of low latitudes (Griffin *et al.* 1968) are supposedly explained by clay mineral segregation in the marine environment due to physical sorting of sediment by size (Hallam 1975; Gibbs 1977). Subsequently, kaolinite/illite ratios have been used to infer shoreline proximity (Hallam 1975; Spears & Amin 1981; Hallam *et al.* 1991), with increased abundance of kaolinite marking shallowing and more nearshore conditions (Hallam *et al.* 1991), and increased mixed-layer clay marking more basal settings (Spears & Amin 1981). Contesting views of Deconinck (1993) and Hesselbo *et al.* (2009), claim that the ratio increases during transgression due to additional surficial erosion of kaolinite-rich pedogenic blankets. However, such soils have not been identified for the studied area, validating the use of the kaolinite abundance as an indication of shoreline proximity.

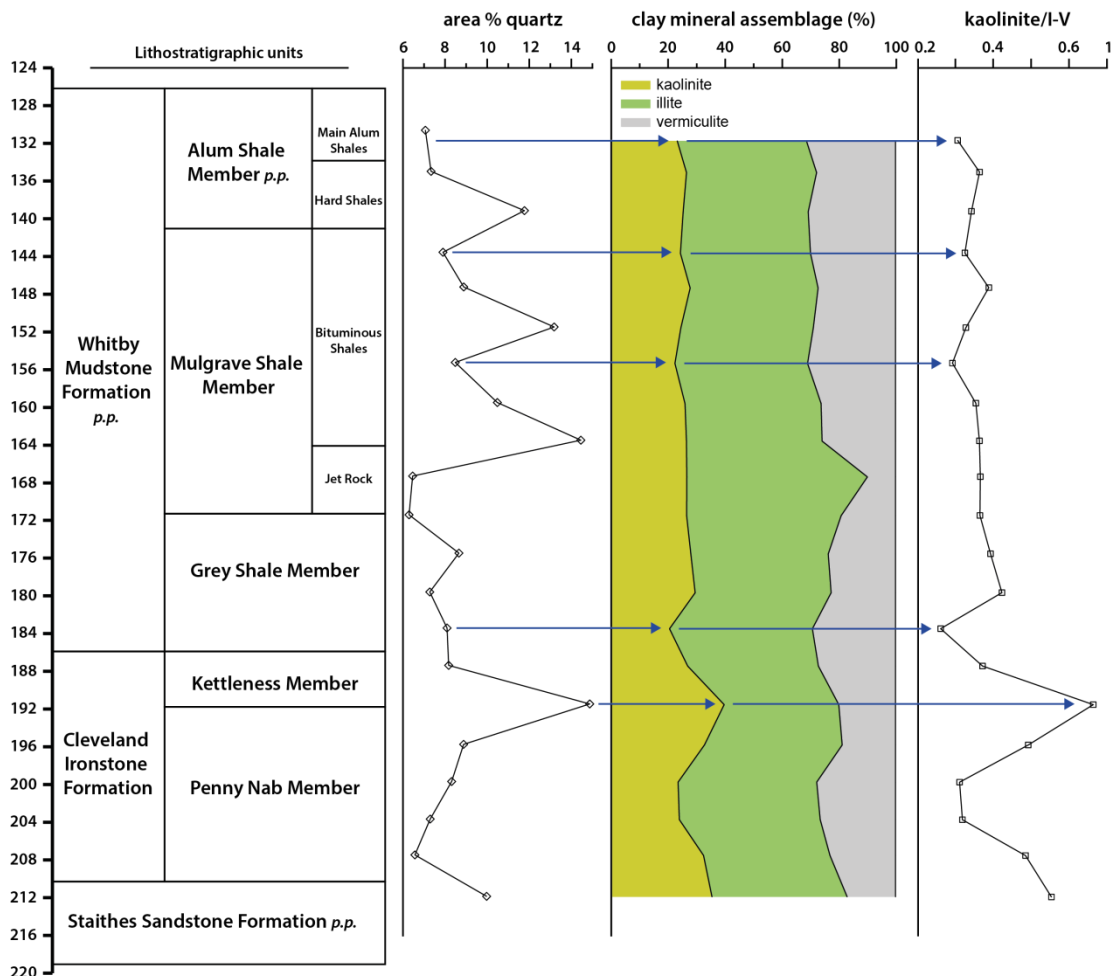


Figure 21) Quartz content versus clay mineral assemblage and ratio of kaolinite to irregularly interstratified illite-vermiculite.

Clay mineral assemblage must show only small variations, reflecting stability of source areas and paleoclimate, if to be applied in determination of eustatic fluctuations and sequence stratigraphy (Deconinck 1993). The assemblage of this study satisfies that condition for the upper part of the succession, corresponding to the period of most profound fluctuations in quartz content. Diminished and/or low quartz content appears to correlate well with reduced kaolinite abundance and low kaolinite to I/V ratios (Figure 21), suggesting that quartz content is indeed controlled by the proximity of the shoreline. However, during periods of increased quartz content, the correlation displays a mismatch apparently caused by a delayed response of the clay mineral assemblage. The reason for this lag is not clear, and, given the limited resolution of the dataset, cannot be well defined. Given that 'shoreline proximity' is essentially an analogue for short term sea-level

fluctuations subordinate to the higher order cycle determined from mean quartz grain size, the cause for the lag of clay mineralogy during periods of increased quartz input is related to either the forcing mechanism responsible for the sea-level fluctuations (i.e., climate and/or local tectonics) or the reworking of palimpsest sediments (*Atar 2015*) during sea-level fall.

An alternative explanation, also involving distance from source, might be that quartz content is related to major cyclic avulsions. The grain size distribution (Figure 9), sedimentological parameters (Figure 19), and climate (Figure 21), show no major response in relation to the periodic fluctuations in quartz content of the upper part of the succession. The implied suggestion is that there apparently is no significant change in sediment composition or depositional setting, indicating that quartz content is primarily a function of supply. Since there is no evidence for increased weathering rates that may explain the increased abundance of quartz, the resulting implication is that the source moved towards the area of deposition. Although this explanation is perhaps more improbable than the 'shoreline proximity concept' involving short term sea-level fluctuations, as of now, there is no definitive answer explaining the fluctuation of quartz content in the studied shales.

6. Conclusion

The results from the determination of quartz content, grain size distribution, and environmentally controlled statistical parameters, indicate that the late Pliensbachian–early Toarcian shale succession of the Cleveland Basin can be subdivided into two distinct depositional settings in terms of sedimentology. The lower part, extending from the late Pliensbachian into the early stages of the Toarcian, is inherently variable. The transition to the stable setting of the upper part took place before the onset of enhanced TOC deposition associated with the T-OAE, between 175.46–171.41 m depth, and probably simultaneous with the initiation of the carbon isotope excursion.

The results from clay mineralogy show that kaolinite and randomly interstratified illite-vermiculite dominate the clay mineral assemblage with a minor addition of chlorite in the lower part of the core between 175.46–211.75 m depth. The associated paleoclimate was temperate-warm with high levels of precipitation with podzols as the inferred dominant soil type. The results concur with the implied change in environment from quartz analysis and shows a similar subdivision between variable conditions in the lower part of the succession versus stable conditions in the upper part.

Evidence from grain size parameters and chlorite occurrence together indicate that the transition from variable to more stable conditions of both the depositional setting and climate probably initiated before the start of the T-OAE. The major perturbation that followed had a profound effect on both the clay mineralogy and depositional setting before stabilizing under slightly warmer and more consistent conditions.

The combined results indicate that facies derived from quartz content and clay mineralogy are primarily controlled by climate and have no principle relation to the geochemistry of the succession. Additionally, the lithostratigraphic subdivision of the late Pliensbachian–early Toarcian has no significance in terms of quartz content or grain size distribution and paleoclimate.

7. References

- Atar, E.F.L., 2015, Inorganic geochemistry and palaeoenvironments of the Early Jurassic Cleveland Basin: Durham theses, Durham University. Available at Durham E-Theses Online: <http://etheses.dur.ac.uk/10948/>
- Bailey, S.W., 1975, Chlorites: in Soil Components, Vol. 2, Inorganic Components, JE Gieseking, ed.
- Bailey, S.W., 1988, Chlorites; structures and crystal chemistry: Reviews in Mineralogy and Geochemistry, v. 19, no. 1, p. 347-403.
- Bailey, T., Rosenthal, Y., McArthur, J., Van De Schootbrugge, B., and Thirlwall, M., 2003, Paleooceanographic changes of the Late Pliensbachian–Early Toarcian interval: a possible link to the genesis of an Oceanic Anoxic Event: Earth and Planetary Science Letters, v. 212, no. 3, p. 307-320.
- Bain, D.C., Mellor, A., and Wilson, M., 1990, Nature and origin of an aluminous vermiculitic weathering product in acid soils from upland catchments in Scotland: Clay Minerals, v. 25, no. 4, p. 467-475.
- Barnard, P., 1973, Mesozoic floras: Special papers in Palaeontology, v. 12, p. 175-187.
- Barnard, P., and Cooper, B., 1983, A review of geochemical data related to the northwest European gas province: Geological Society, London, Special Publications, v. 12, no. 1, p. 19-33.
- Barnhisel, R.I., and Bertsch, P.M., 1989, Chlorites and hydroxy-interlayered vermiculite and smectite: Minerals in soil environments, no. mineralsinsoils, p. 729-788.
- Barshad, I., 1950, The effect of the interlayer cations on the expansion of the mica type of crystal lattice: Am.Mineral, v. 35, p. 225-238.
- Barshad, I., 1966, The effect of a variation in precipitation on the nature of clay mineral formation in soils from acid and basic igneous rocks, *in* Proceedings of the international clay conference, p. 167-173.
- Bergaya, F., and Lagaly, G., 2013, Handbook of clay science, Newnes 5.
- Berner, R.A., 1990, Atmospheric carbon dioxide levels over phanerozoic time: Science (New York, N.Y.), v. 249, no. 4975, p. 1382-1386.
- Biscaye, P., 1964, Distinction between kaolinite and chlorite in recent sediments by X-ray diffraction: American Mineralogist, v. 49, no. 9-1, p. 1281.
- Blatt, H., 1970, Determination of mean sediment thickness in the crust: a sedimentologic method: Geological Society of America Bulletin, v. 81, no. 1, p. 255-262.
- Blatt, H., and Jones, R.L., 1975, Proportions of exposed igneous, metamorphic, and sedimentary rocks: Geological Society of America Bulletin, v. 86, no. 8, p. 1085-1088.
- Blatt, H., and Schultz, D.J., 1976, Size distribution of quartz in mudrocks: Sedimentology, v. 23, no. 6, p. 857-866.
- Blatt, H., and Totten, M.W., 1981, Detrital quartz as an indicator of distance from shore in marine mudrocks: Journal of Sedimentary Research, v. 51, no. 4.
- Blatt, H., 1987, Oxygen Isotopes and the Origin of Quartz: PERSPECTIVE: Journal of sedimentary research, v. 57, no. 2.
- Boles, J.R., and Franks, S.G., 1979, Clay diagenesis in Wilcox sandstones of southwest Texas: implications of smectite diagenesis on sandstone cementation: Journal of Sedimentary Research, v. 49, no. 1.
- Bonifacio, E., Falsone, G., Simonov, G., Sokolova, T., and Tolpeshta, I., 2009, Pedogenic processes and clay transformations in bisequal soils of the Southern Taiga zone: Geoderma, v. 149, no. 1, p. 66-75.

- Bradshaw, M., Cope, J., Cripps, D., et al., 1992, Jurassic: Geological Society, London, Memoirs, v. 13, no. 1, p. 107-129.
- Camp, B.H., 1931, The mathematical part of elementary statistics: New York: D.C.Heath.
- Carter, E.S., Goričan, Š., Guex, J., et al., 2010, Global radiolarian zonation for the Pliensbachian, Toarcian and Aalenian: Palaeogeography, Palaeoclimatology, Palaeoecology, v. 297, no. 2, p. 401-419.
- Caruthers, A.H., Smith, P.L., and Gröcke, D.R., 2013, The Pliensbachian–Toarcian (Early Jurassic) extinction, a global multi-phased event: Palaeogeography, Palaeoclimatology, Palaeoecology, v. 386, p. 104-118.
- Carver, R., 1971, Procedures in sedimentology.
- Casey, R., 1993, Radiolaria: Fossil prokaryotes and protists, p. 249-284.
- Caswell, B.A., Coe, A.L., and Cohen, A.S., 2009, New range data for marine invertebrate species across the early Toarcian (Early Jurassic) mass extinction: Journal of the Geological Society, v. 166, no. 5, p. 859-872.
- Chamley, H., 1989, Clay sedimentology (p. 623).
- Chandler, M.A., Rind, D., and Ruedy, R., 1992, Pangaeian climate during the Early Jurassic: GCM simulations and the sedimentary record of paleoclimate: Geological Society of America Bulletin, v. 104, no. 5, p. 543-559.
- Chayes, F., 1950, On the bias of grain-size measurements made in thin section: The Journal of geology, v. 58, no. 2, p. 156-160.
- Chayes, F., 1951, On the Bias of Grain-Size Measurements Made in Thin Section: A Reply: The Journal of geology, v. 59, no. 3, p. 274-275.
- Chayes, F., 1954, The theory of thin-section analysis: The Journal of geology, p. 92-101.
- Churchman, G., 1980, Clay minerals formed from micas and chlorites in some New Zealand soils: Clay Minerals, v. 15, no. 1, p. 59-76.
- Cohen, A.S., Coe, A.L., Harding, S.M., and Schwark, L., 2004, Osmium isotope evidence for the regulation of atmospheric CO₂ by continental weathering: Geology, v. 32, no. 2, p. 157-160.
- Cohen, K., Finney, S., Gibbard, P., and Fan, J., 2013, The ICS international chronostratigraphic chart: Episodes, v. 36, no. 3, p. 199-204.
- Coward, M., Dewey, J., Hempton, M., and Holroyd, J., 2003, Tectonic evolution: The Millennium Atlas: Petroleum Geology of the Central and Northern North Sea. Geological Society, London, p. 17-33.
- Cox, B., 1990, A review of Jurassic chronostratigraphy and age indicators for the UK: Geological Society, London, Special Publications, v. 55, no. 1, p. 169-190.
- Curtis, C., 1990, Aspects of climatic influence on the clay mineralogy and geochemistry of soils, palaeosols and clastic sedimentary rocks: Journal of the Geological Society, v. 147, no. 2, p. 351-357.
- Deconinck, J., 1993, Clay mineralogy of the Late Tithonian-Berriasian deep-sea carbonates of the Vocontian Trough (SE France): relationships with sequence stratigraphy: Bulletin des Centres de Recherche Exploration–Production Elf Aquitaine, v. 17, p. 223-234.
- Deconinck, J., Hesselbo, S.P., Debuissier, N., Averbuch, O., Baudin, F., and Bessa, J., 2003, Environmental controls on clay mineralogy of an Early Jurassic mudrock (Blue Lias Formation, southern England): International Journal of Earth Sciences, v. 92, no. 2, p. 255-266.

- DeMaster, D.J., 2002, The accumulation and cycling of biogenic silica in the Southern Ocean: revisiting the marine silica budget: Deep Sea Research Part II: Topical Studies in Oceanography, v. 49, no. 16, p. 3155-3167.
- Dera, G., Pellenard, P., Neige, P., Deconinck, J., Pucéat, E., and Dommergues, J., 2009, Distribution of clay minerals in Early Jurassic Peritethyan seas: palaeoclimatic significance inferred from multiproxy comparisons: Palaeogeography, Palaeoclimatology, Palaeoecology, v. 271, no. 1, p. 39-51.
- Dera, G., Neige, P., Dommergues, J., Fara, E., Laffont, R., and Pellenard, P., 2010, High-resolution dynamics of Early Jurassic marine extinctions: the case of Pliensbachian–Toarcian ammonites (Cephalopoda): Journal of the Geological Society, v. 167, no. 1, p. 21-33.
- Dera, G., Neige, P., Dommergues, J., and Brayard, A., 2011, Ammonite paleobiogeography during the Pliensbachian–Toarcian crisis (Early Jurassic) reflecting paleoclimate, eustasy, and extinctions: Global and Planetary Change, v. 78, no. 3, p. 92-105.
- Dercourt, J., 2000, Atlas peri-Tethys palaeogeographical maps, CCGM/CGMW.
- Dixon, J.B., and Weed, S.B., 1989, Minerals in soil environments., Soil Science Society of America Inc.(SSSA).
- Doré, A., Lundin, E., Jensen, L., Birkeland, Ø., Eliassen, P., and Fichler, C., 1999, Principal tectonic events in the evolution of the northwest European Atlantic margin, *in* Geological society, london, petroleum geology conference series, Geological Society of London, p. 41-61.
- Drits, V., Sakharov, B., Lindgreen, H., and Salyn, A., 1997, Sequential structure transformation of illite-smectite-vermiculite during diagenesis of Upper Jurassic shales from the North Sea and Denmark: Clay Minerals, v. 32, no. 3, p. 351-371.
- Eberl, D., 1984, Clay mineral formation and transformation in rocks and soils [and discussion]: Philosophical Transactions of the Royal Society of London A: Mathematical, Physical and Engineering Sciences, v. 311, no. 1517, p. 241-257.
- Folk, R.L., 1966, A review of grain-size parameters: Sedimentology, v. 6, no. 2, p. 73-93.
- Frakes, L., 1979, Climates through geological time: Elsevier, Amsterdam.
- Francus, P., 1998, An image-analysis technique to measure grain-size variation in thin sections of soft clastic sediments: Sedimentary Geology, v. 121, no. 3, p. 289-298.
- Friedman, G.M., 1958, Determination of sieve-size distribution from thin-section data for sedimentary petrological studies: The Journal of geology, p. 394-416.
- Friedman, G.M., 1962, On sorting, sorting coefficients, and the lognormality of the grain-size distribution of sandstones: The Journal of geology, p. 737-753.
- Friedman, G.M., 1967, Dynamic processes and statistical parameters compared for size frequency distribution of beach and river sands: Journal of Sedimentary Research, v. 37, no. 2, p. 327-354.
- Friedman, G.M., and Sanders, J.E., 1978, Principles of sedimentology, Wiley.
- Friedman, G.M., 1979, Address of the retiring President of the International Association of Sedimentologists: Differences in size distributions of populations of particles among sands of various origins: Sedimentology, v. 26, no. 1, p. 3-32.
- Friedman, G.M., 1996, Thin section grain size analysis revisited: Sedimentology, v. 43, no. 1, p. 189-189.
- Gatliff, R., 1994, The geology of the central North Sea, HM Stationery Office 5.
- Ghiold, J., 1991, The sponges that spanned Europe: New Scientist, v. 129, no. 1754, p. 58-62.

- Gibbs, R.J., 1977, Clay mineral segregation in the marine environment: *Journal of Sedimentary Research*, v. 47, no. 1.
- Goldstein, J., Newbury, D., Joy, D., Lyman, C., Echlin, P., Lifkshin, E., Sawyer, L., Michael, J., 2007. *Scanning Electron Microscopy and X-ray Microanalysis*, 3rd edition. Springer Scienc+Business Media, LLC978-0-306-47292-3.
- Goričan, Š., Carter, E.S., Guex, J., et al., 2013, Evolutionary patterns and palaeobiogeography of Pliensbachian and Toarcian (Early Jurassic) radiolaria: *Palaeogeography, Palaeoclimatology, Palaeoecology*, v. 386, p. 620-636.
- Graciansky, P.C., Jacquin, T., and Hesselbo, S.P., 1998, The Ligurian cycle: an overview of Lower Jurassic 2nd-order transgressive/regressive facies cycles in western Europe.
- Gradstein, F.M., Ogg, G., and Schmitz, M., 2012, *The Geologic Time Scale 2012 2-Volume Set*, elsevier.
- Greenman, N.N., 1951a, The mechanical analysis of sediments from thin-section data: *The Journal of geology*, p. 447-462.
- Greenman, N.N., 1951b, On the bias of grain-size measurements made in thin-section: A discussion: *The Journal of geology*, v. 59, no. 3, p. 268-274.
- Griffin, J.J., Windom, H., and Goldberg, E.D., 1968, The distribution of clay minerals in the world ocean, *in Deep Sea Research and Oceanographic Abstracts*, Elsevier, p. 433-459.
- Gröcke, D., Hori, R., Trabucho-Alexandre, J., Kemp, D., and Schwark, L., 2011, An open ocean record of the Toarcian oceanic anoxic event: *Solid Earth*, v. 2, no. 2, p. 245.
- Hallam, A., 1967, An environmental study of the upper Domerian and lower Toarcian in Great Britain: *Philosophical Transactions of the Royal Society of London B: Biological Sciences*, v. 252, no. 778, p. 393-445.
- Hallam, A., and Sellwood, B., 1968, Origin of fuller's earth in the Mesozoic of southern England: *Nature*, v. 220, p. 1193-1195.
- Hallam, A., 1975, *Jurassic environments*, Cambridge University Press.
- Hallam, A., 1978, Eustatic cycles in the Jurassic: *Palaeogeography, Palaeoclimatology, Palaeoecology*, v. 23, p. 1-32.
- Hallam, A., 1981a, A revised sea-level curve for the early Jurassic: *Journal of the Geological Society*, v. 138, no. 6, p. 735-743.
- Hallam, A., 1981b, Facies interpretation and the stratigraphic record.
- Hallam, A., 1985, A review of Mesozoic climates: *Journal of the Geological Society*, v. 142, no. 3, p. 433-445.
- Hallam, A., 1986, The Pliensbachian and Tithonian extinction events: *Nature*, v. 319, no. 6056, p. 765-768.
- Hallam, A., 1987, Radiations and extinctions in relation to environmental change in the marine Lower Jurassic of northwest Europe: *Paleobiology*, v. 13, no. 02, p. 152-168.
- Hallam, A., Grose, J., and Ruffell, A., 1991, Palaeoclimatic significance of changes in clay mineralogy across the Jurassic-Cretaceous boundary in England and France: *Palaeogeography, Palaeoclimatology, Palaeoecology*, v. 81, no. 3-4, p. 173-187.
- Hallam, A., 1997, Estimates of the amount and rate of sea-level change across the Rhaetian—Hettangian and Pliensbachian—Toarcian boundaries (latest Triassic to early Jurassic): *Journal of the Geological Society*, v. 154, no. 5, p. 773-779.
- Hallam, A., and Wignall, P.B., 1997, *Mass extinctions and their aftermath*, Oxford University Press, UK.

- Haq, B.U., Hardenbol, J., and Vail, P.R., 1987, Chronology of fluctuating sea levels since the triassic: *Science* (New York, N.Y.), v. 235, no. 4793, p. 1156-1167.
- Harries, P.J., and Little, C.T., 1999, The early Toarcian (Early Jurassic) and the Cenomanian–Turonian (Late Cretaceous) mass extinctions: similarities and contrasts: *Palaeogeography, Palaeoclimatology, Palaeoecology*, v. 154, no. 1, p. 39-66.
- Harris, W., and White, G.N., 2008, X-ray diffraction techniques for soil mineral identification: *Methods of soil analysis, part*, p. 81-116.
- Hartman, W.D., Wendt, J.W., and Wiedenmayer, F., 1980, Living and fossil sponges: notes for a short course, *Comparative Sedimentology Laboratory, Division of Marine Geology and Geophysics, Rosentiel School of Marine & Atmospheric Science, University of Miami* 8.
- Hemingway, J., 1974, Jurassic, *in* The geology and mineral resources of Yorkshire, *Yorkshire Geol. Soc.*, p. 161-223
- Hemingway, J., and Riddler, G., 1982, Basin inversion in north Yorkshire: *Institution of Mining and Metallurgy Transactions*, v. 91.
- Hesselbo, S.P., and Jenkyns, H.C., 1998, British lower Jurassic sequence stratigraphy.
- Hesselbo, S.P., Gröcke, D.R., Jenkyns, H.C., Bjerrum, C.J., Farrimond, P., Bell, H.S.M., and Green, O.R., 2000, Massive dissociation of gas hydrate during a Jurassic oceanic anoxic event: *Nature*, v. 406, no. 6794, p. 392-395.
- Hesselbo, S.P., Deconinck, J., Huggett, J.M., and Morgans-Bell, H.S., 2009, Late Jurassic palaeoclimatic change from clay mineralogy and gamma-ray spectrometry of the Kimmeridge Clay, Dorset, UK: *Journal of the Geological Society*, v. 166, no. 6, p. 1123-1133.
- Hillier, S., 2003, Quantitative analysis of clay and other minerals in sandstones by X-ray powder diffraction (XRPD): *Clay Mineral Cements in Sandstones: Special Publication*, v. 34, p. 213-251.
- Holliday, D., 1999, Palaeotemperatures, thermal modelling and depth of burial studies in northern and eastern England, *in* Proceedings of the Yorkshire Geological and Polytechnic Society, *Geological Society of London*, p. 337-352.
- Hong, H., Churchman, G.J., Yin, K., Li, R., and Li, Z., 2014, Randomly interstratified illite-vermiculite from weathering of illite in red earth sediments in Xuancheng, southeastern China: *Geoderma*, v. 214, p. 42-49.
- Houben, M., Desbois, G., and Urai, J., 2013, Pore morphology and distribution in the shaly facies of Opalinus Clay (Mont Terri, Switzerland): Insights from representative 2D BIB–SEM investigations on mm to nm scale: *Applied Clay Science*, v. 71, p. 82-97.
- Houben, M., Barnhoorn, A., Lie-A-Fat, J., Ravestein, T., Peach, C., and Drury, M., 2016, Microstructural characteristics of the Whitby Mudstone Formation (UK): *Marine and Petroleum Geology*, v. 70, p. 185-200.
- Howard, A., 1985, Lithostratigraphy of the Staithes sandstone and Cleveland Ironstone formations (Lower Jurassic) of north-east Yorkshire, *in* Proceedings of the Yorkshire Geological and Polytechnic Society, *Geological Society of London*, p. 261-275.
- Howarth, M.K., 1955, Domesian of the Yorkshire coast, *in* Proceedings of the Yorkshire Geological and Polytechnic Society, *Geological Society of London*, p. 147-175.
- Howarth, M.K., 1962, The jet rock series and the alum shale series of the Yorkshire coast, *in* Proceedings of the Yorkshire Geological and Polytechnic Society, *Geological Society of London*, p. 381-422.
- Hower, J., Eslinger, E.V., Hower, M.E., and Perry, E.A., 1976, Mechanism of burial metamorphism of argillaceous sediment: 1. Mineralogical and chemical evidence: *Geological Society of America Bulletin*, v. 87, no. 5, p. 725-737.

- Hughes, R., Moore, D., and Glass, H., 1994, Qualitative and quantitative analysis of clay minerals in soils: Quantitative methods in soil mineralogy, no. quantitativemet, p. 330-359.
- Jackson, M., Hseung, Y., Corey, R., Evans, E., and Vanden Heuvel, R., 1952, Weathering sequence of clay-size minerals in soils and sediments: II. Chemical weathering of layer silicates, *in* Soil Sci. Soc. Am. Proc, p. 3-6.
- Jacquin, T., and Graciansky, P.C., 1998, Major transgressive/regressive cycles: the stratigraphic signature of European basin development.
- Jeans, C., 2006, Clay mineralogy of the Jurassic strata of the British Isles: Clay Minerals, v. 41, no. 1, p. 187-307.
- Jenkyns, H., 1988, The early Toarcian (Jurassic) anoxic event-stratigraphic, sedimentary, and geochemical evidence: American Journal of Science, v. 288, no. 2.
- Johnson, M., 1994, Thin section grain size analysis revisited: Sedimentology, v. 41, no. 5, p. 985-999.
- Johnson, M., 1996, Thin section grain size analysis revisited-Reply: Sedimentology, v. 43, no. 1, p. 190-191.
- Kellerhals, R., Shaw, J., and Arora, V.K., 1975, On grain size from thin sections: The Journal of geology, p. 79-96.
- Kemp, D.B., Coe, A.L., Cohen, A.S., and Schwark, L., 2005a, Astronomical pacing of methane release in the Early Jurassic period: Nature, v. 437, no. 7057, p. 396-399.
- Kemp, S., Merriman, R., and Bouch, J., 2005b, Clay mineral reaction progress—the maturity and burial history of the Lias Group of England and Wales: Clay Minerals, v. 40, no. 1, p. 43-62.
- Kennedy, S., and Mazzullo, J., 1991, Image analysis method of grain size measurement: Principles, methods, and application of particle size analysis, p. 76-87.
- Knox, R., Howard, A., Powell, J., and Van Buchem, F., 1991, Lower and Middle Jurassic sediments of the Cleveland Basin, NE England: shallow marine and paralic facies seen in their sequence stratigraphic context. Field Guide, 5. Compiled for the 13th International Sedimentological Congress, Nottingham, UK. 1990: British Sedimentological Research Group.
- Kong, M., Bhattacharya, R.N., James, C., and Basu, A., 2005, A statistical approach to estimate the 3D size distribution of spheres from 2D size distributions: Geological Society of America Bulletin, v. 117, no. 1-2, p. 244-249.
- Korte, C., and Hesselbo, S.P., 2011, Shallow marine carbon and oxygen isotope and elemental records indicate icehouse-greenhouse cycles during the Early Jurassic: Paleoclimatology, v. 26, no. 4.
- Korte, C., Hesselbo, S.P., Ullmann, C.V., Dietl, G., Ruhl, M., Schweigert, G., and Thibault, N., 2015, Jurassic climate mode governed by ocean gateway: Nature communications, v. 6.
- Krinsley, D., Pye, K., and Kearsley, A., 1983, Application of backscattered electron microscopy in shale petrology: Geological Magazine, v. 120, no. 02, p. 109-114.
- Krinsley, D., Nagy, B., Dypvik, H., and Rigali, M., 1993, Microtextures in mudrocks as revealed by backscattered electron imaging: Precambrian Research, v. 61, no. 3-4, p. 191-207.
- Krumbein, W., 1935, Thin-section mechanical analysis of indurated sediments: The Journal of geology, p. 482-496.
- Krumbein, W.C., 1936, Application of logarithmic moments to size frequency distributions of sediments: Journal of Sedimentary Research, v. 6, no. 1.

- Krumbein, W., 1950, Grain-Size Measurements Made in Thin Section: Comments: The Journal of geology, v. 58, no. 2, p. 160-160.
- Lin, C., Hseu, Z., and Chen, Z., 2002, Clay mineralogy of Spodosols with high clay contents in the subalpine forests of Taiwan: Clays and Clay Minerals, v. 50, no. 6, p. 726-735.
- Little, C.T., and Benton, M.J., 1995, Early Jurassic mass extinction: a global long-term event: Geology, v. 23, no. 6, p. 495-498.
- Little, C.T., 1996, The Pliensbachian-Toarcian (Lower Jurassic) extinction event: Geological Society of America Special Papers, v. 307, p. 505-512.
- Liu, J., and Chen, Z., 2004, Soil characteristics and clay mineralogy of two subalpine forest spodosols with clay accumulation in Taiwan: Soil Science, v. 169, no. 1, p. 66-80.
- Lott, G., Wong, T., Dusar, M., Andsbjerg, J., Mönnig, E., Feldman-Olszewska, A., and Verreussel, R., 2010, Jurassic: Petroleum Geological Atlas of the Southern Permian Basin Area. EAGE Publications (Houten), v. 175, p. 193.
- Macquaker, J., and Taylor, K., 1996, A sequence-stratigraphic interpretation of a mudstone-dominated succession: the Lower Jurassic Cleveland Ironstone Formation, UK: Journal of the Geological Society, v. 153, no. 5, p. 759-770.
- Macquaker, J., Gawthorpe, R., Taylor, K., and Oates, M., 1998, Heterogeneity, stacking patterns and sequence stratigraphic interpretation in distal mudstone successions: examples from the Kimmeridge Clay Formation, UK.
- McArthur, J., Donovan, D., Thirlwall, M., Fouke, B., and Matthey, D., 2000, Strontium isotope profile of the early Toarcian (Jurassic) oceanic anoxic event, the duration of ammonite biozones, and belemnite palaeotemperatures: Earth and Planetary Science Letters, v. 179, no. 2, p. 269-285.
- McCartney, K., Wise Jr, S.W., Harwood, D.M., and Gersonde, R., 1986, Enigmatic lower Albian silicoflagellates from ODP site 693 progenitors of the order silicoflagellata? *in* Proceedings of the Ocean Drilling Program: Scientific results, The Program, p. 427.
- McElwain, J.C., Wade-Murphy, J., and Hesselbo, S.P., 2005, Changes in carbon dioxide during an oceanic anoxic event linked to intrusion into Gondwana coals: Nature, v. 435, no. 7041, p. 479-482.
- McManus, D.A., 1963, A criticism of certain usage of the phi-notation: Journal of Sedimentary Research, v. 33, no. 3.
- McManus, D.A., 1991, Suggestions for authors whose manuscripts include quantitative clay mineral analysis by X-ray diffraction: Marine Geology, v. 98, no. 1, p. 1-5.
- McManus, J., 1988, Grain size determination and interpretation: Techniques in sedimentology, v. 408, p. 63-85.
- Méring, J., 1949, L'interférence des rayons X dans les systèmes à stratification désordonnée: Acta Crystallographica, v. 2, no. 6, p. 371-377.
- Merriman, R., and Frey, M., 1999, Patterns of very lowgrade metamorphism in metapelitic rocks. Pp. 61-107 in: Low-grade Metamorphism (M. Frey & D. Robinson, editors).
- Mielenz, R.C., Schieltz, N.C., and King, M.E., 1955, Effect of exchangeable cation on X-ray diffraction patterns and thermal behavior of a montmorillonite clay: Clays Clay Miner, v. 3, p. 146-173.
- Milliken, K.L., 1994, Cathodoluminescent Textures and the Origin of Quarts Silt in Oligocene Mudrocks, South Texas: Journal of Sedimentary Research, v. 64, no. 3.









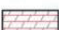






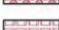



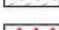
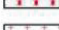
- Milliken, K.L., Ergene, S.M., and Ozkan, A., 2016, Quartz types, authigenic and detrital, in the upper cretaceous eagle ford formation, South Texas, USA: *Sedimentary Geology*, v. 339, p. 273-288.
- Millot, G., 1970, *Geology of Clay: Weathering, Sedimentology, Geochemistry*, Springer-Verlag.
- Millot, G., and Camez, T., 1963, Genesis of vermiculite and mixed layered vermiculite in the evolution of soils in France, 90–95: *Clays and Clay Minerals Earth Sciences Monograph*, v. 12.
- Mock, S., and Palmer, T., 1991, Preservation of siliceous sponges in the Jurassic of southern England and northern France: *Journal of the Geological Society*, v. 148, no. 4, p. 681-689.
- Moore, D.M., and Reynolds, R.C., 1989, *X-ray Diffraction and the Identification and Analysis of Clay Minerals*, Oxford university press Oxford 378.
- O'Brien, N.R., 1990, Significance of lamination in Toarcian (Lower Jurassic) shales from Yorkshire, Great Britain: *Sedimentary Geology*, v. 67, no. 1-2, p. 25-34.
- O'Brien, N.R., 1996, *Shale lamination and sedimentary processes: Geological Society, London, Special Publications*, v. 116, no. 1, p. 23-36.
- Pálffy, J., Smith, P., and Mortensen, J., 1999, A revised numeric time scale for the Jurassic, *in Retrospective Collection*, Trans Tech Publ, p. 181-182.
- Philippe, H., Sörhannus, U., Baroin, A., Perasso, R., Gasse, F., and Adoutte, A., 1994, Comparison of molecular and paleontological data in diatoms suggests a major gap in the fossil record: *Journal of Evolutionary Biology*, v. 7, no. 2, p. 247-265.
- Pike, J., and Kemp, A.E., 1996, Silt aggregates in laminated marine sediment produced by agglutinated foraminifera: *Journal of Sedimentary Research*, v. 66, no. 3.
- Powell, J., 1984, Lithostratigraphical nomenclature of the Lias Group in the Yorkshire Basin, *in Proceedings of the Yorkshire Geological and Polytechnic Society, Geological Society of London*, p. 51-57.
- Powell, J., 2010, Jurassic sedimentation in the Cleveland Basin: a review: *Proceedings of the Yorkshire Geological Society*, v. 58, no. 1, p. 21-72.
- Pye, K., and Krinsley, D.H., 1984, Petrographic examination of sedimentary rocks in the SEM using backscattered electron detectors: *Journal of Sedimentary Research*, v. 54, no. 3.
- Pye, K., and Krinsley, D.H., 1986, Microfabric, mineralogy and early diagenetic history of the Whitby Mudstone Formation (Toarcian), Cleveland Basin, UK: *Geological Magazine*, v. 123, no. 03, p. 191-203.
- Rawson, P., and Wright, J., 1995, *Jurassic of the Cleveland Basin, North Yorkshire: Field geology of the British Jurassic: Geological Society of London*, p. 173-208.
- Reynolds, R., 1980, Interstratified clay minerals: Crystal structures of clay minerals and their X-ray identification, p. 249-303.
- Reynolds, R., 1988, Mixed layer chlorite minerals: *Reviews in Mineralogy and Geochemistry*, v. 19, no. 1, p. 601-629.
- Rich, C., 1958, Muscovite weathering in a soil developed in the Virginia Piedmont: *Clays Clay Miner*, v. 5, p. 203-212.
- Rigby, J., 1971, Sponges and reefs and related facies through time, *in Reef Organisms Through Time. North American Paleontological Convention Proceedings*, p. 1374-1388.
- Rothpletz, A., 1896, Ueber die Flysch-Fucoiden und einige andere fossile Algen, sowie über liasische, Diatomeen führende Hornschwämme.: *Zeitschrift der Deutschen Geologischen Gesellschaft*, p. 854-914.

- Sakharov, B., and Lanson, B., 2013, X-ray Identification of Mixed-Layer Structures: Modelling of Diffraction Effects-Chapter 2.3.
- Sawhney, B.L., 1989, Interstratification in layer silicates: Minerals in soil environments, no. mineralsinsoile, p. 789-828.
- Schäfer, A., and Teyssen, T., 1987, Size, shape and orientation of grains in sands and sandstones—image analysis applied to rock thin-sections: *Sedimentary Geology*, v. 52, no. 3-4, p. 251-271.
- Schieber, J., 1996, Early diagenetic silica deposition in algal cysts and spores: a source of sand in black shales?: *Journal of Sedimentary Research*, v. 66, no. 1.
- Schieber, J., Krinsley, D., and Riciputi, L., 2000, Diagenetic origin of quartz silt in mudstones and implications for silica cycling: *Nature*, v. 406, no. 6799, p. 981-985.
- Schieber, J., and Zimmerle, W., 1998, Petrography of shales: a survey of techniques: *Shales and Mudstones.: Petrography, Petrophysics, Geochemistry, and Economic Geology*, v. 2, p. 3-12.
- Schubert, J.K., Kidder, D.L., and Erwin, D.H., 1997, Silica-replaced fossils through the Phanerozoic: *Geology*, v. 25, no. 11, p. 1031-1034.
- Sellwood, B.W., 1972, Regional environmental changes across a Lower Jurassic stage-boundary in Britain: *Palaeontology*, v. 15, no. 1, p. 125.
- Sellwood, B., 1986, Shallow-marine carbonate environments. *in Sedimentary environments and facies*, Blackwell Oxford, p.283-342.
- Sellwood, B., and Sladen, C., 1981, Mesozoic and Tertiary argillaceous units: distribution and composition: *Quarterly Journal of Engineering Geology and Hydrogeology*, v. 14, no. 4, p. 263-275.
- Shaw, H., 1981, Mineralogy and petrology of the argillaceous sedimentary rocks of the UK.: *Quarterly Journal of Engineering Geology and Hydrogeology*, v. 14, no. 4, p. 277-290.
- Simms, M.J., Chidlaw, N., Morton, N., and Page, K.N., 2004, British Lower Jurassic Stratigraphy, Geological Conservation Review Series, No. 30, Joint Nature Conservation Committee, Peterborough, 458 pp 30.
- Sims, P.A., Mann, D.G., and Medlin, L.K., 2006, Evolution of the diatoms: insights from fossil, biological and molecular data: *Phycologia*, v. 45, no. 4, p. 361-402.
- Singer, A., 1980, The paleoclimatic interpretation of clay minerals in soils and weathering profiles: *Earth-Science Reviews*, v. 15, no. 4, p. 303-326.
- Singer, A., 1984, The paleoclimatic interpretation of clay minerals in sediments—a review: *Earth-Science Reviews*, v. 21, no. 4, p. 251-293.
- Spears, D., and Amin, M., 1981, A mineralogical and geochemical study of turbidite sandstones and interbedded shales, Mam Tor, Derbyshire, UK: *Clay Minerals*, v. 16, no. 4, p. 333-345.
- Środoń, J., 1999, Nature of mixed-layer clays and mechanisms of their formation and alteration: *Annual Review of Earth and Planetary Sciences*, v. 27, no. 1, p. 19-53.
- Środoń, J., 2006, Identification and Quantitative Analysis of Clay Minerals: *Developments in Clay Science*, v. 1, p. 765-787.
- Thierry, J., and Barrier, E., 2000, Middle Toarcian (map 8): Atlas Peri-Tethys, Paleogeographical maps, CCM/CGMW, Paris.
- Thiry, M., 2000, Palaeoclimatic interpretation of clay minerals in marine deposits: an outlook from the continental origin: *Earth-Science Reviews*, v. 49, no. 1, p. 201-221.

- Thorez, J., 1975, Phyllosilicates and clay minerals: a laboratory handbook for their x-ray diffraction analysis.
- Tovey, N., and Krinsley, D., 1991, Mineralogical mapping of scanning electron micrographs: *Sedimentary Geology*, v. 75, no. 1, p. 109-123.
- Trabucho-Alexandre, J., 2015, Organic Matter-Rich Shale Depositional Environments: Fundamentals of Gas Shale Reservoirs, p. 21-45.
- Udden, J.A., 1914, Mechanical composition of clastic sediments: *Geological Society of America Bulletin*, v. 25, no. 1, p. 655-744.
- Underhill, J.T., and Partington, M., 1993, Jurassic thermal doming and deflation in the North Sea: implications of the sequence stratigraphic evidence, *in Geological Society, London, Petroleum Geology Conference series, Geological Society of London*, p. 337-345.
- van de Kamp, Peter C, 2008, Smectite-illite-muscovite transformations, quartz dissolution, and silica release in shales: *Clays and Clay Minerals*, v. 56, no. 1, p. 66-81.
- van de Schootbrugge, B., McArthur, J.M., Bailey, T., Rosenthal, Y., Wright, J., and Miller, K., 2005, Toarcian oceanic anoxic event: an assessment of global causes using belemnite C isotope records: *Paleoceanography*, v. 20, no. 3.
- Walker, G., 1975, Vermiculites. *in Soil components*, Springer, p.155-189.
- Weaver, C.E., 1956, The distribution and identification of mixed-layer clay in sedimentary rocks: *Am.Mineral*, v. 141, p. 202-221.
- Weaver, C.E., 1980, Fine-grained rocks: shales or physilites: *Sedimentary Geology*, v. 27, no. 4, p. 301-313.
- Weaver, C.E., 1989, *Clays, muds, and shales*, Elsevier 44.
- Wentworth, C.K., 1922, A scale of grade and class terms for clastic sediments: *The Journal of geology*, v. 30, no. 5, p. 377-392.
- Wignall, P.B., Newton, R.J., and Little, C.T., 2005, The timing of paleoenvironmental change and cause-and-effect relationships during the Early Jurassic mass extinction in Europe: *American Journal of Science*, v. 305, no. 10, p. 1014-1032.
- Williams, C.J., Hesselbo, S.P., Jenkyns, H.C., and Morgans-Bell, H.S., 2001, Quartz silt in mudrocks as a key to sequence stratigraphy (Kimmeridge Clay Formation, Late Jurassic, Wessex Basin, UK): *Terra Nova*, v. 13, no. 6, p. 449-455.
- Wilson, M., 1999, The origin and formation of clay minerals in soils: past, present and future perspectives: *Clay Minerals*, v. 34, no. 1, p. 7-25.
- Ziegler, P., 1990, Pangaea break-up: Jurassic–Early Cretaceous opening of central North Atlantic and western Tethys: *Shell International Petroleum, Maatschappij., ed., Geological Atlas of Western and Central Europe*, p. 91-122.
- Ziegler, P., 1992, North Sea rift system: *Tectonophysics*, v. 208, no. 1, p. 55-75.

Appendix A - Key to Figure 1






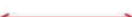


LITHOLOGICAL SYMBOLS

-  Shale, clay
-  Sandstone, sand (silt)
-  Conglomerate
-  Breccia
-  Marl
-  Limestone
-  Nodular limestone
-  Chalk
-  Dolomite
-  Anoxic, organic shale and clay
-  Banded/laminated chert, silicified limestone (incl. menilites)
-  Graded beds (incl. turbidite)
S : silicoclastic
V : volcanoclastic
C : carbonatic
-  Oolites
-  Diatomaceous deposits
-  Radiolaritic deposits
-  Lignite, coal (peat)
-  Sulphates
-  Halite
-  Intrusives
-  Extrusives/volcanics (volcano)
-  Pyroclastics




Examples of Mixed Lithologies

-  Sand(stone) and Conglomerate
-  Oolitic Limestone
-  Sulphates and Halite

TECTONIC SYMBOLS

-  Fault : unspecified, ascertained
-  Fault : questionable
-  Normal fault
-  Strike-slip fault
-  Thrust fault/front reverse fault
-  Anticlinal fold axis
-  Synclinal fold axis
-  Oceanic subduction








REGIONAL DEPOCENTRAL TRENDS

-  Active extension
-  "Post-rift" passive thermal subsidence
-  Active compression

PALAEOSTRESS SYMBOLS

-  Reverse fault regime
-  Normal fault regime
-  Strike-slip fault regime

SPECIAL SYMBOLS

-  Marine incursion
-  Coastal sediment influx
-  Intra-basinal sediment transport
-  Bioherm, reef
-  Deltaic / submarine fan
-  Volcano
-  Mountain range

Appendix B - SEM images

Different images used for determination of silt content and grain size distributions per sample. Header for each set of images includes: sample number, core depth, and the associated lithostratigraphy.

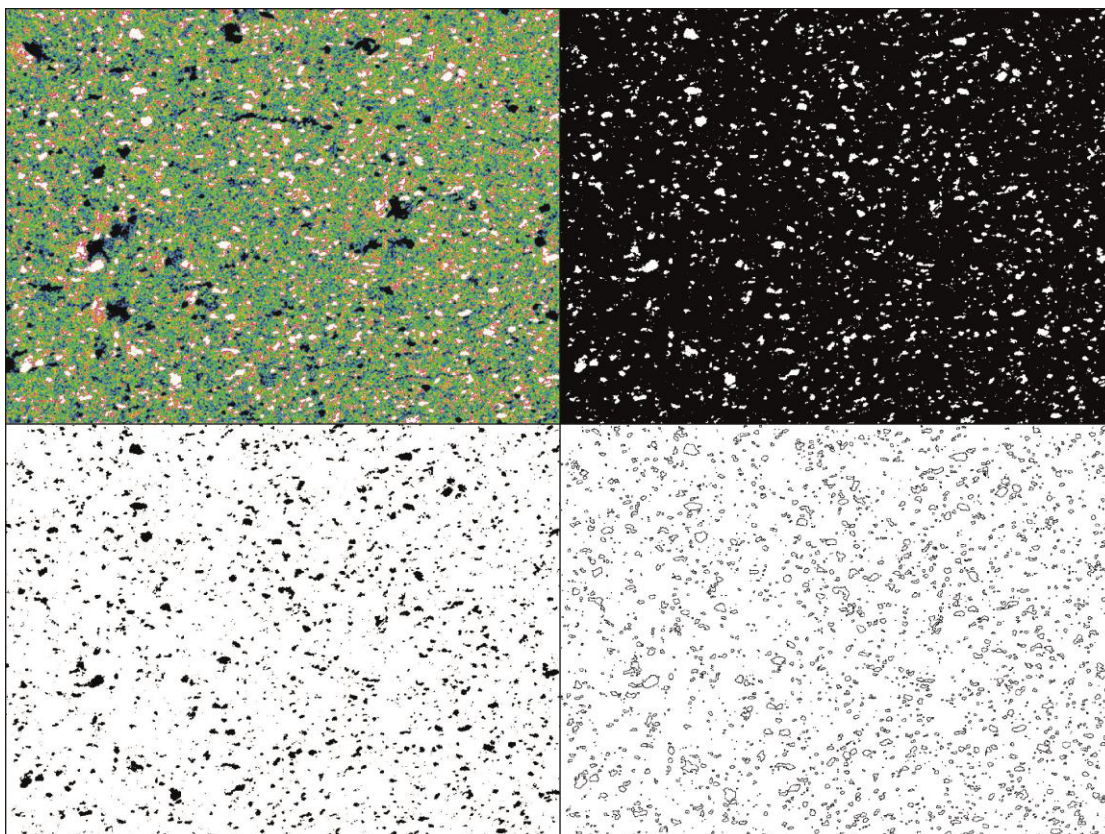
All sets comply to the following set-up:

- A Raw image
- B Highest silicon occurrences isolated from background by thresholding
- C Unedited image used for determination of total % area occupied by quartz-silt. Includes grains in contact with edge of image
- D Outlines of all particles used for grain size analysis. Image is edited to separate clusters of grains and grains in contact with image edge are excluded

A	B
C	D

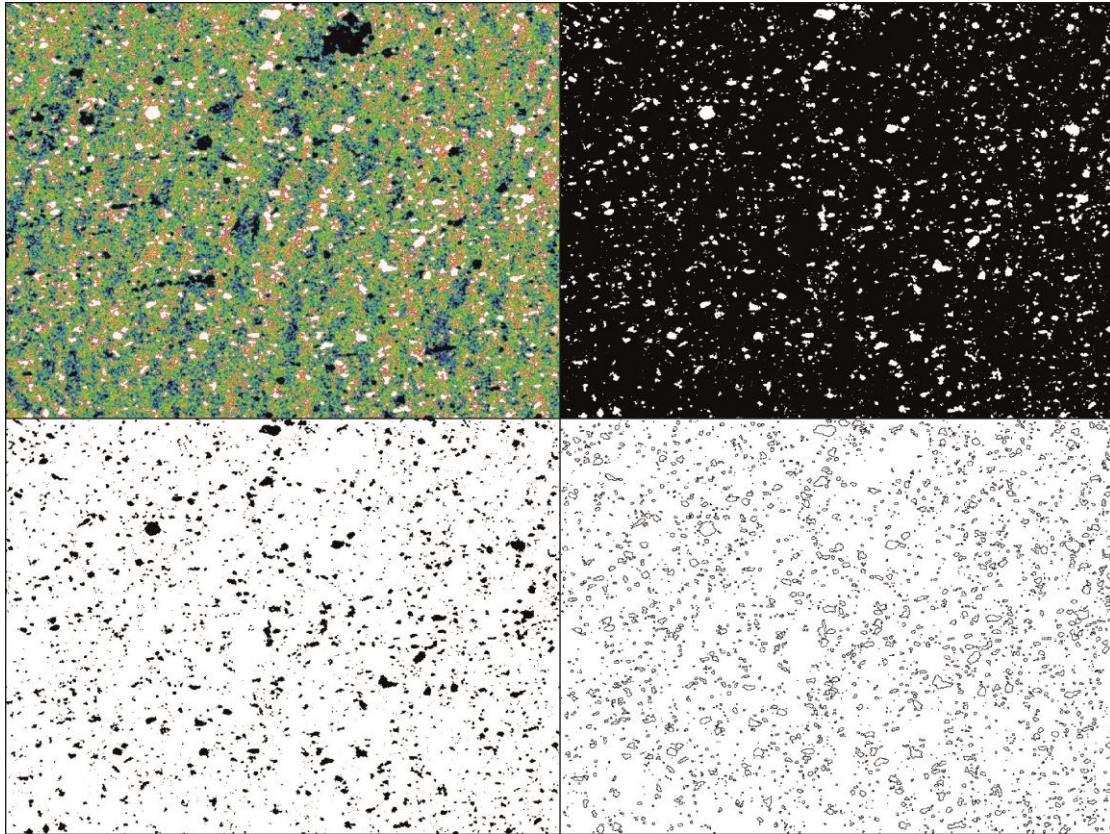
Notes: WMF = Whitby Mudstone Formation

DN01 depth: 130,75 m WMF – Alum Shale Member – Main Alum Shales



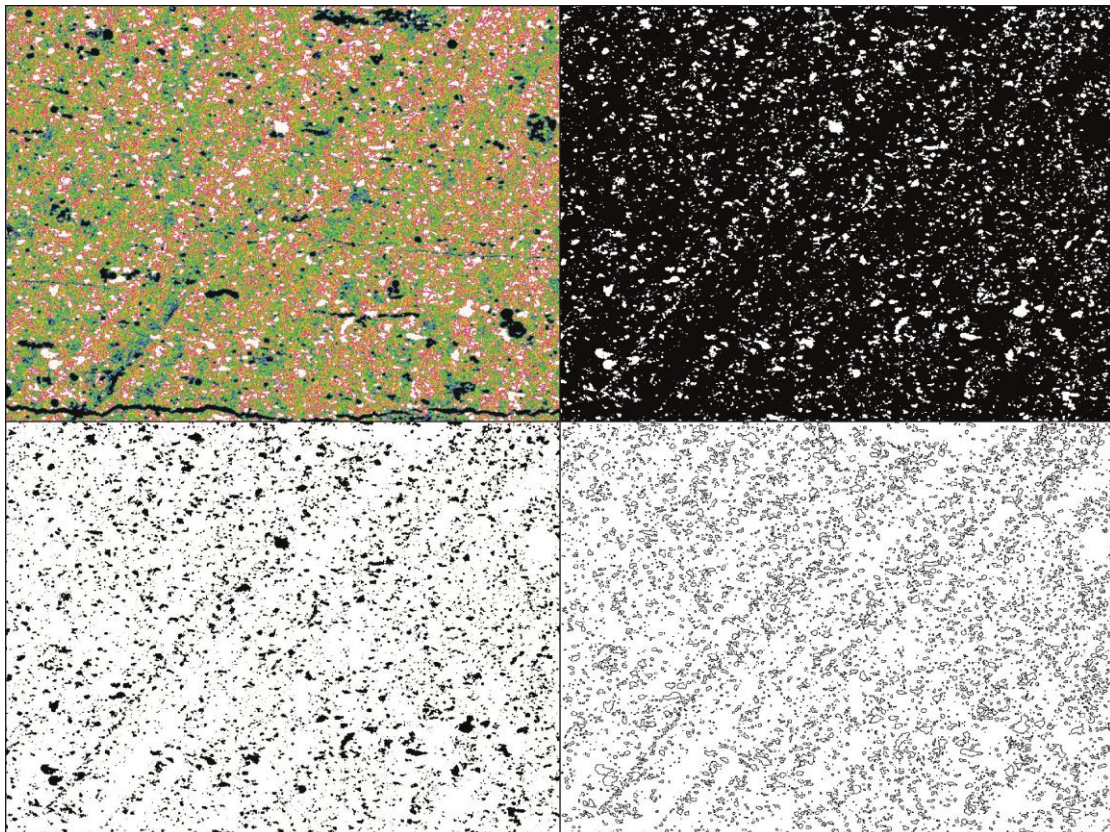
DN02 depth: 135,10 m

WMF – Alum Shale Member – Hard Shales



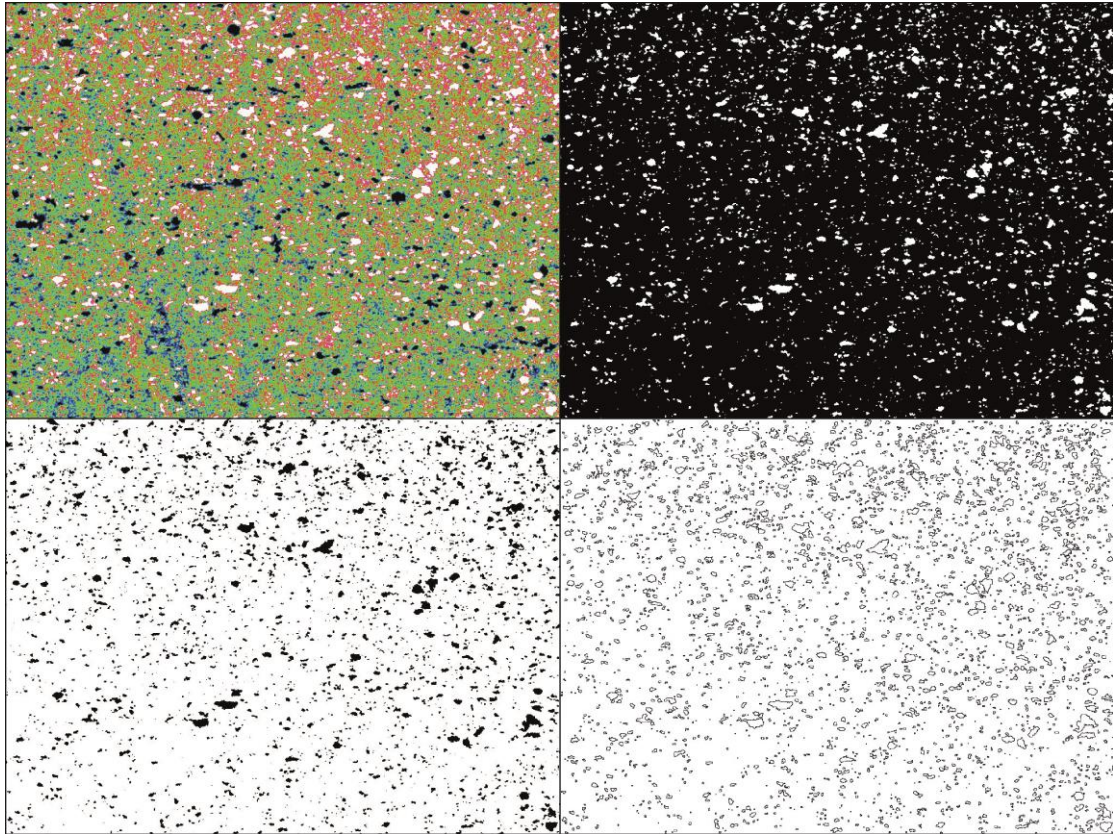
DN03 depth: 139,25 m

WMF – Alum Shale Member – Hard Shales



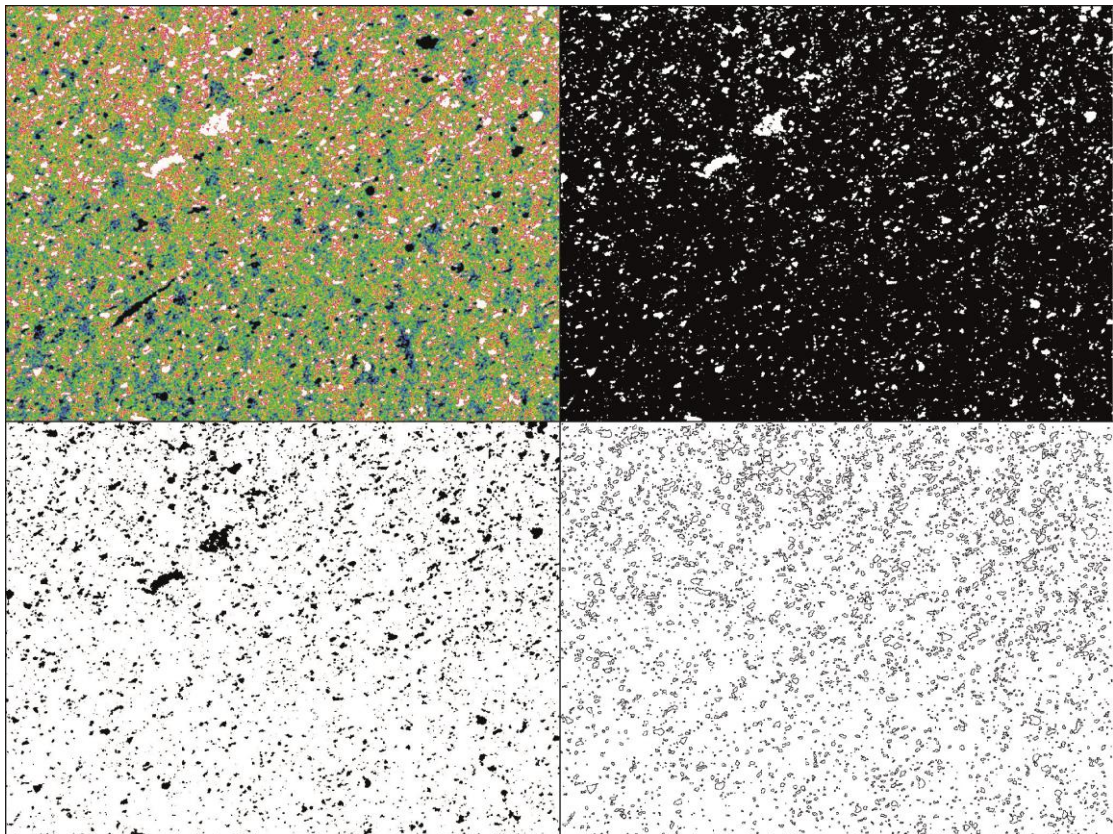
DN04 depth: 143,65 m

WMF – Mulgrave Shale Member – Bituminous Shales



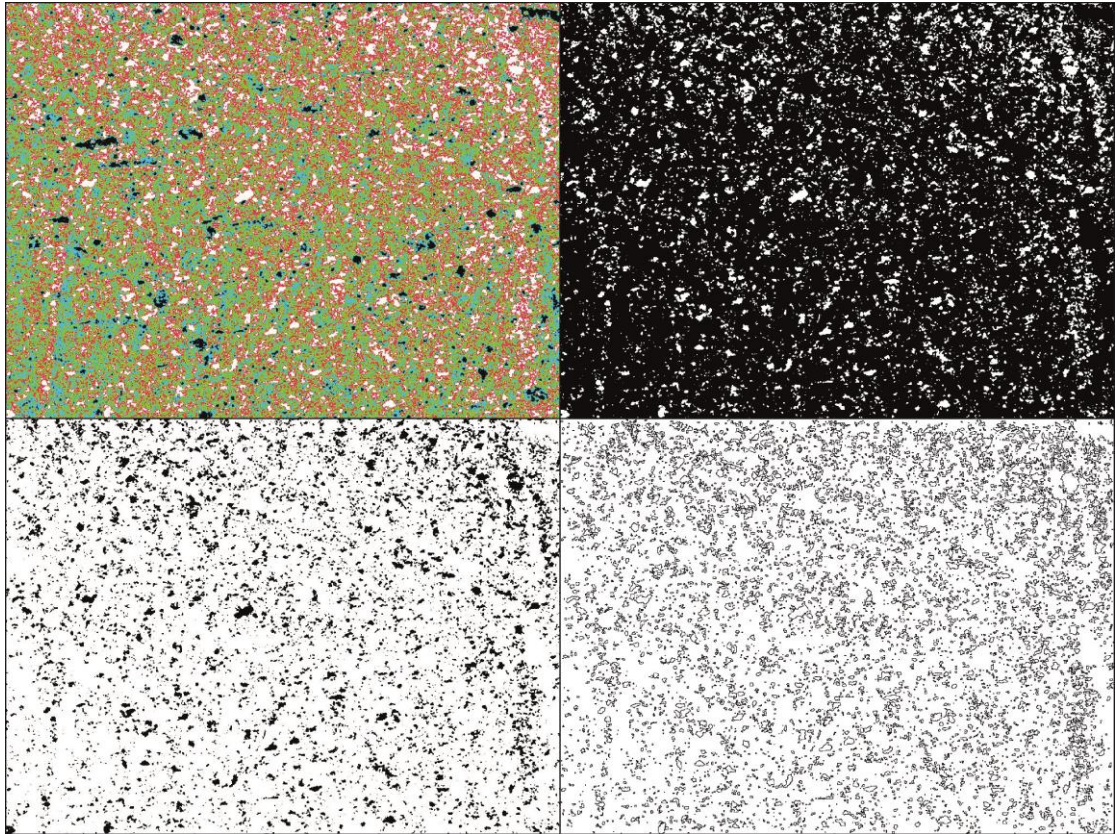
DN05 depth: 147,32 m

WMF – Mulgrave Shale Member – Bituminous Shales



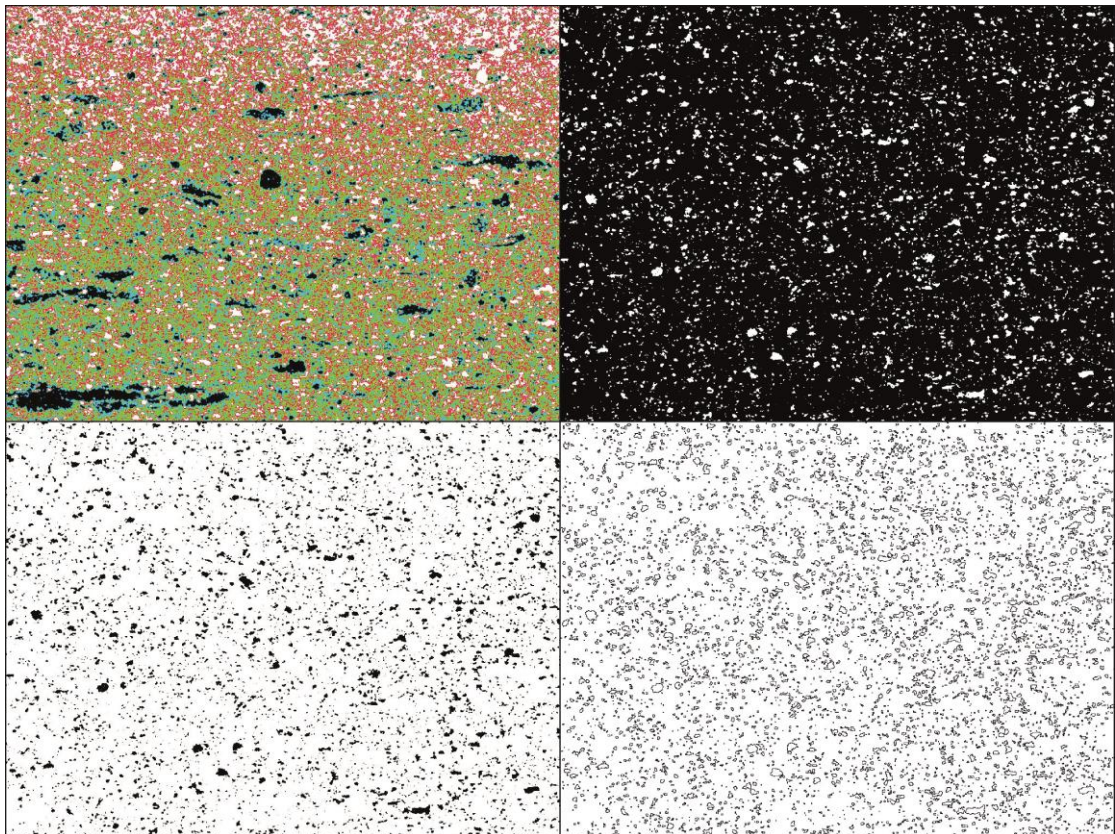
DN06 depth: 151,55 m

WMF – Mulgrave Shale Member – Bituminous Shales



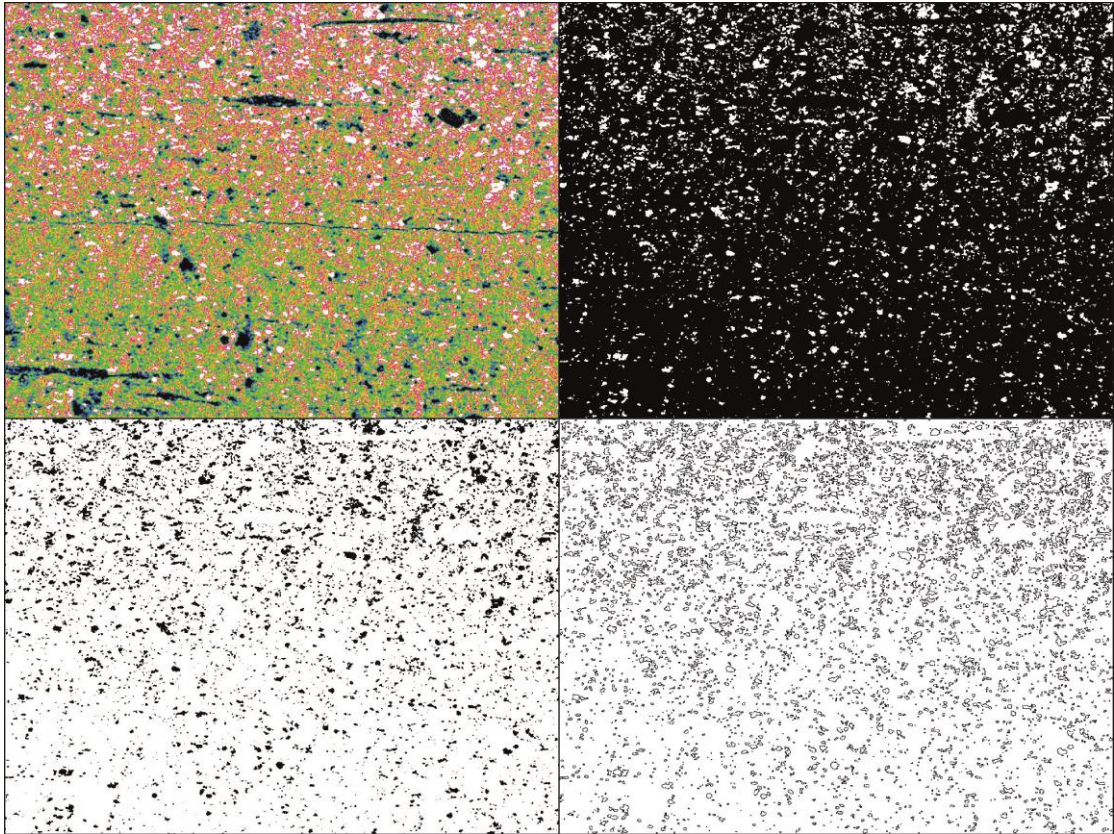
DN07 depth: 155,30 m

WMF – Mulgrave Shale Member – Bituminous Shales



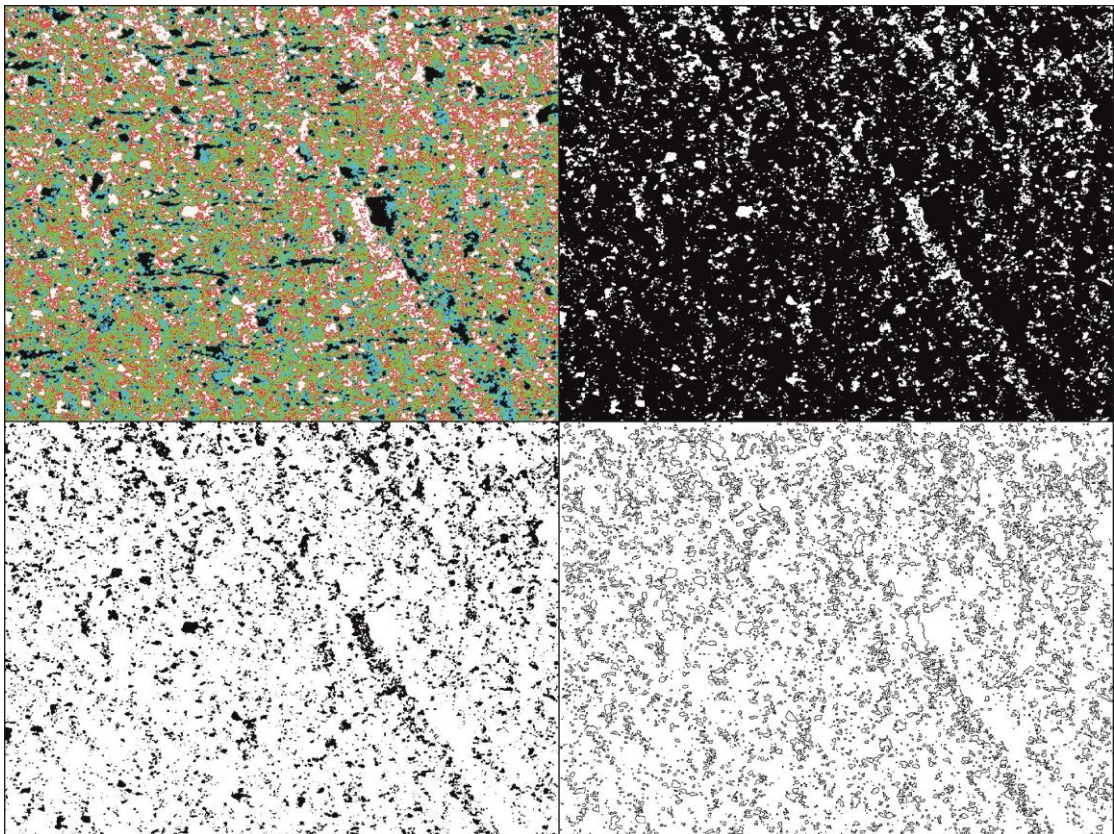
DN08 depth: 159,54 m

WMF – Mulgrave Shale Member – Bituminous Shales



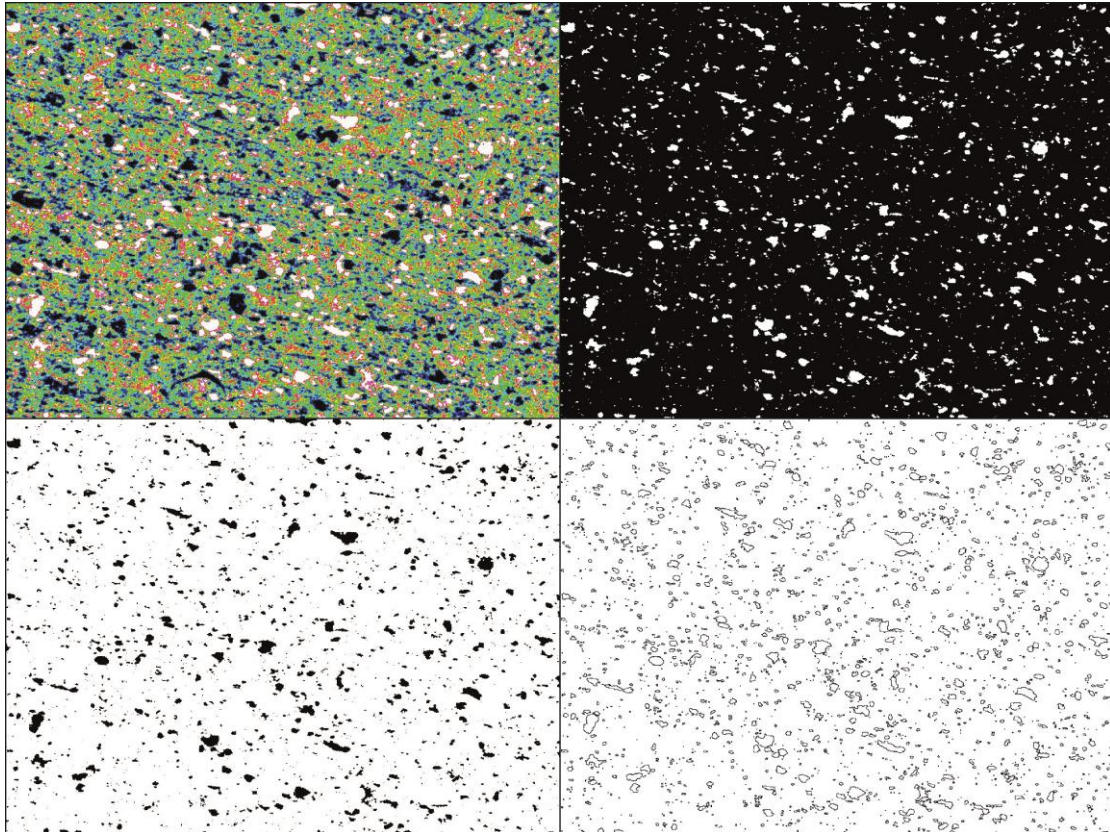
DN09 depth: 163,52 m

WMF – Mulgrave Shale Member – Bituminous Shales



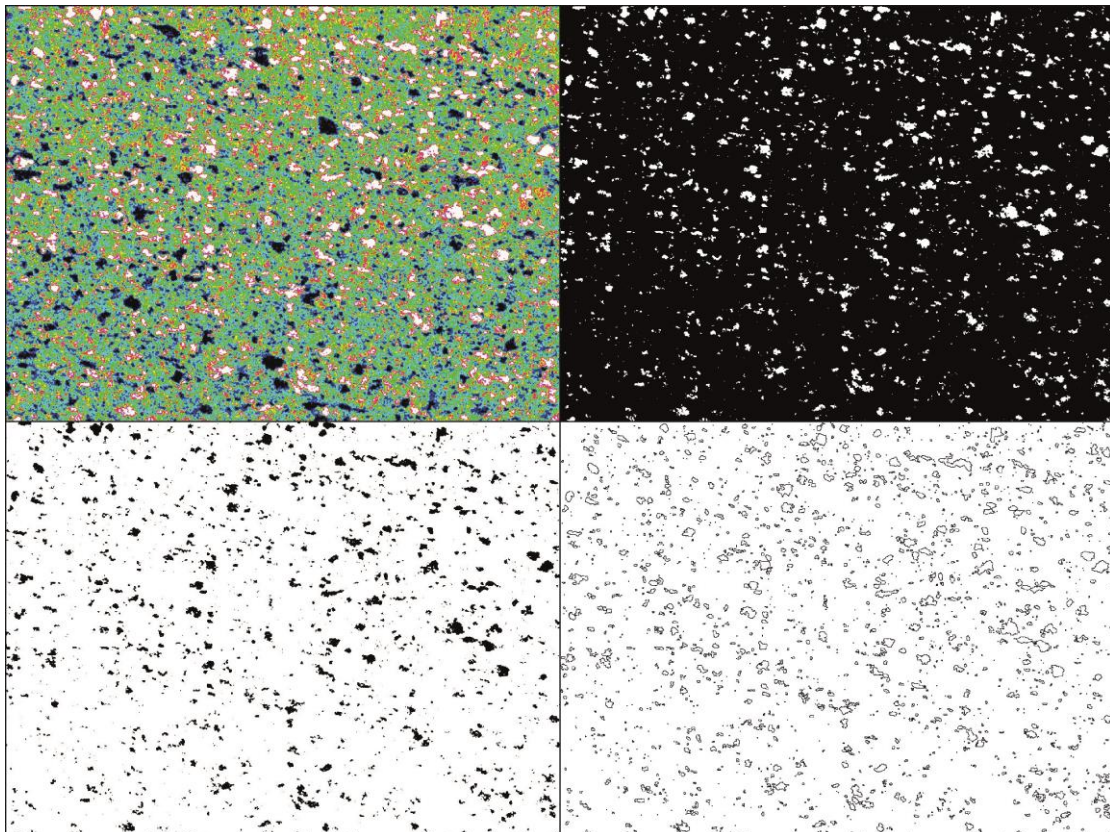
DN10 depth: 167,31 m

WMF – Mulgrave Shale Member - Jetrock



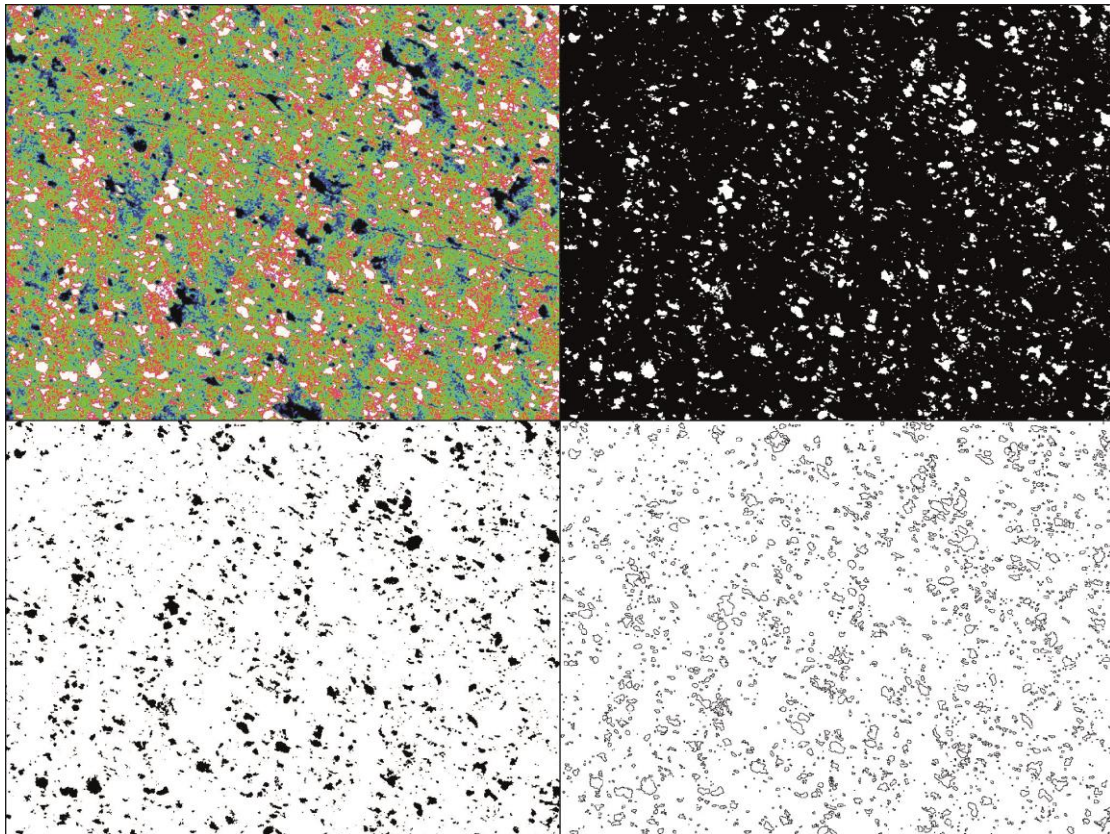
DN11 depth: 171,41 m

Whitby Mudstone Formation – Grey Shale Member



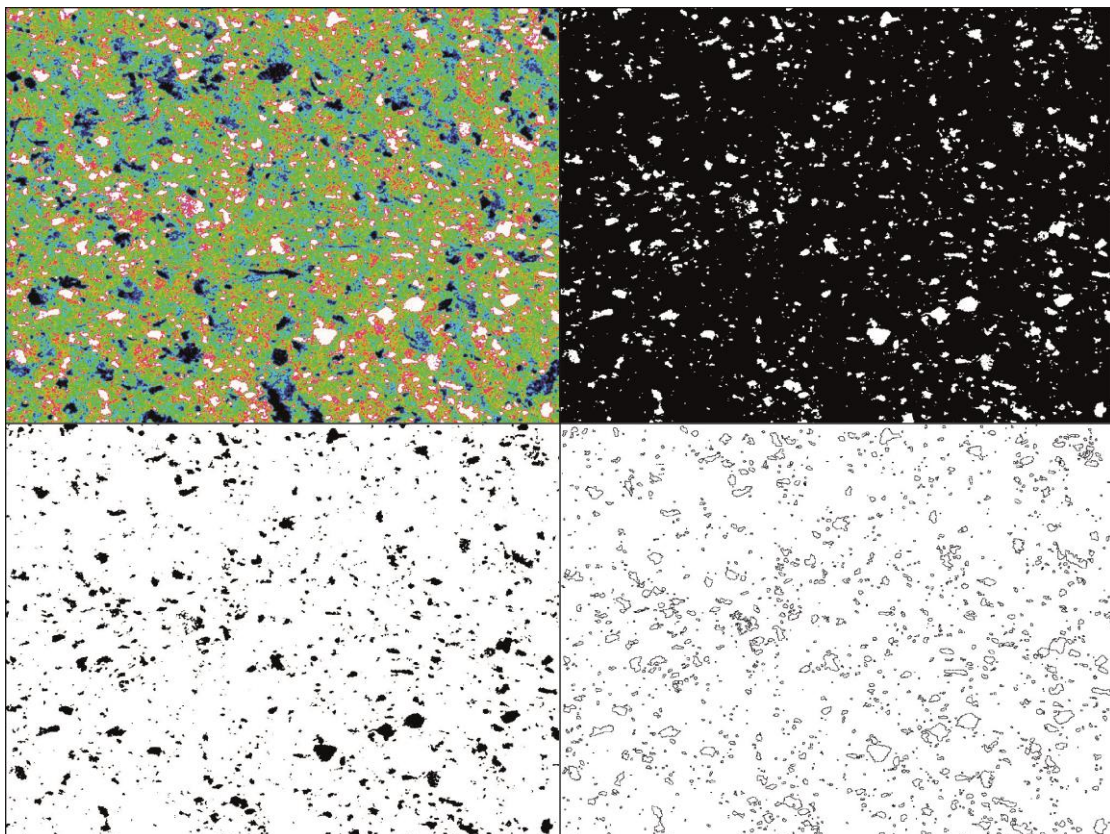
DN12 depth: 175,46 m

Whitby Mudstone Formation – Grey Shale Member



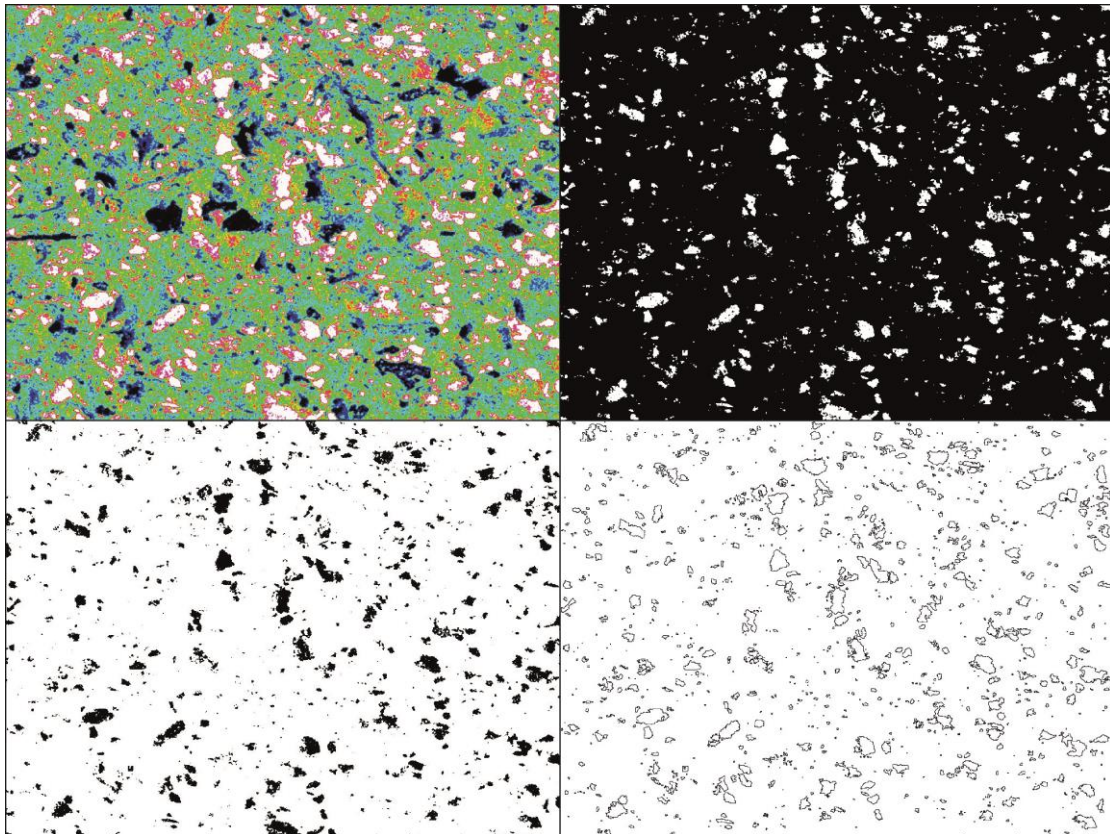
DN13 depth: 179,57 m

Whitby Mudstone Formation – Grey Shale Member



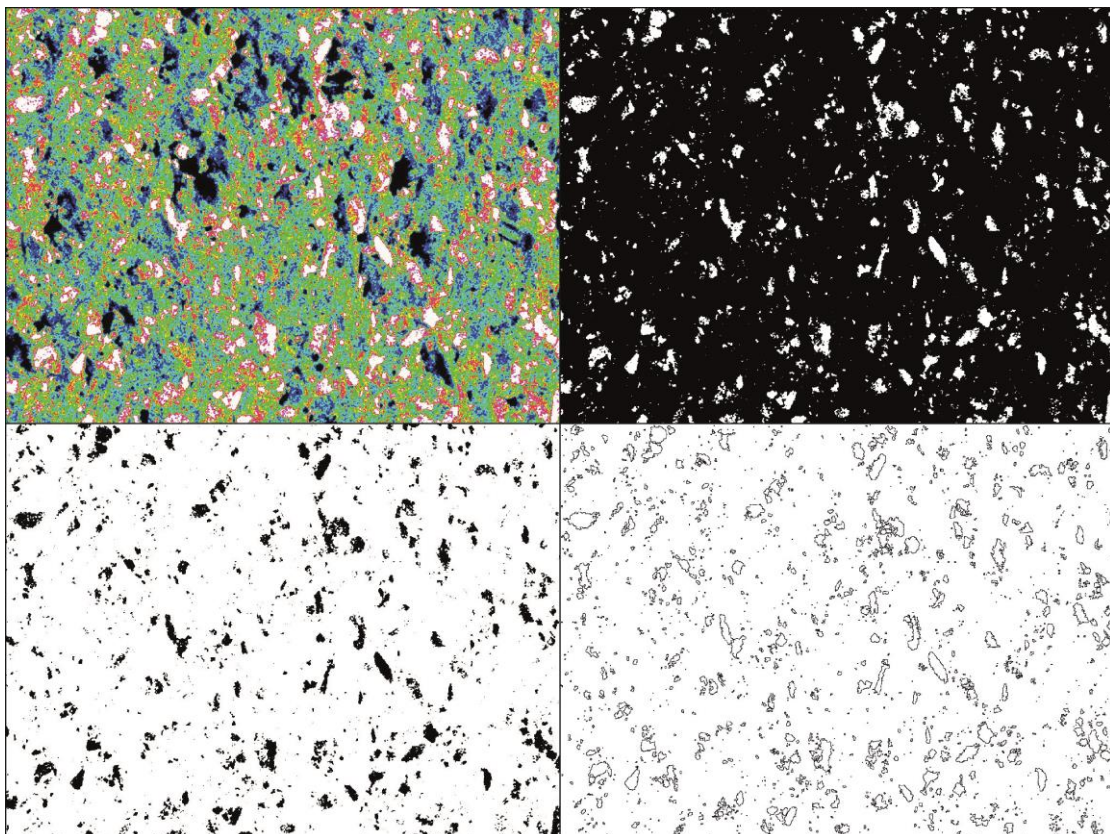
DN14 depth: 183,38 m

Whitby Mudstone Formation – Grey Shale Member



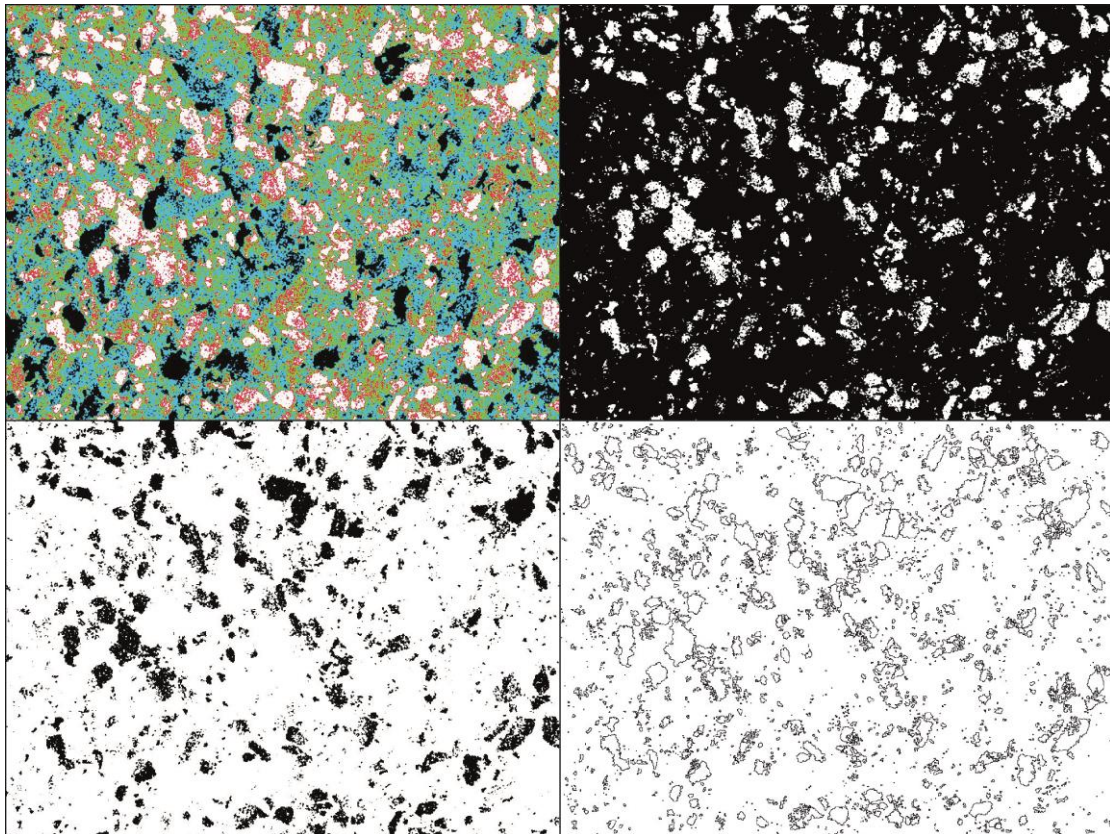
DN15 depth: 187,33 m

Cleveland Ironstone Formation – Kettleless Member



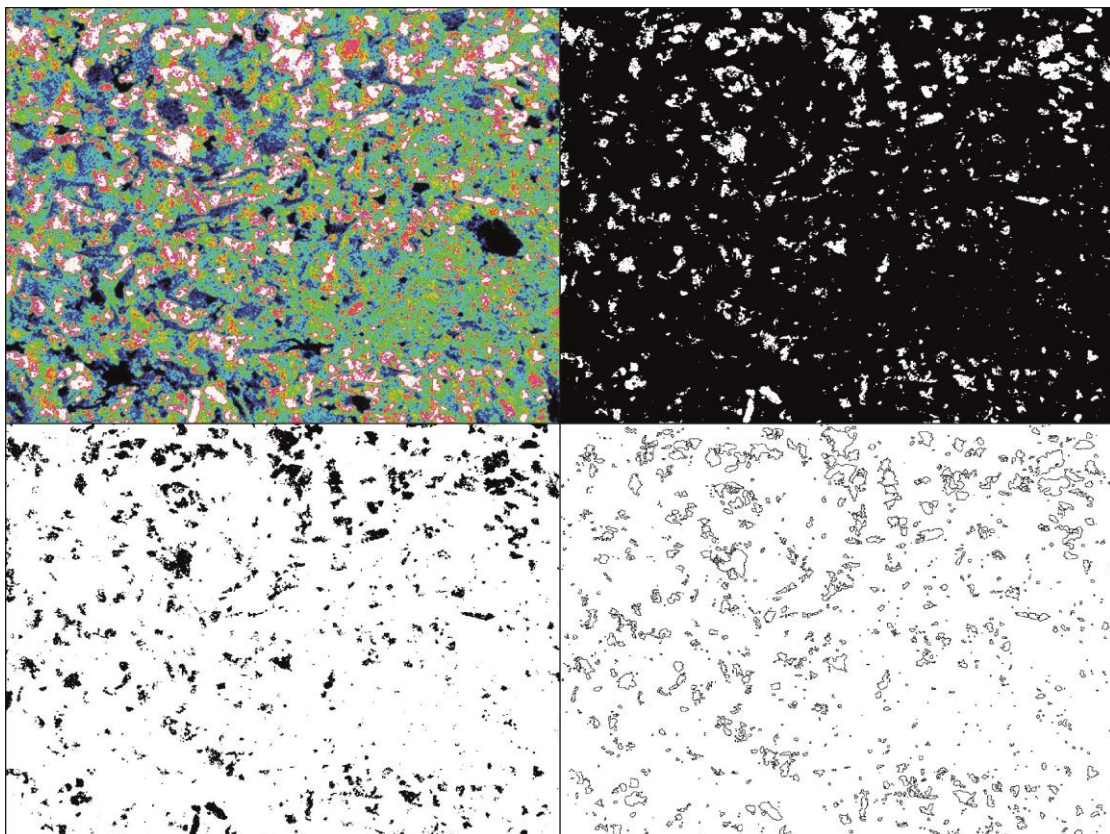
DN16 depth: 191,41 m

Cleveland Ironstone Formation – Kettleness Member



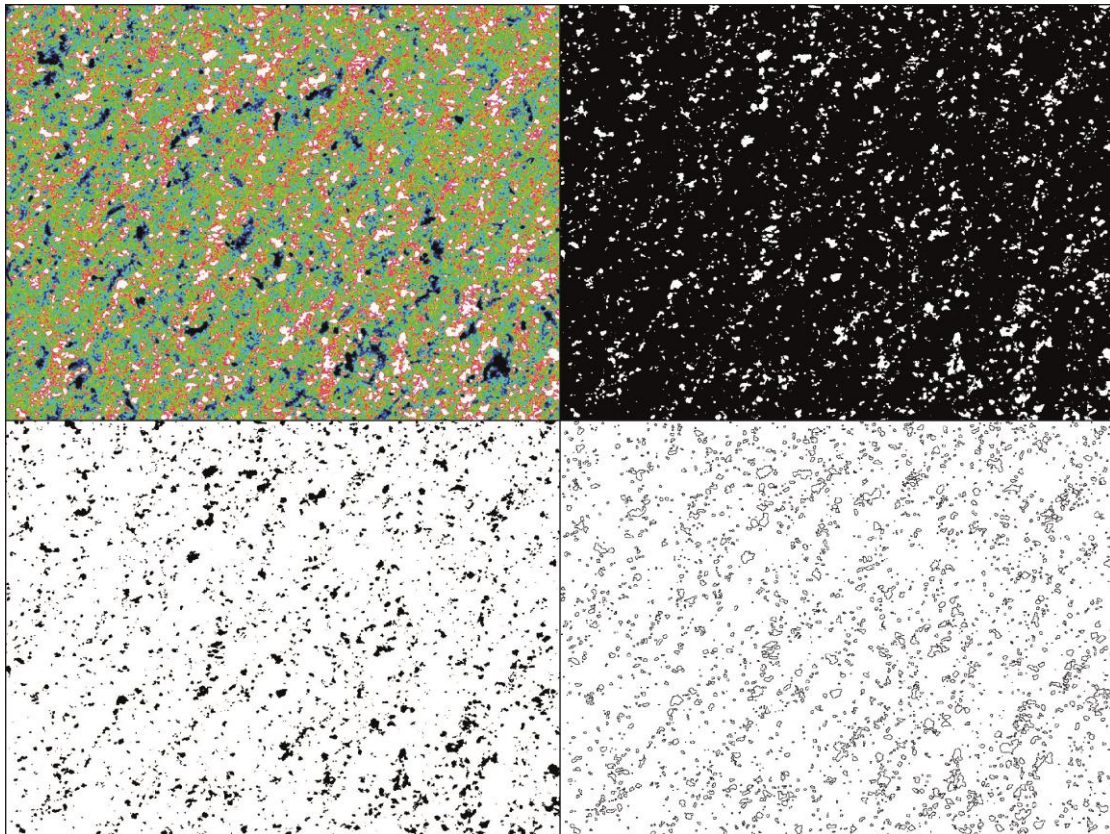
DN17 depth: 195,68 m

Cleveland Ironstone Formation – Penny Nab Member



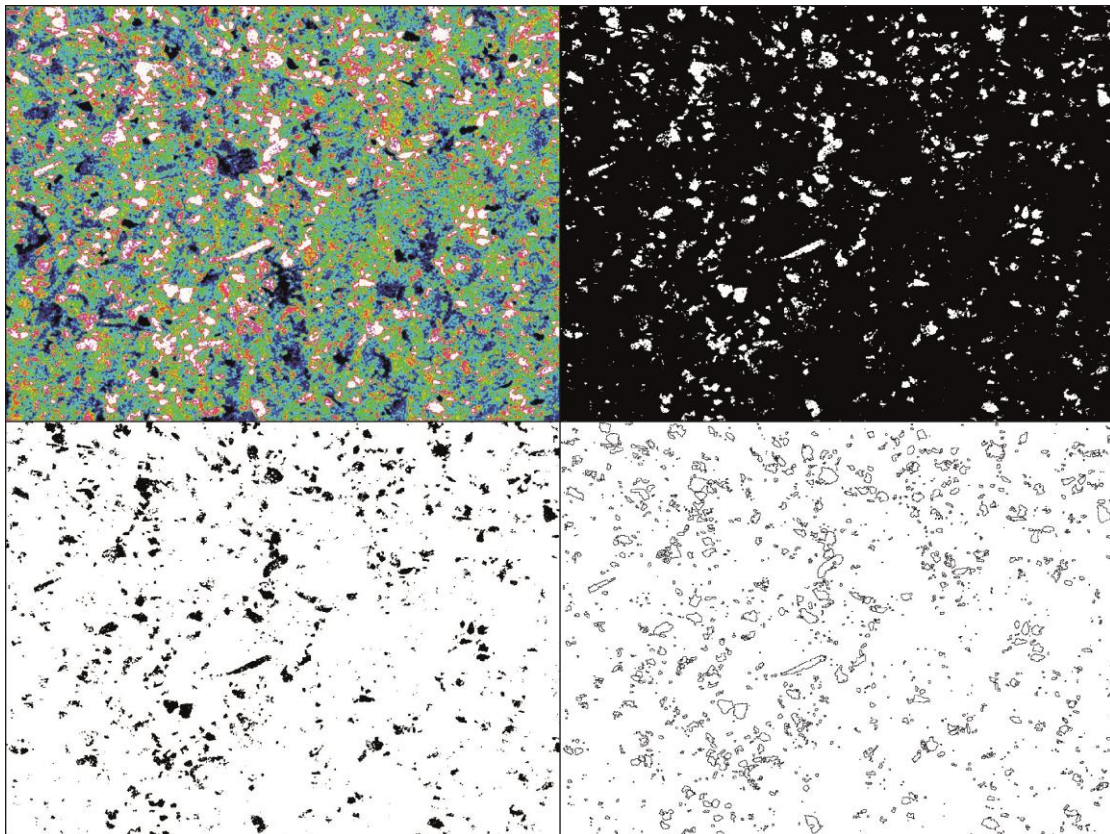
DN18 depth: 199,61 m

Cleveland Ironstone Formation – Penny Nab Member



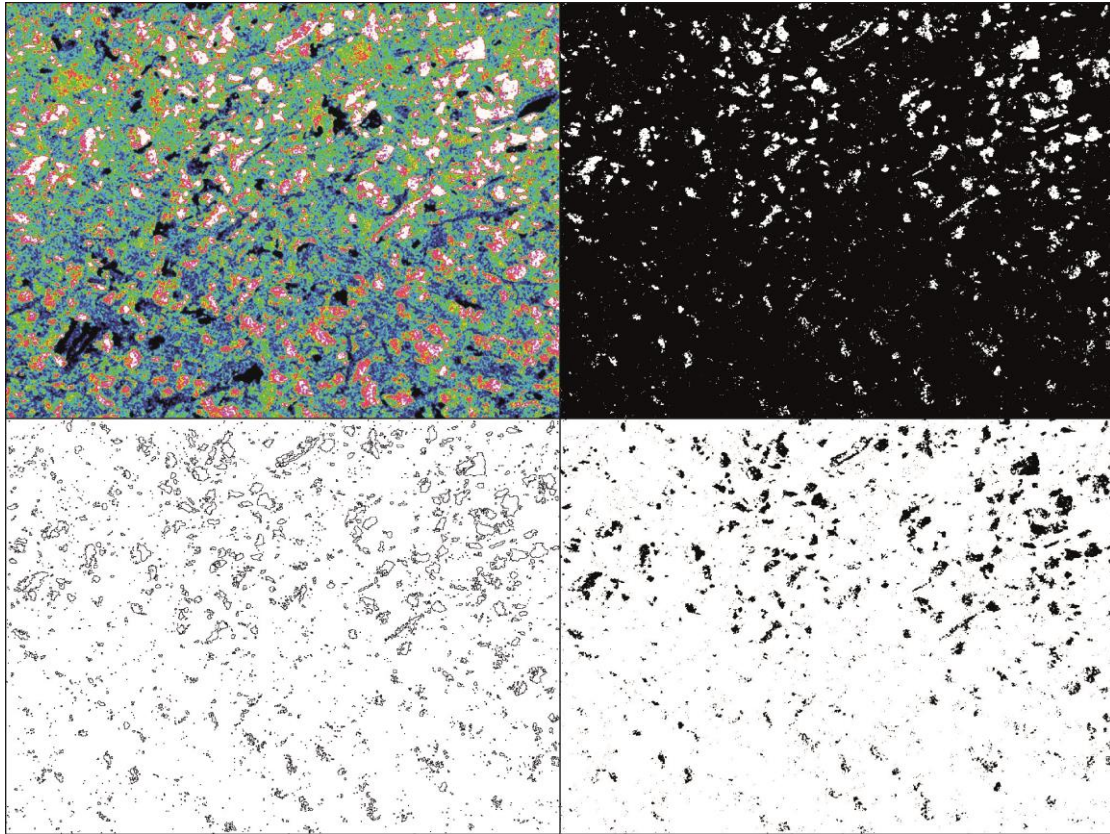
DN19 depth: 203,58 m

Cleveland Ironstone Formation – Penny Nab Member



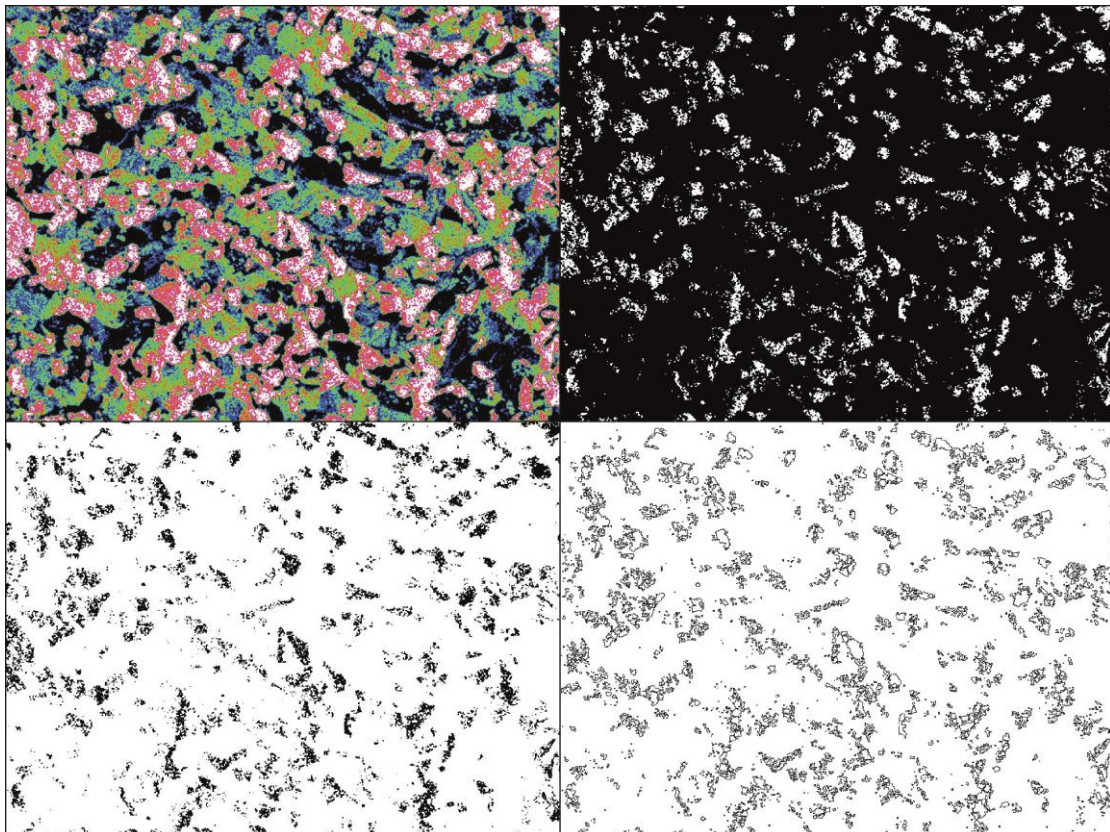
DN20 depth: 207,37 m

Cleveland Ironstone Formation – Penny Nab Member



DN21 depth: 211,75 m

Staites Sandstone Formation



Appendix C - Grain size distributions

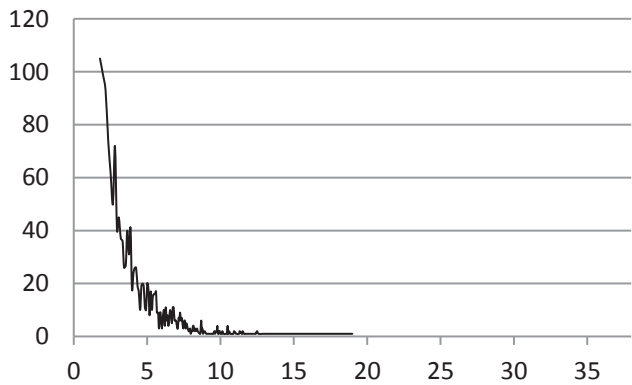
Grain size distribution per sample. All data is presented following the order described below and exemplified by sample DN01. Bin size applied for top two distributions (a & b) is 0.2 μm . Particles below 1.77 μm (4 px^2) are excluded from the count. The distribution per class (c) is based on Wentworth's (1922) grain size classification for silt. "Clay" refers to 1.77-3.91 μm fraction.

DN01
 core depth: 130,75 m
 total grain count: 1610
 max grain size: 18.99 μm
 mean grain size: 4.39 μm

a) Grain count versus size

Original data ($> 1.77 \mu\text{m}$)

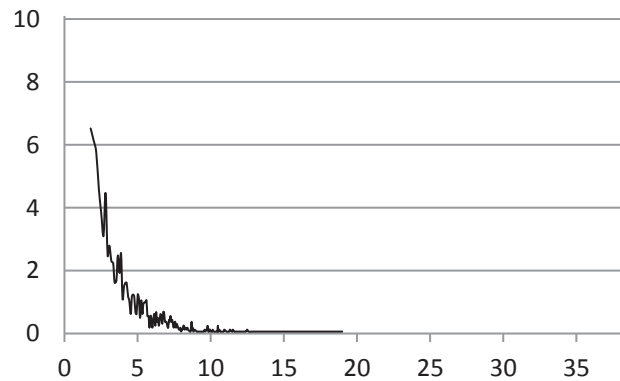
x-axis: grain size (μm)
 y-axis: number of grains (i.e. count)



b) Normalized abundance versus size

Normalized data: $\frac{\text{grain count}}{\text{total count}} * 100\%$

x-axis: grain size (μm)
 y-axis: abundance (%)

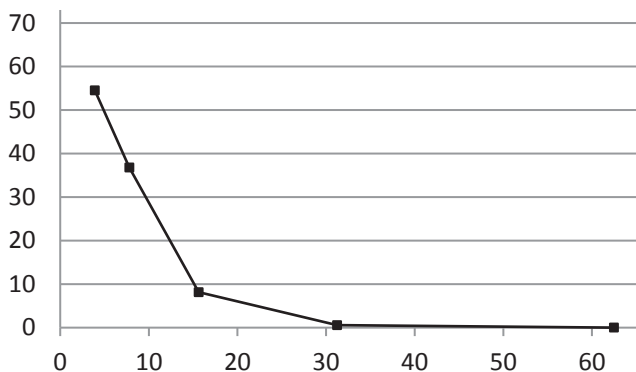


c) Normalized abundance per class

Grain size distribution per size class

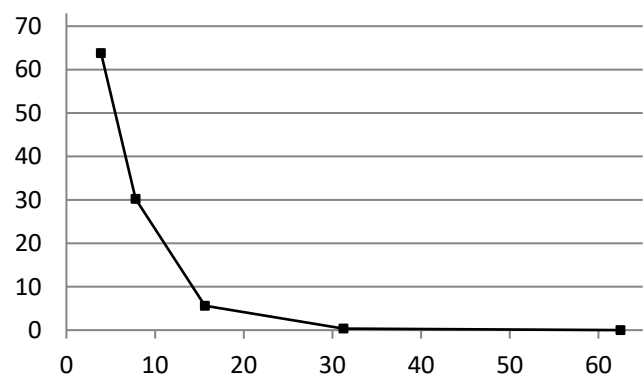
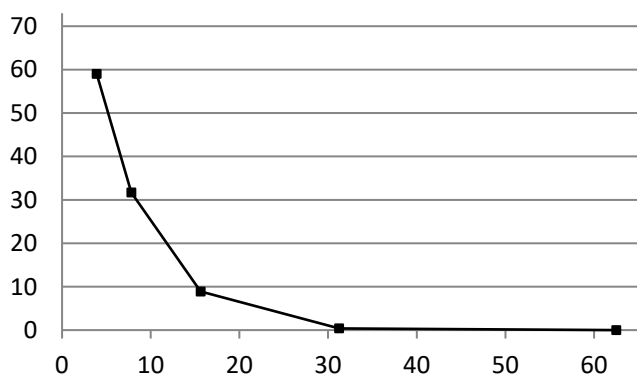
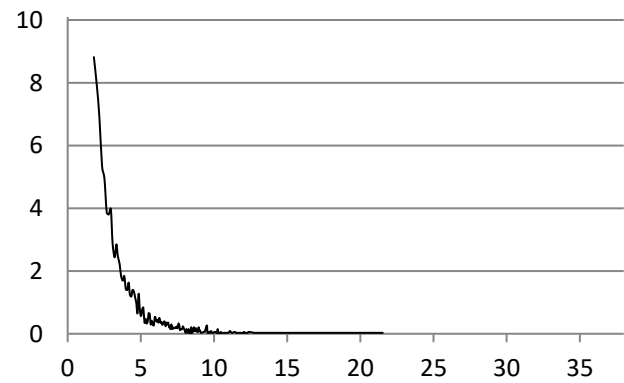
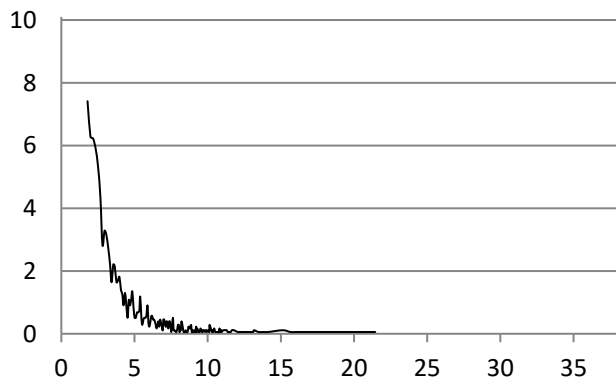
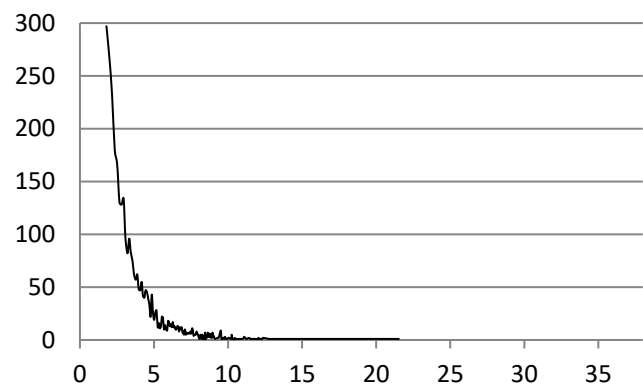
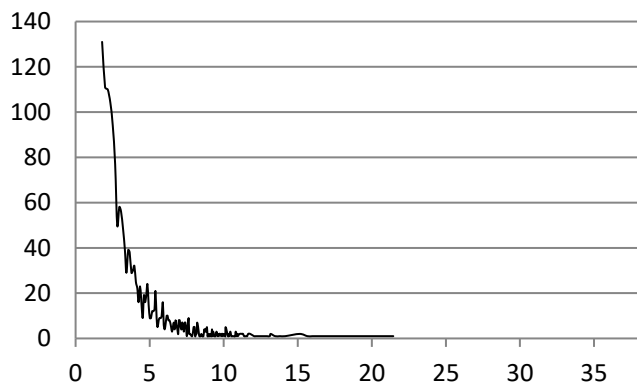
clay	< 3.91	μm
Very-fine	< 7.81	μm
Fine	< 15.625	μm
Medium	< 31.25	μm
Coarse	< 62.5	μm

x-axis: grain size (μm)
 y-axis: abundance (%)



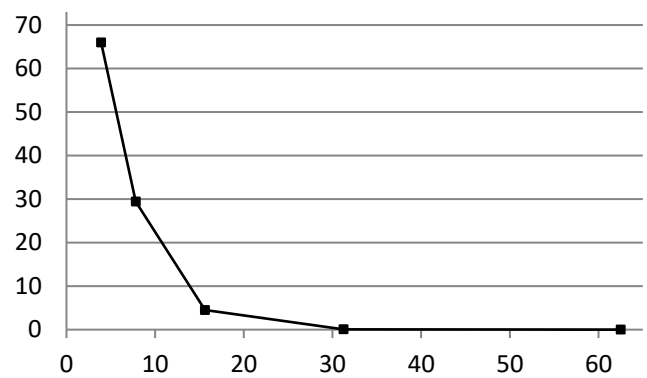
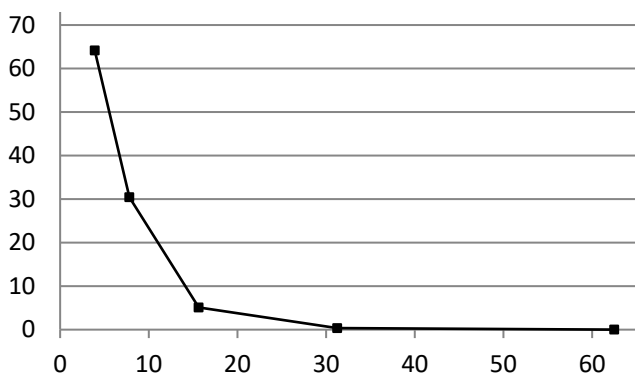
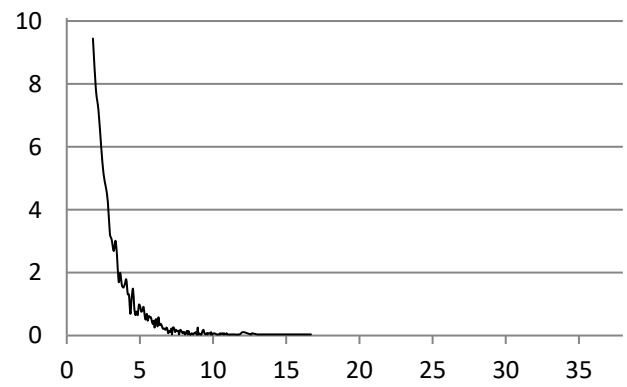
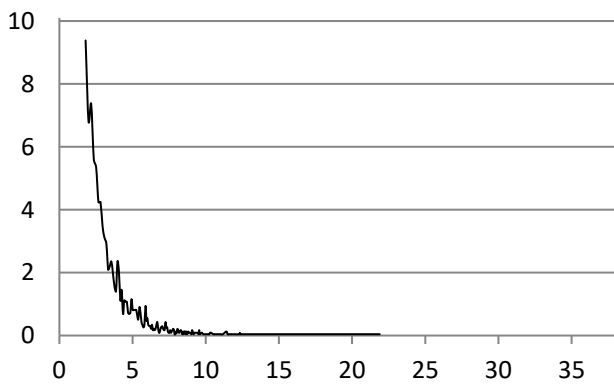
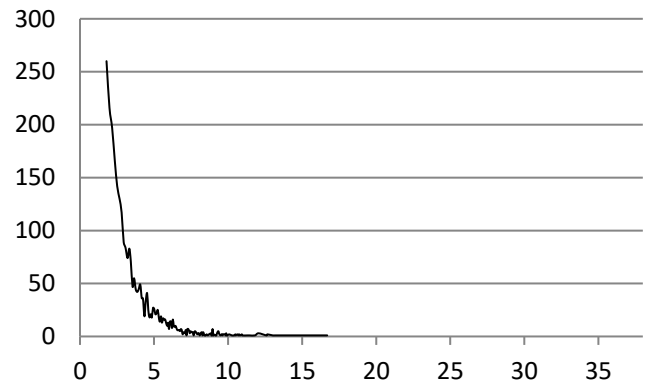
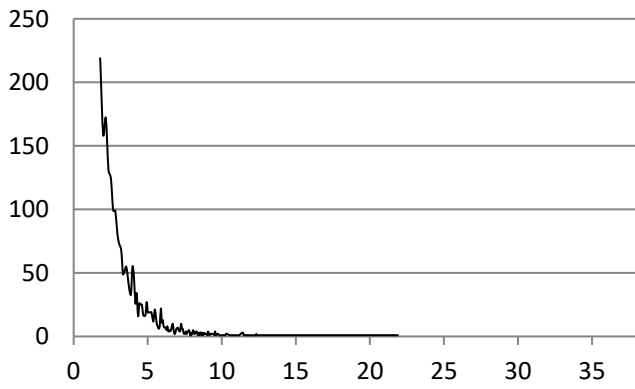
DN02
 core depth: 135,10 m
 total grain count: 1767
 max grain size: 21.44 μm
 mean grain size: 4.22 μm

DN03
 core depth: 139,25 m
 total grain count: 3368
 max grain size: 21.52 μm
 mean grain size: 3.88 μm



DN04
core depth: 143,65 m
total grain count: 2334
max grain size: 21.88 μm
mean grain size: 3.83 μm

DN05
core depth: 147,32 m
total grain count: 2753
max grain size: 16.68 μm
mean grain size: 3.70 μm

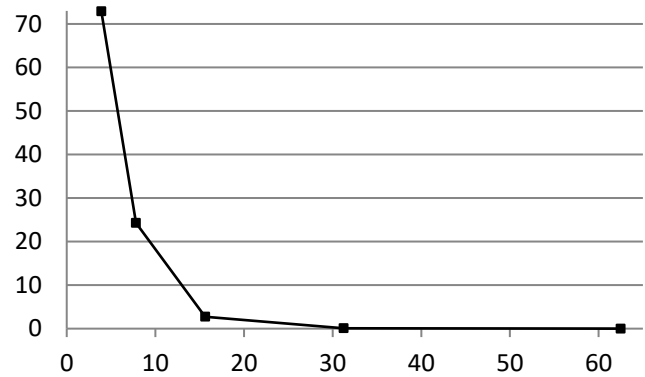
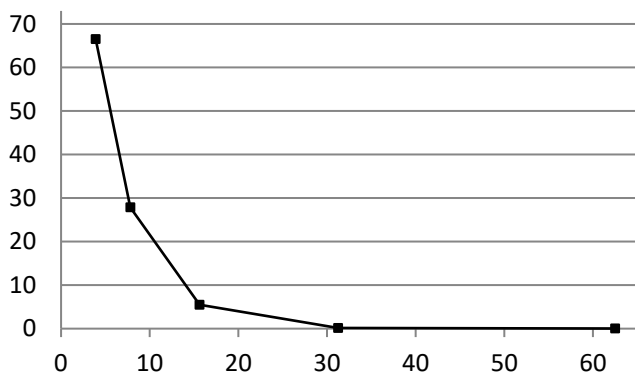
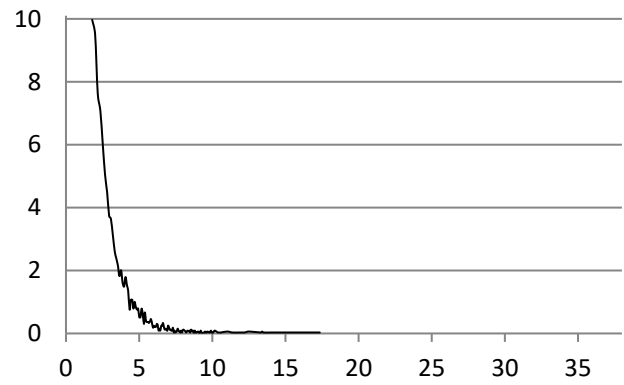
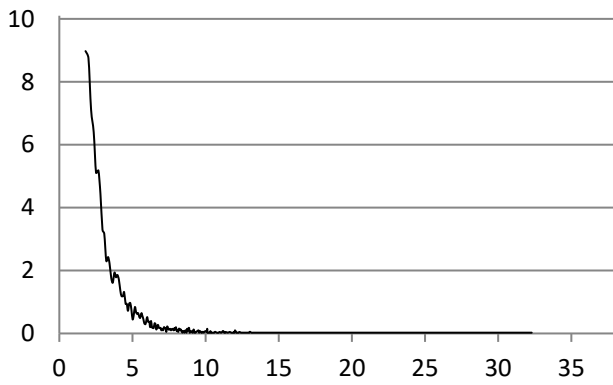
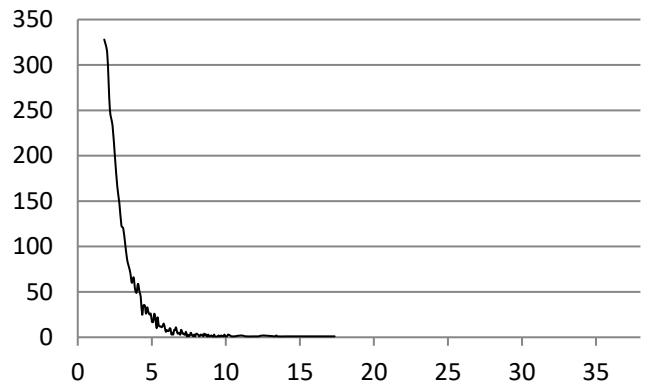
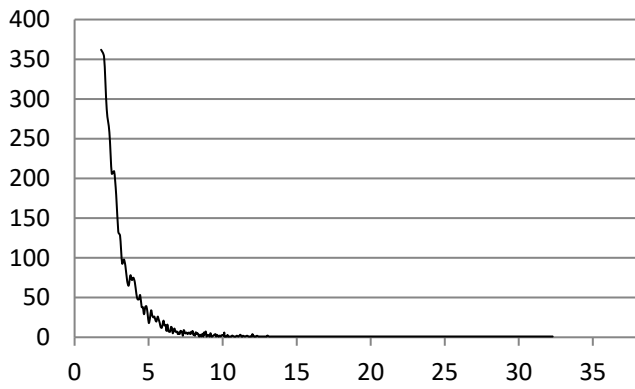


DN06

core depth: 151,55 m
total grain count: 4033
max grain size: 32,29 μm
mean grain size: 3.74 μm

DN07

core depth: 155,30 m
total grain count: 3290
max grain size: 17.34 μm
mean grain size: 3.40 μm

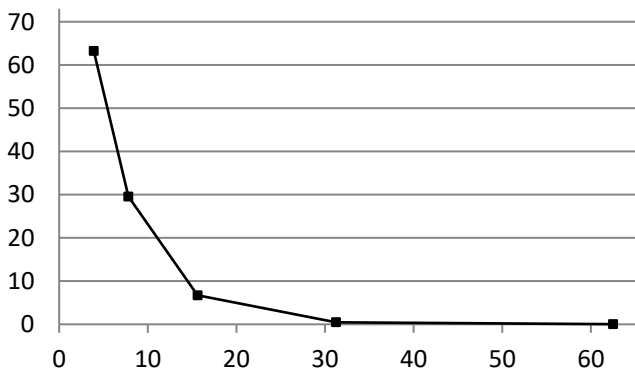
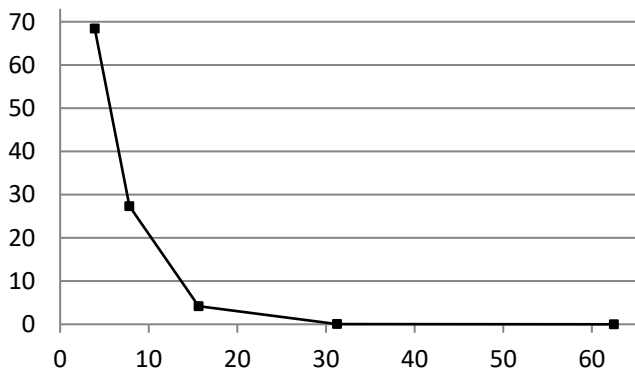
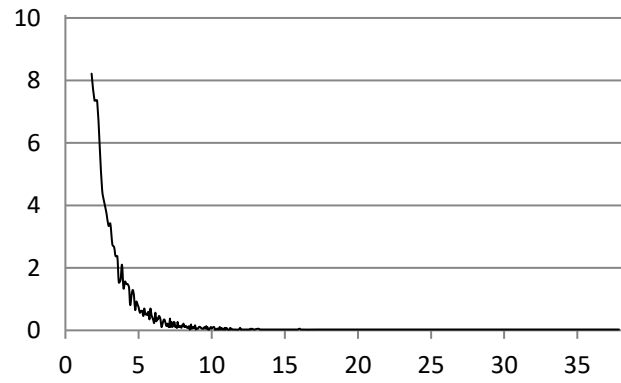
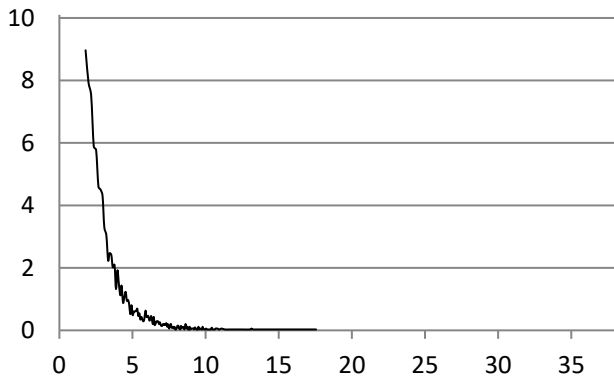
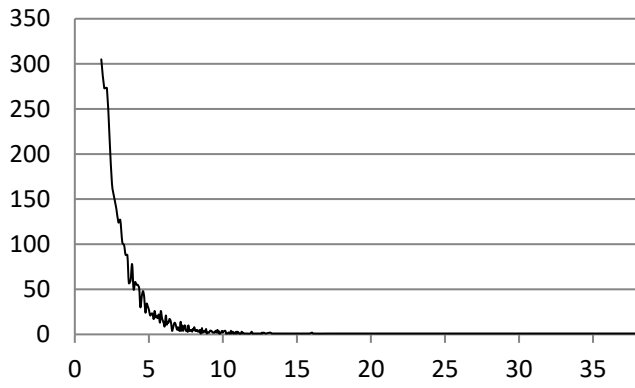
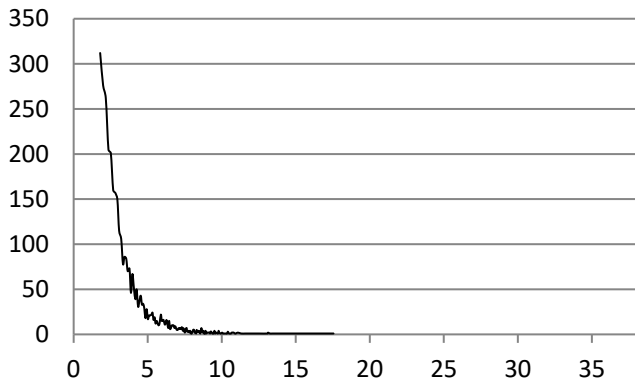


DN08

core depth: 159,54 m
total grain count: 3480
max grain size: 17.55 μm
mean grain size: 3.63 μm

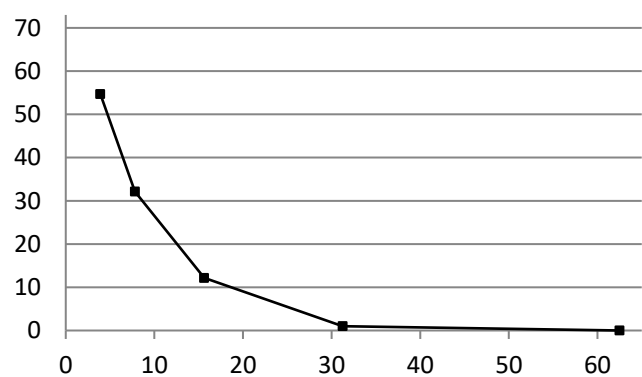
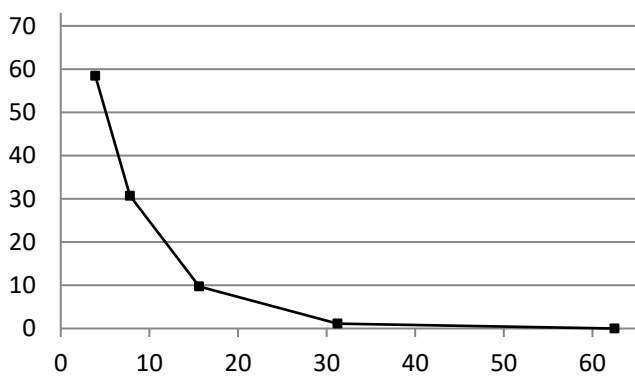
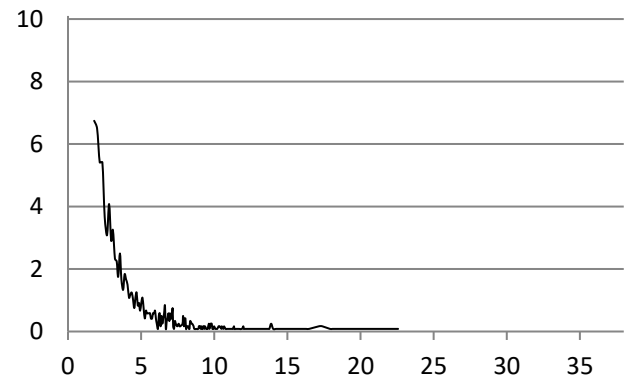
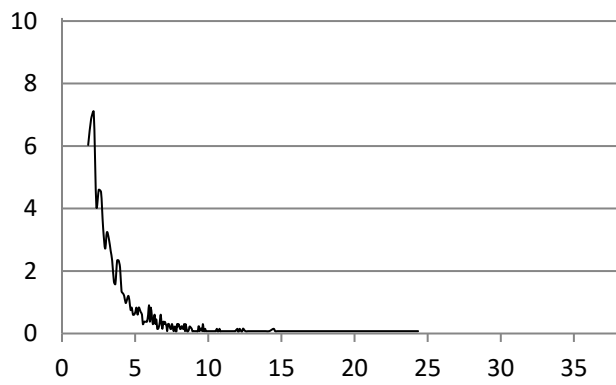
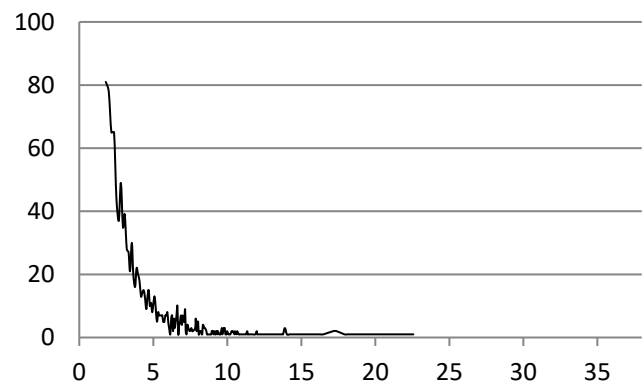
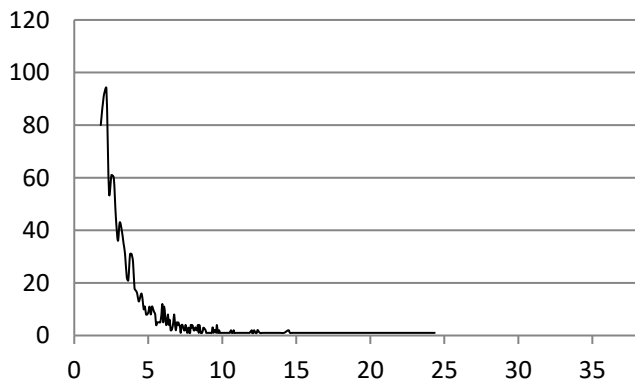
DN09

core depth: 167,31 m
total grain count: 3712
max grain size: 37.84 μm
mean grain size: 3.98 μm



DN10
 core depth: 167,31 m
 total grain count: 1326
 max grain size: 24.33 μm
 mean grain size: 4.40 μm

DN11
 core depth: 171,41 m
 total grain count: 1201
 max grain size: 22.56 μm
 mean grain size: 4.61 μm

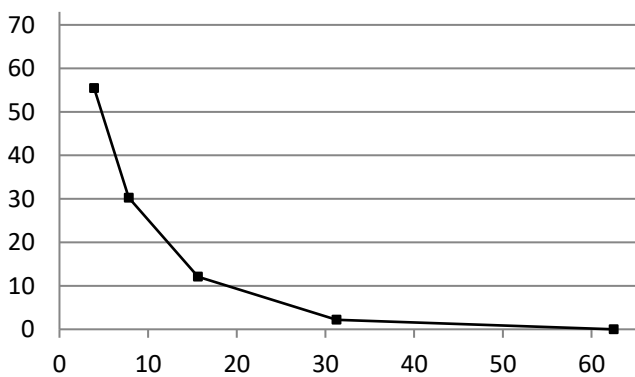
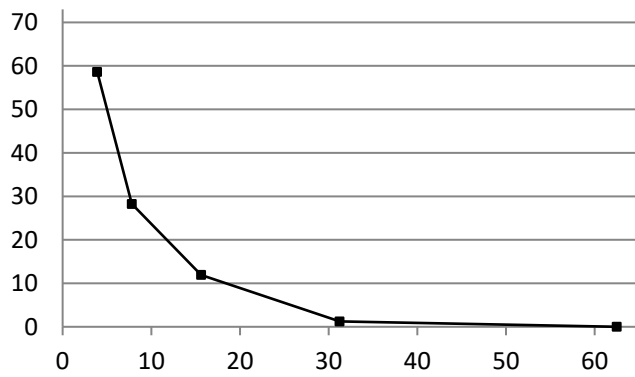
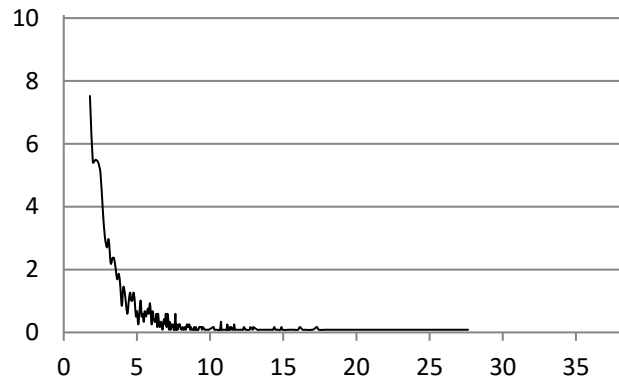
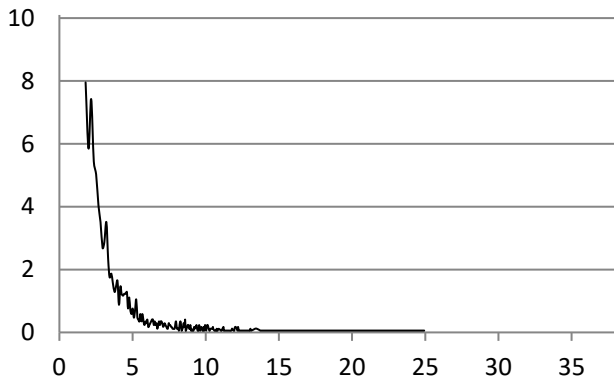
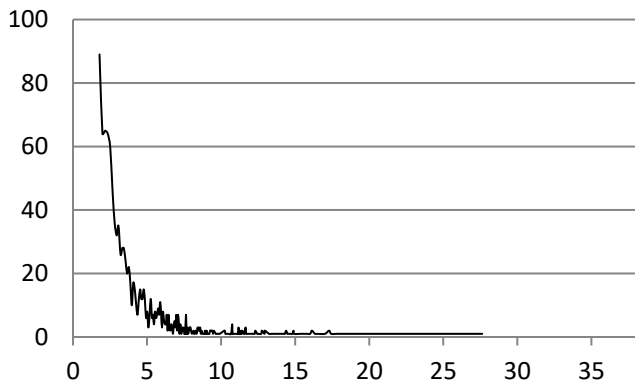
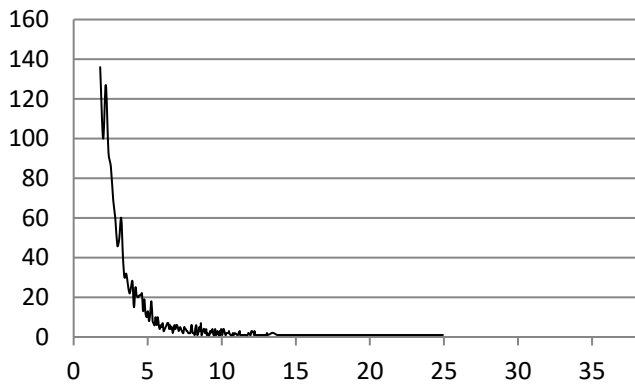


DN12

core depth: 175,46 m
total grain count: 1710
max grain size: 24.92 μm
mean grain size: 4.45 μm

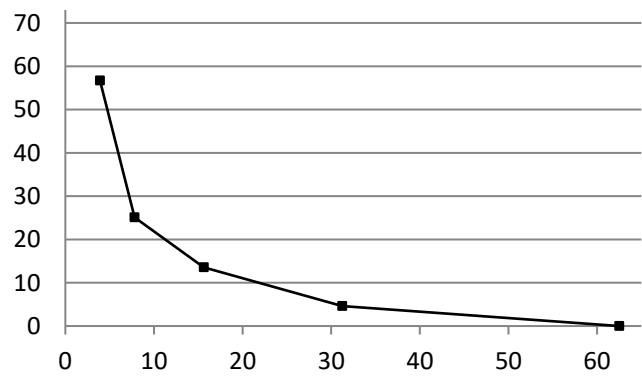
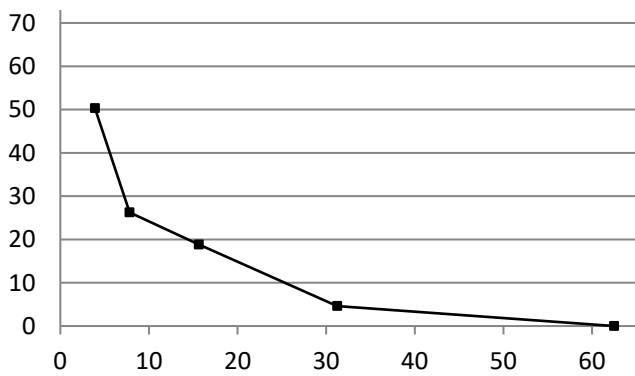
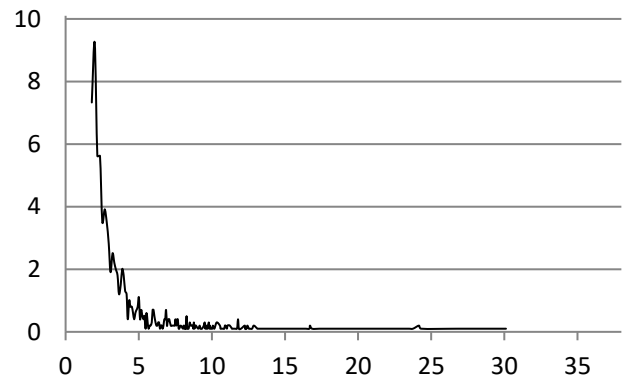
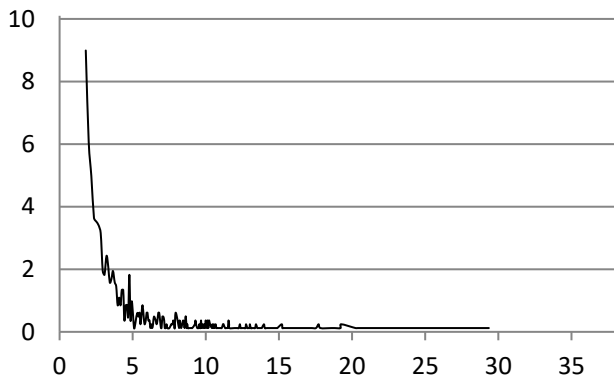
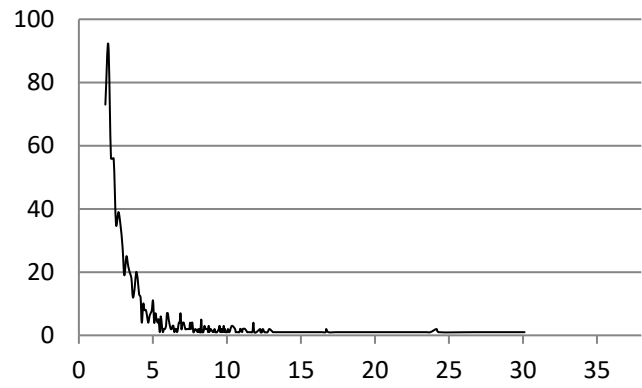
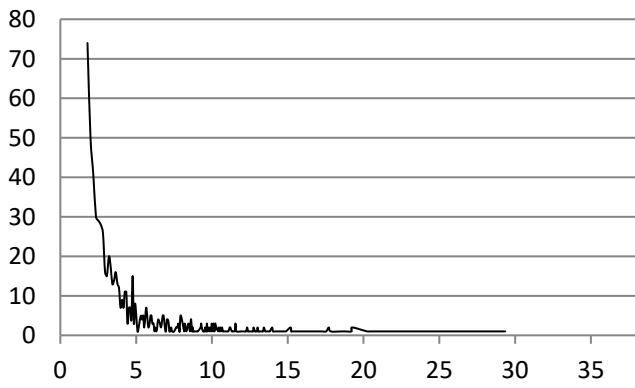
DN13

core depth: 179,57 m
total grain count: 1183
max grain size: 27.62 μm
mean grain size: 4.84 μm



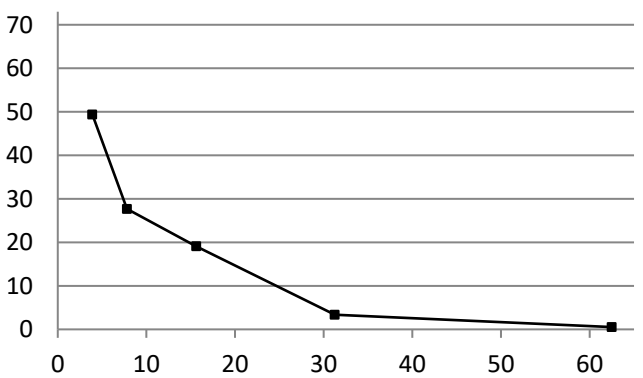
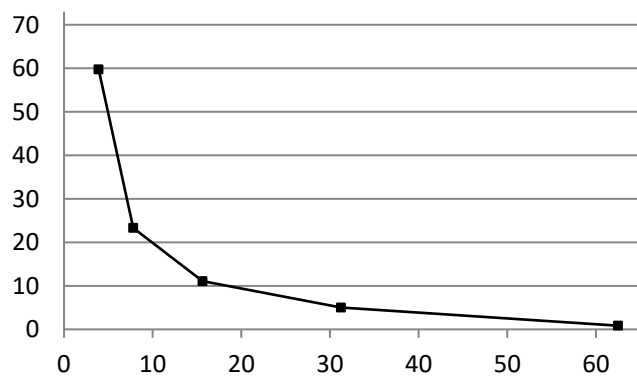
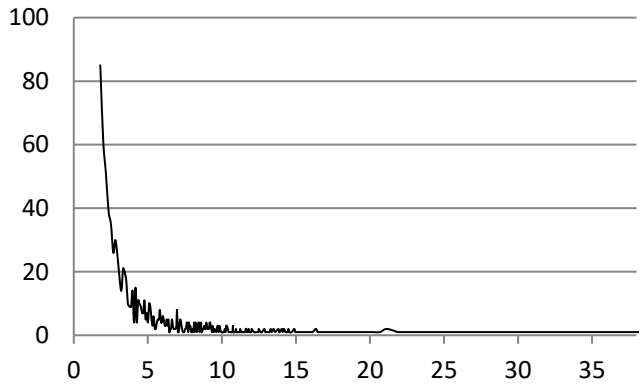
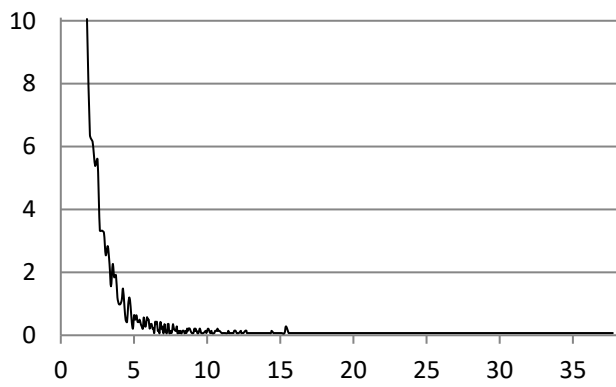
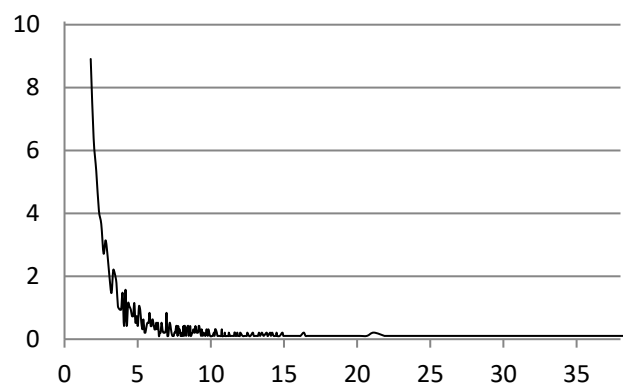
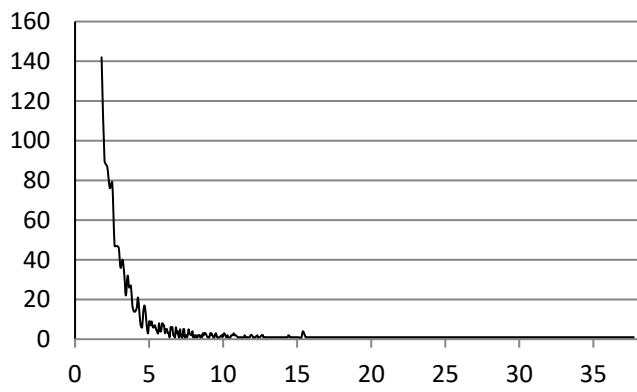
DN14
 core depth: 183,38 m
 total grain count: 823
 max grain size: 29.34 μm
 mean grain size: 5.76 μm

DN15
 core depth: 187,33 m
 total grain count: 996
 max grain size: 30.09 μm
 mean grain size: 5.20 μm



DN16
 core depth: 191,41 m
 total grain count: 1416
 max grain size: 51.54 μm
 mean grain size: 5.37 μm

DN17
 core depth: 195,68 m
 total grain count: 954
 max grain size: 45,54 μm
 mean grain size: 5.62 μm

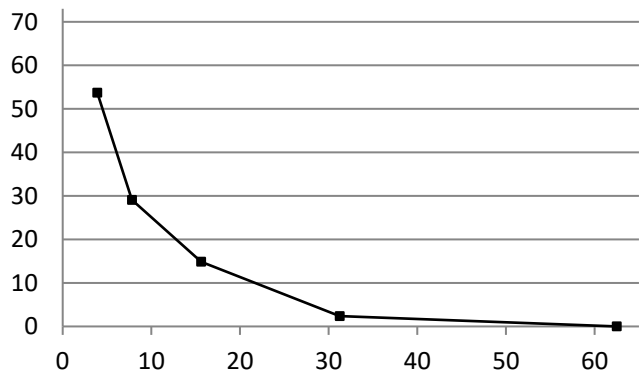
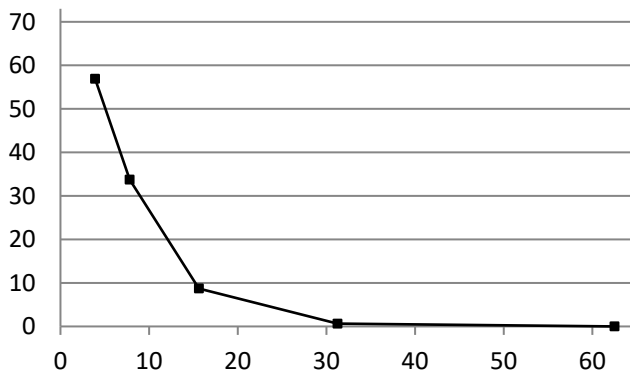
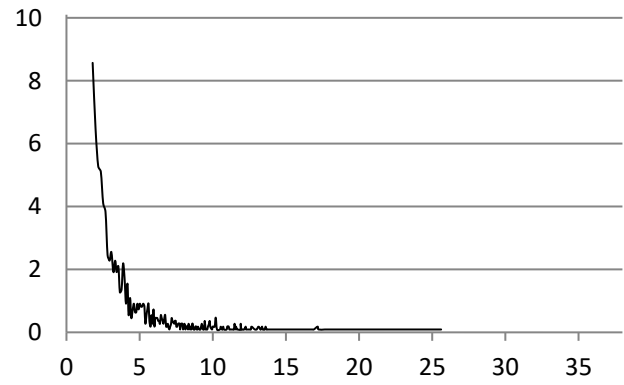
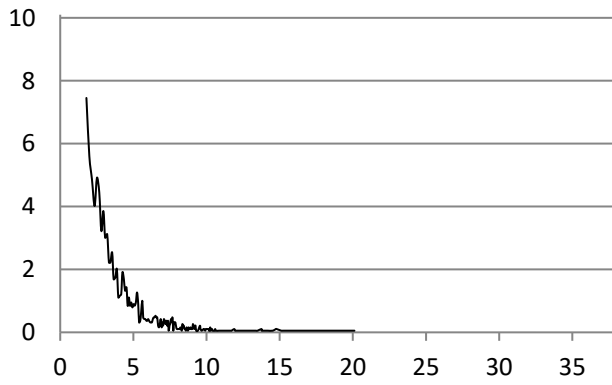
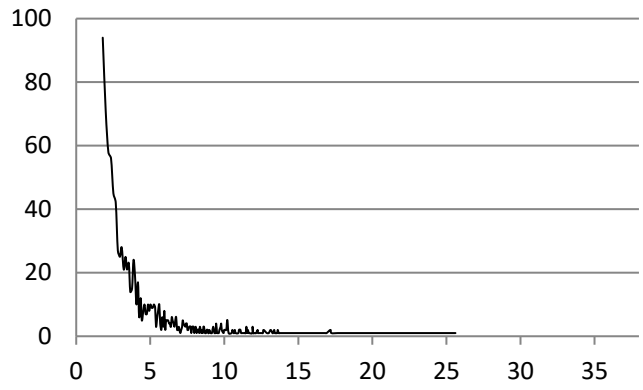
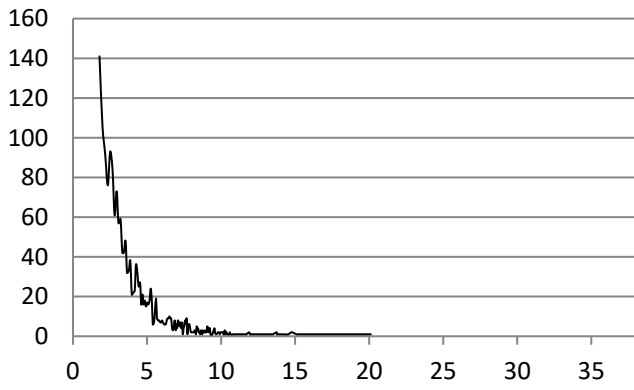


DN18

core depth: 199,61 m
total grain count: 1892
max grain size: 20.10 μm
mean grain size: 4.32 μm

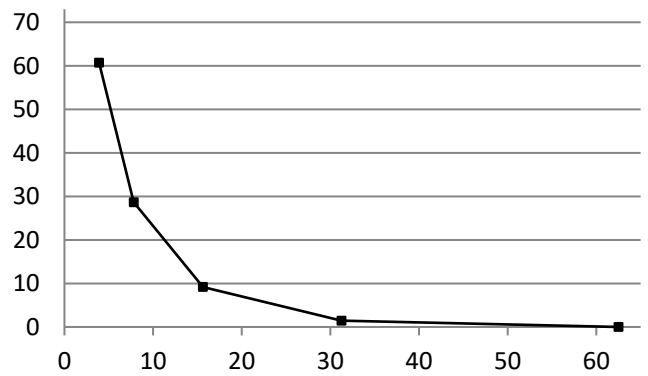
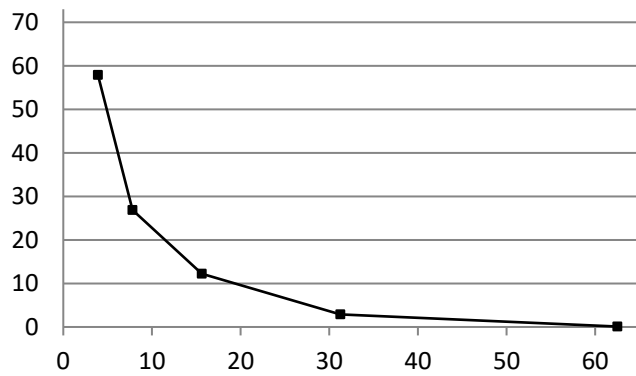
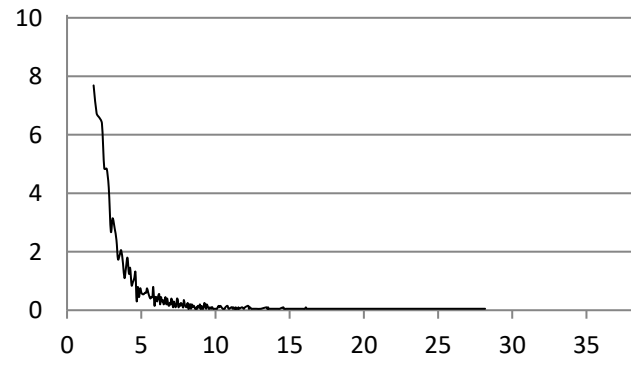
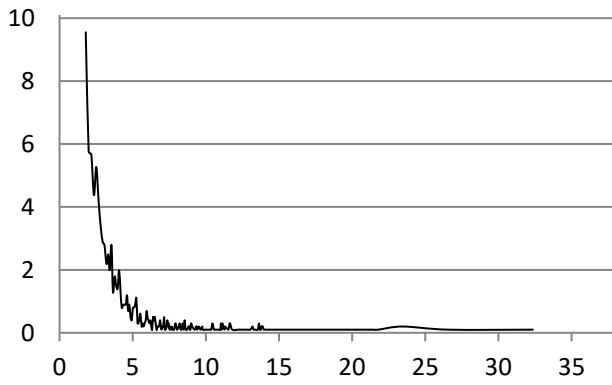
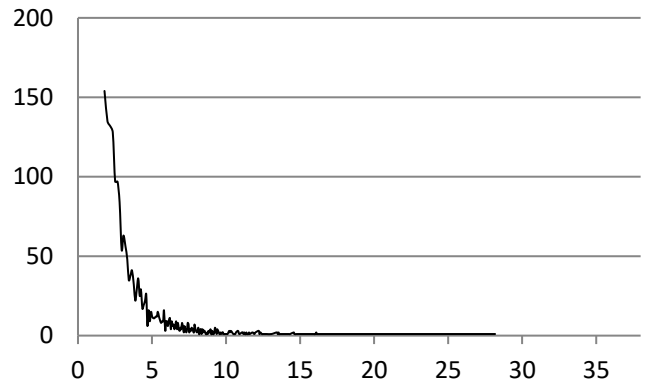
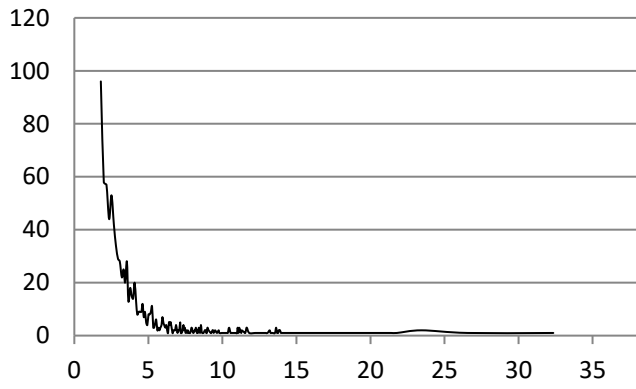
DN19

core depth: 203,58 m
total grain count: 1097
max grain size: 25.60 μm
mean grain size: 5.02 μm



DN20
 core depth: 207,37 m
 total grain count: 1005
 max grain size: 32.34 μm
 mean grain size: 4.83 μm

DN21
 core depth: 211,75 m
 total grain count: 2003
 max grain size: 28.15 μm
 mean grain size: 4.33 μm



Appendix D - XRD patterns

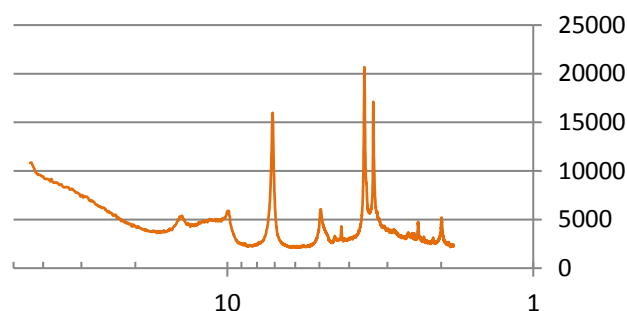
XRD diffraction patterns presented per sample. All data is presented according to the set-up described below and exemplified by sample DN01. Header includes sample name, core depth and lithostratigraphic association.

DN01
depth: 131,75 m
Whitby Mudstone Formation
Alum Shale Member - Main Alum Shales

Air-dried diffraction pattern

Measured: 2° to 50° 2θ / 44.16 to 1.82 Å

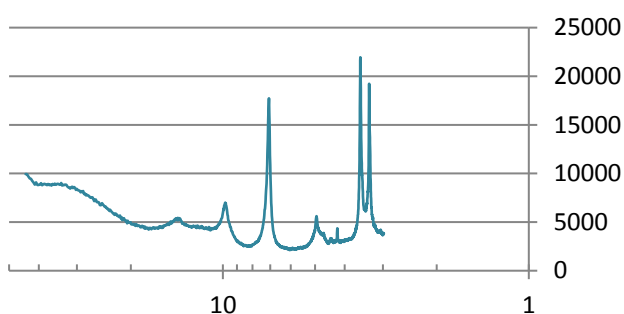
x-axis: d-spacing (Å) logarithmic scale
y-axis: count



Glycol solvated diffraction pattern

Measured: 2° to 30° 2θ / 44.16 to 2.98 Å

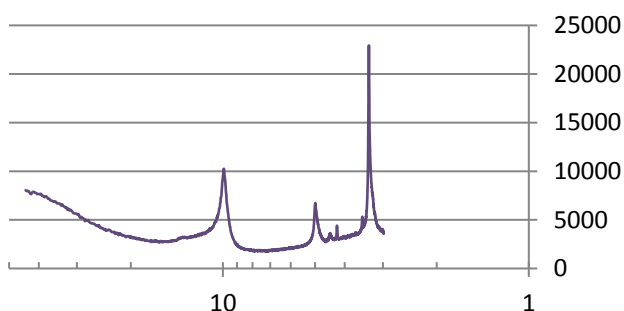
x-axis: d-spacing (Å) logarithmic scale
y-axis: count



Heated (550 °C) diffraction pattern

Measured: 2° to 30° 2θ / 44.16 to 2.98 Å

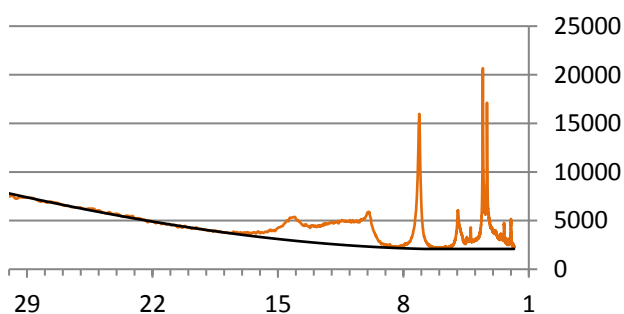
x-axis: d-spacing (Å) logarithmic scale
y-axis: count



Air-dried diffraction pattern plus background

Displayed on linear scale to highlight region of interest (approximately up to 20 Å)

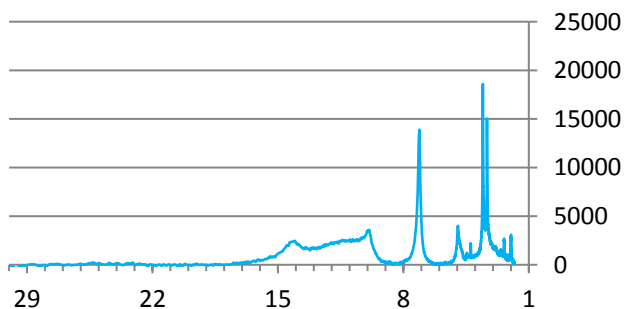
x-axis: d-spacing (Å) linear scale
y-axis: count



Background subtracted diffraction pattern

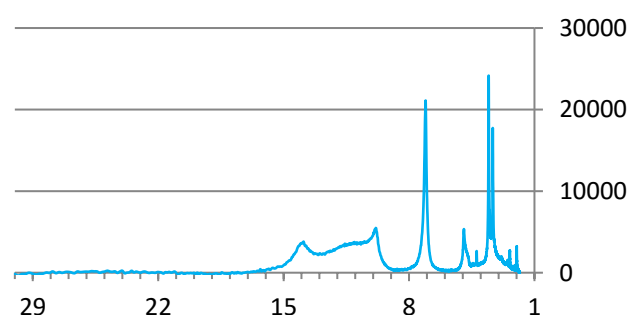
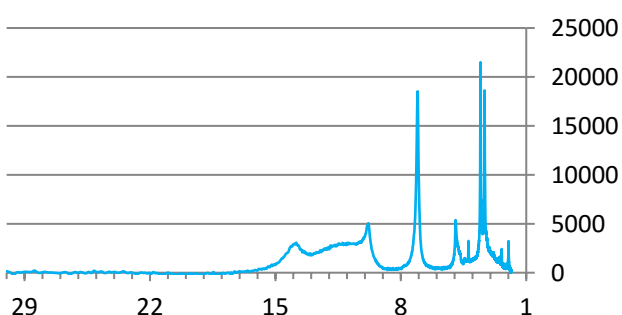
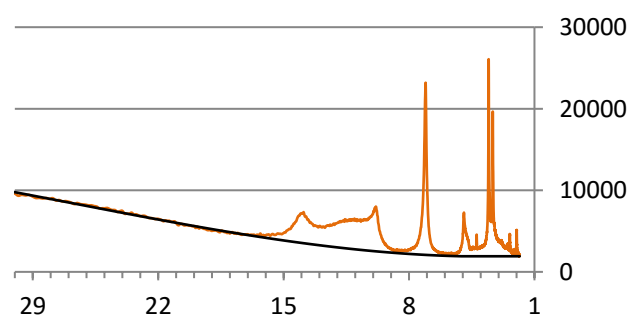
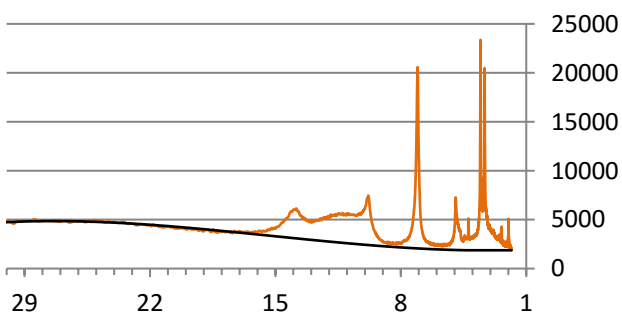
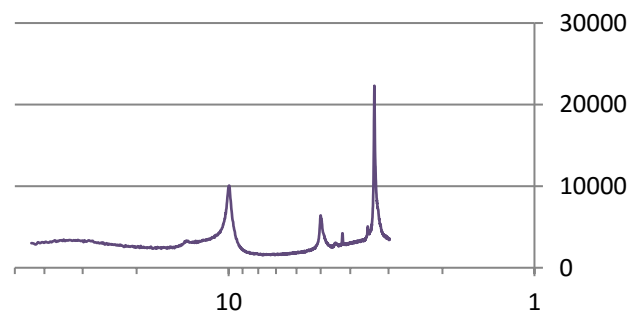
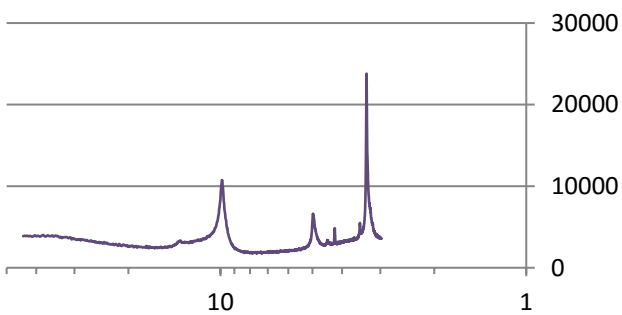
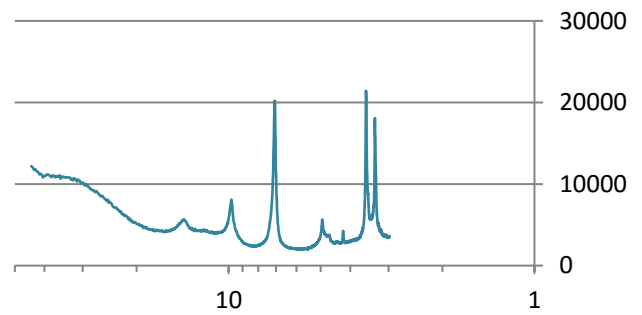
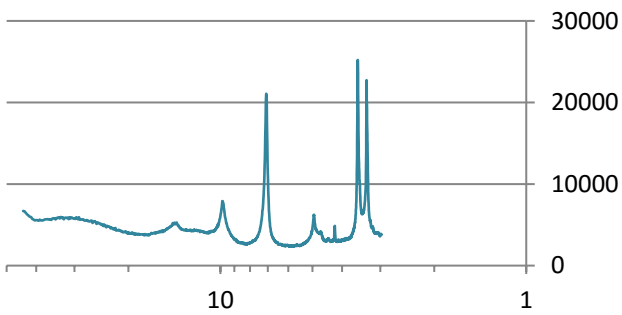
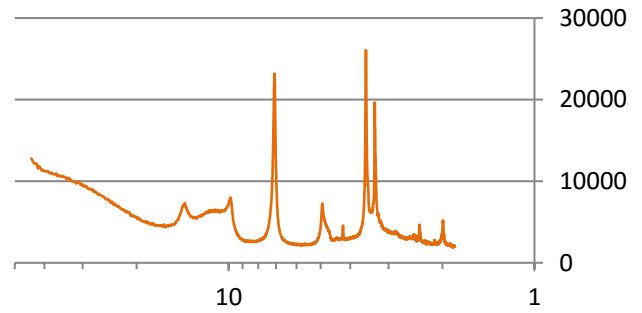
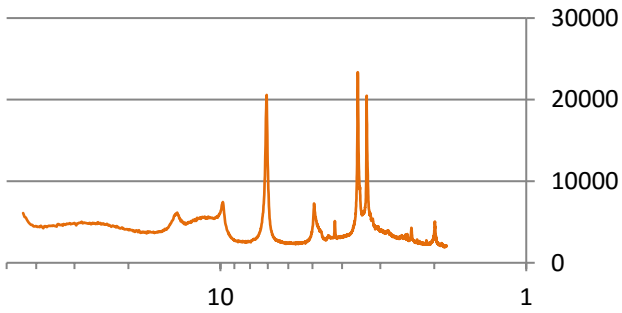
Edited data used for (semi-) quantitative analysis

x-axis: d-spacing (Å) linear scale
y-axis: count

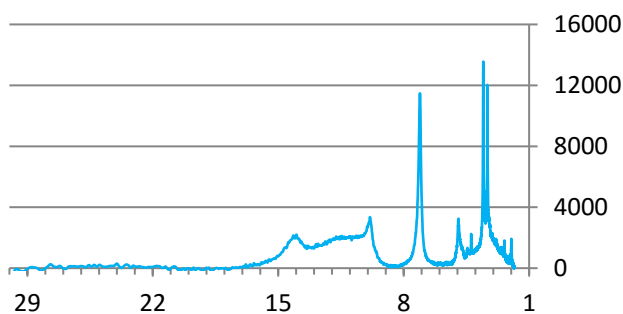
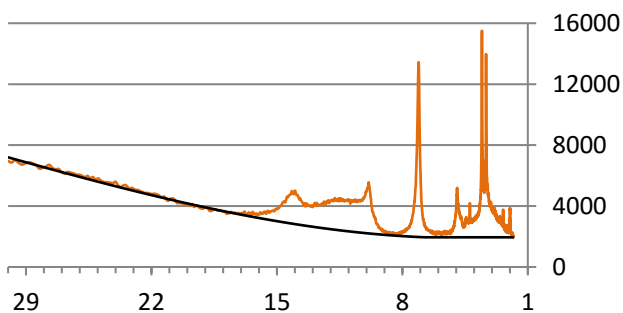
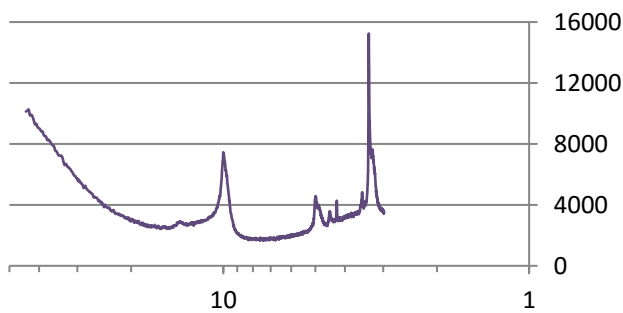
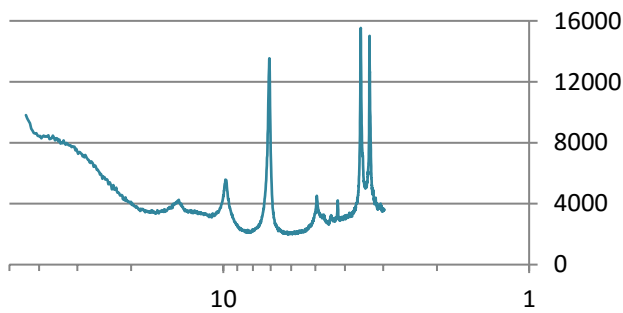
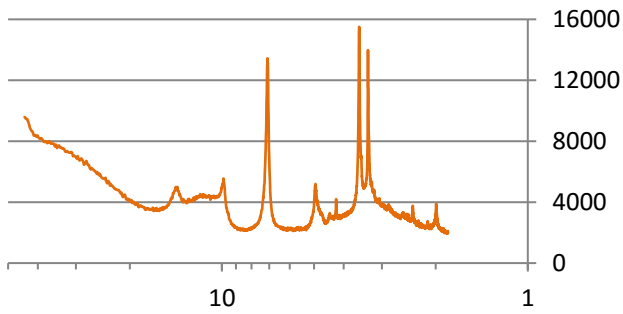


DN02
depth: 135,10 m
Whitby Mudstone Formation
Alum Shale Member - Hard Shales

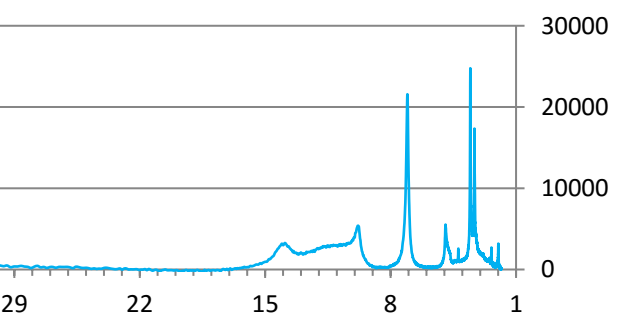
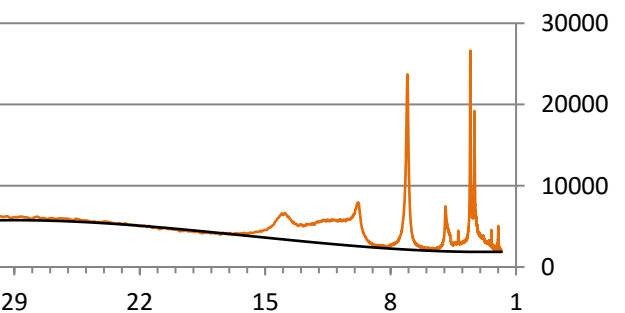
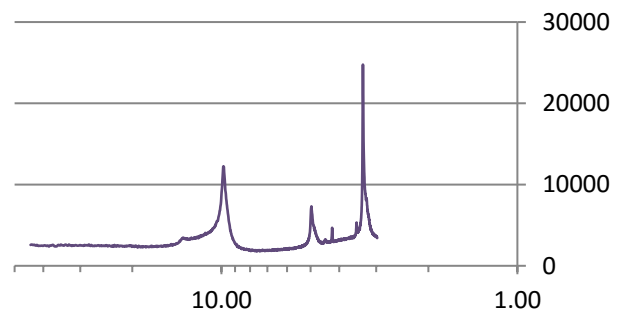
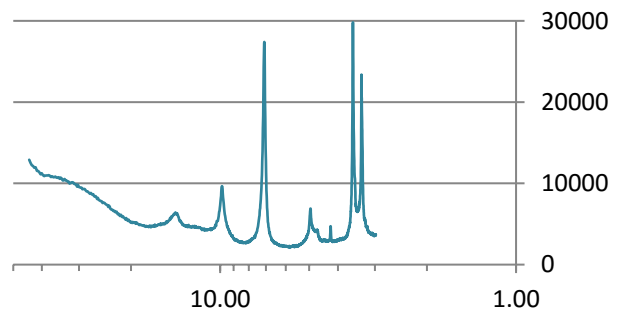
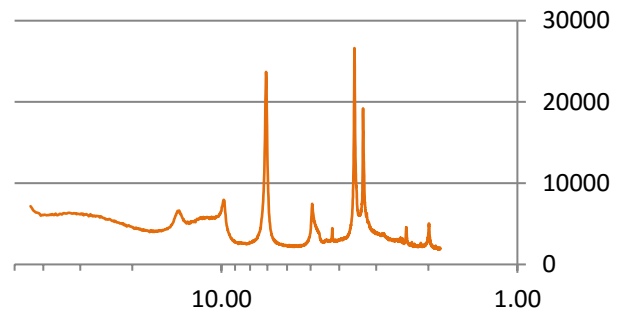
DN03
depth: 139,25 m
Whitby Mudstone Formation
Alum Shale Member - Hard Shales



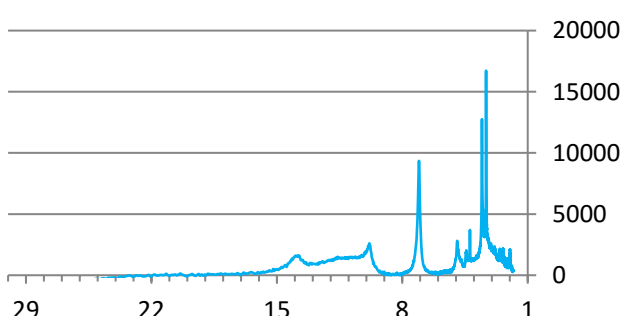
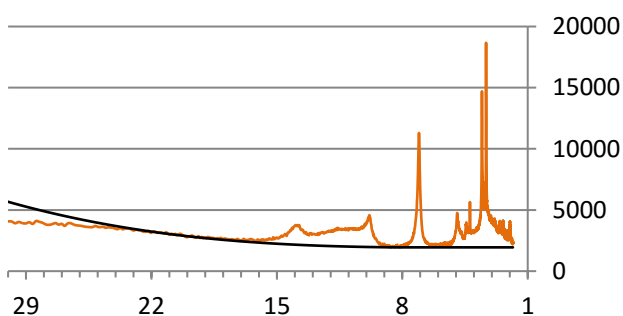
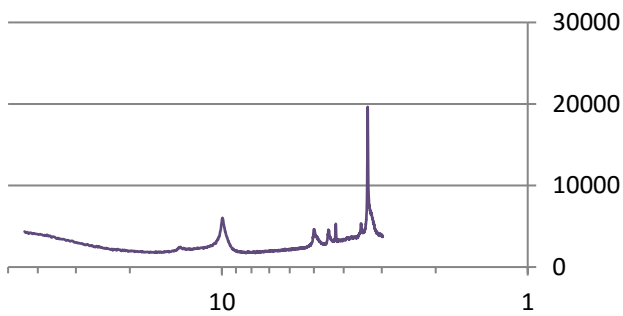
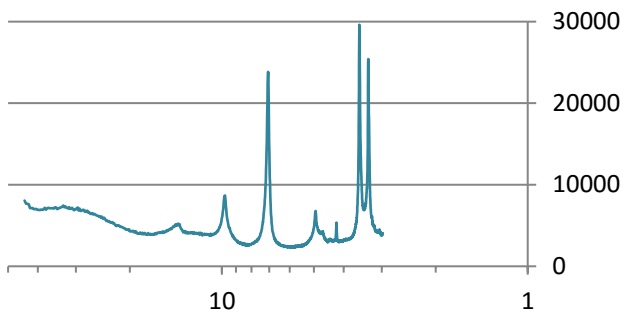
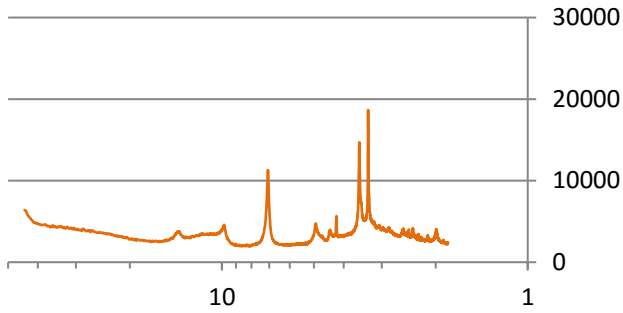
DN04
depth: 143,65 m
Whitby Mudstone Formation
Mulgrave Shale Member – Bituminous Shales



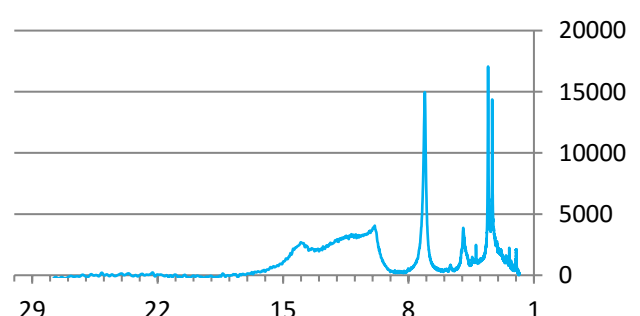
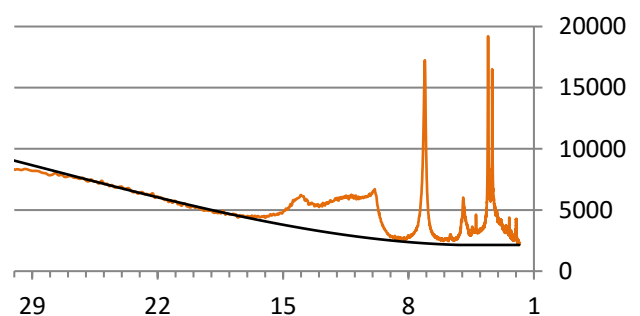
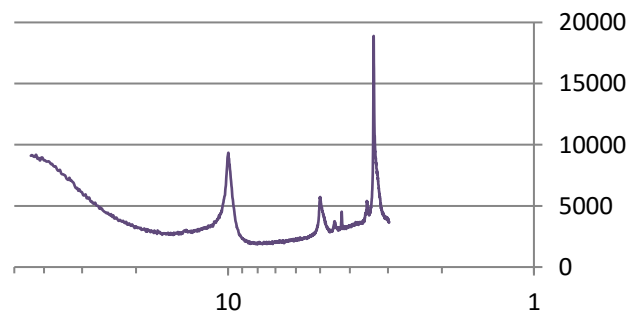
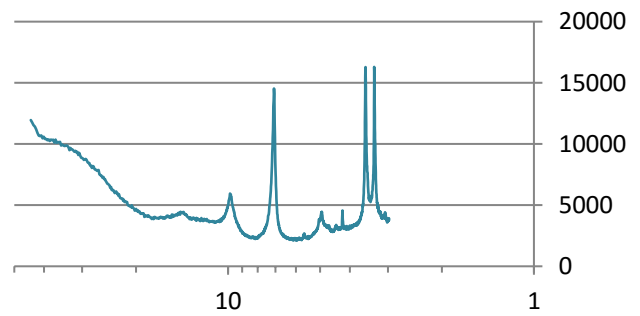
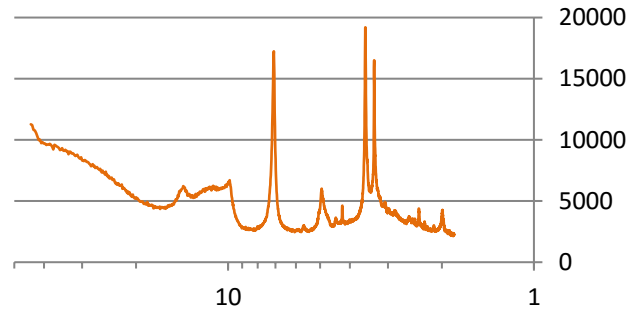
DN05
depth: 147,32 m
Whitby Mudstone Formation
Mulgrave Shale Member – Bituminous Shales



DN06
depth: 151,55 m
Whitby Mudstone Formation
Mulgrave Shale Member – Bituminous Shales

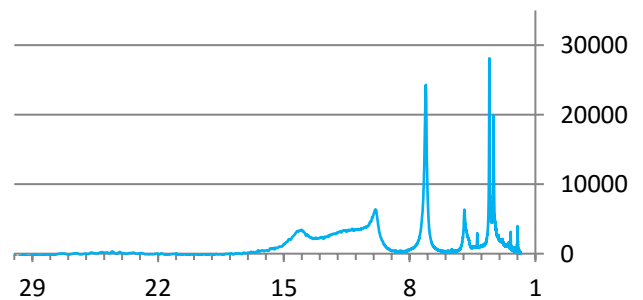
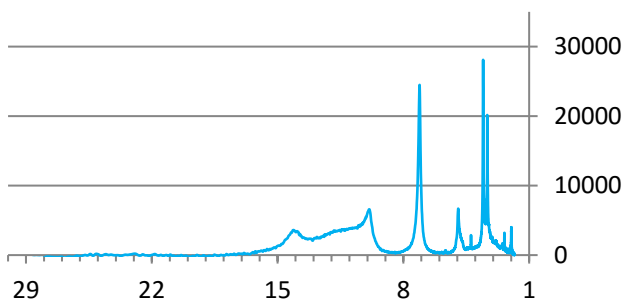
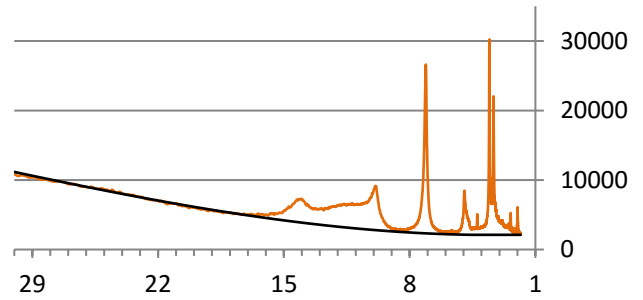
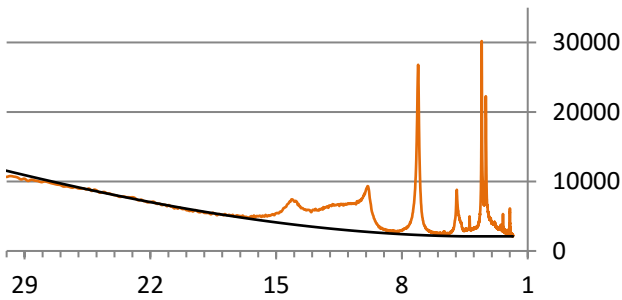
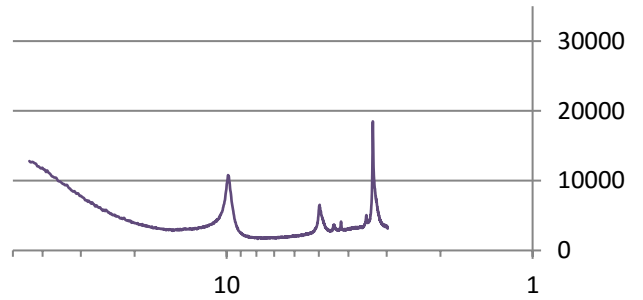
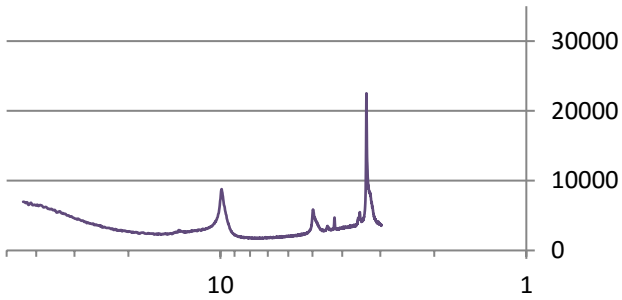
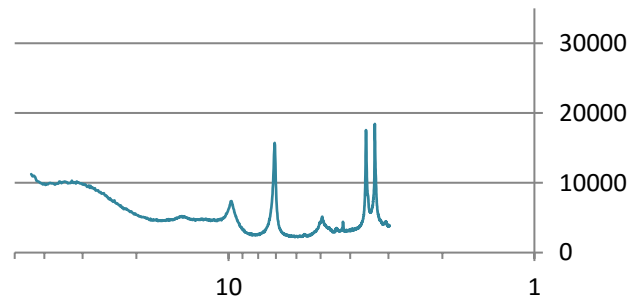
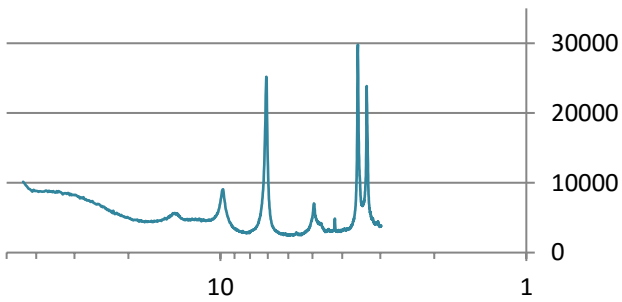
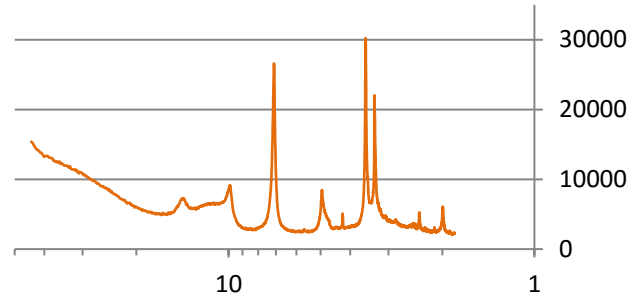
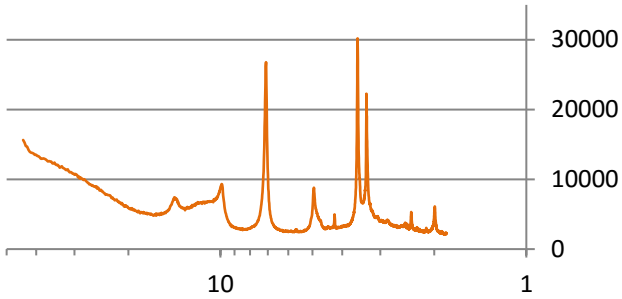


DN07
depth: 155,30 m
Whitby Mudstone Formation
Mulgrave Shale Member – Bituminous Shales



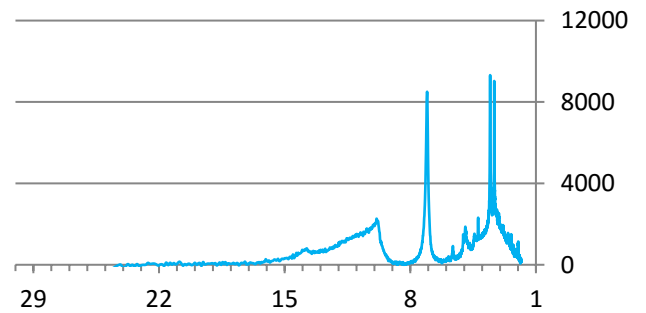
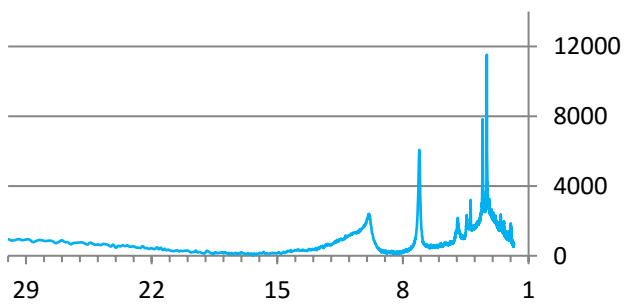
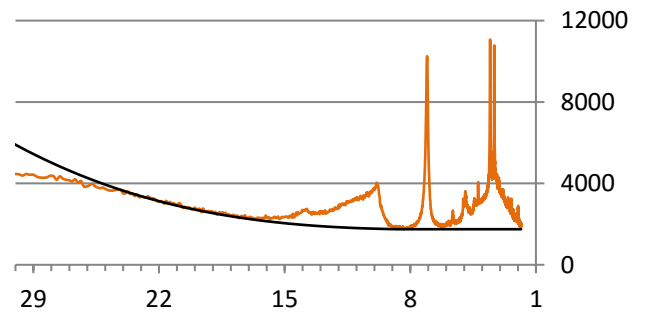
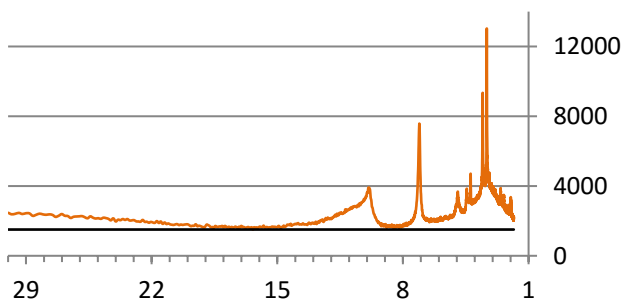
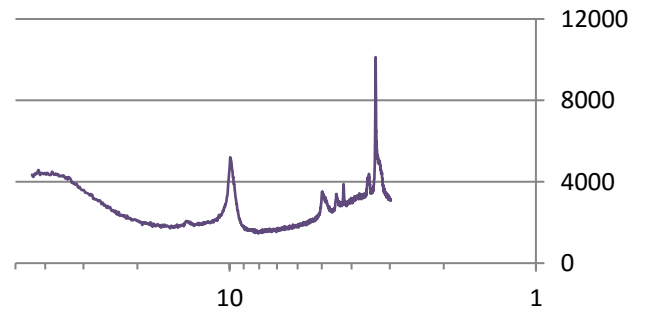
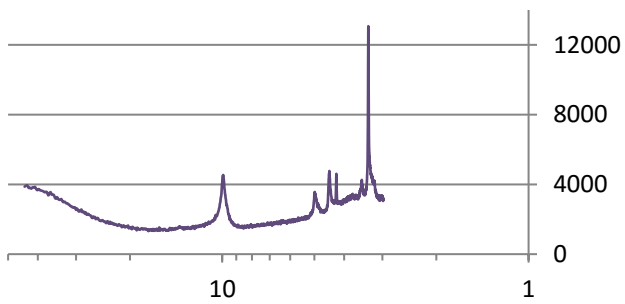
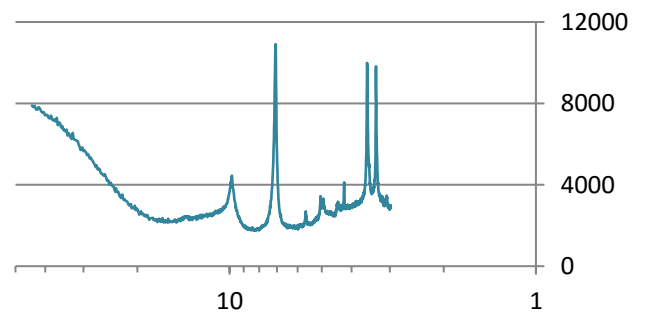
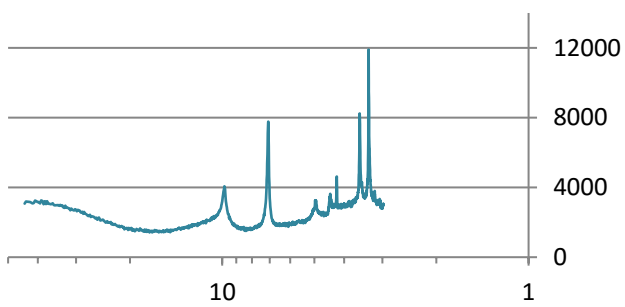
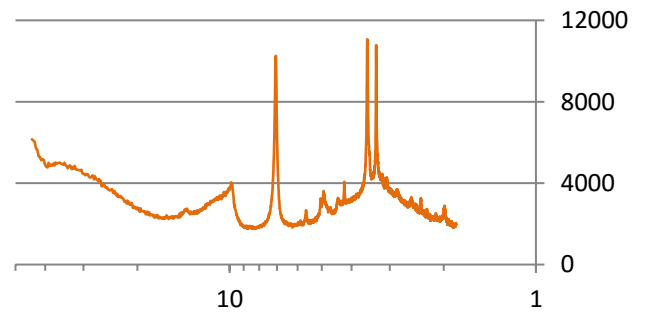
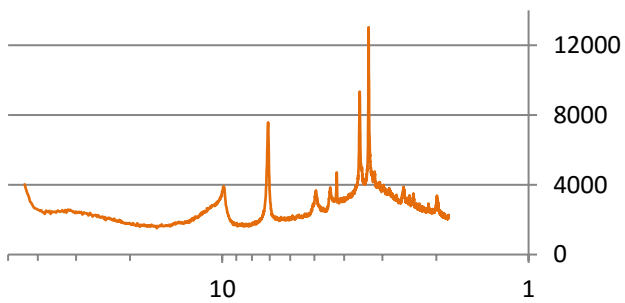
DN08
depth: 159,54 m
Whitby Mudstone Formation
Mulgrave Shale Member – Bituminous Shales

DN09
depth: 163,52 m
Whitby Mudstone Formation
Mulgrave Shale Member – Bituminous Shales



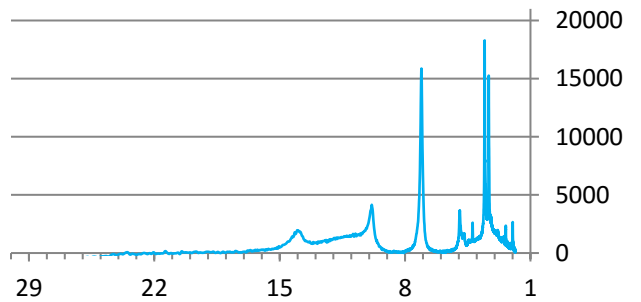
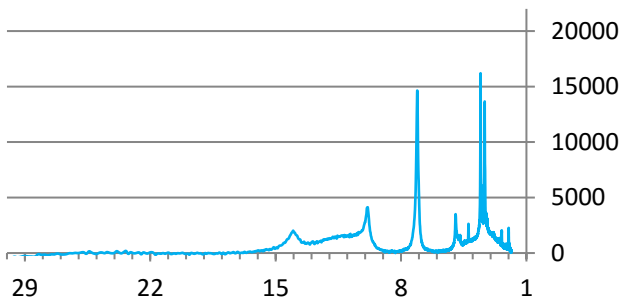
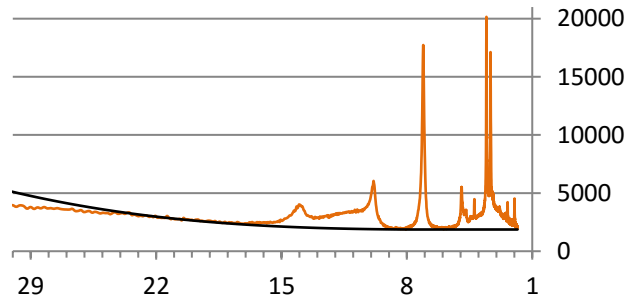
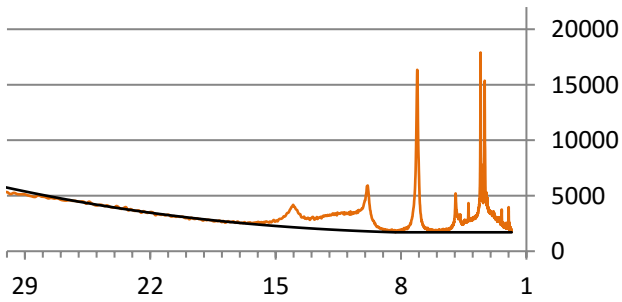
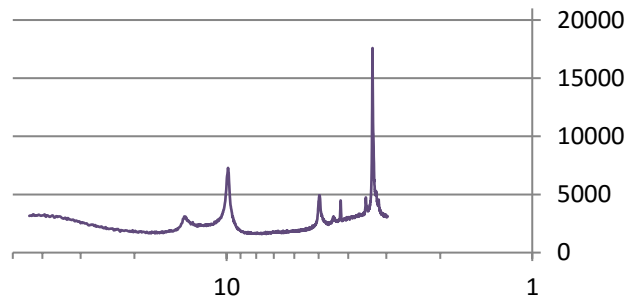
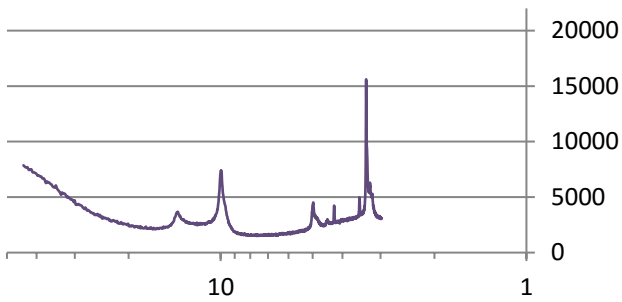
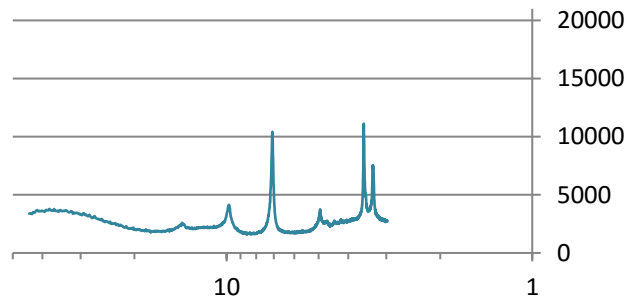
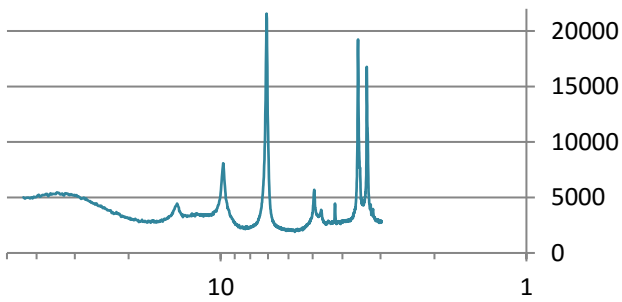
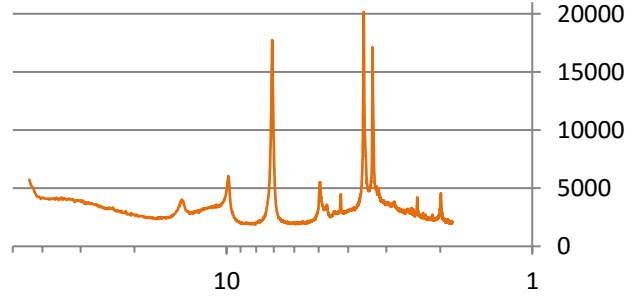
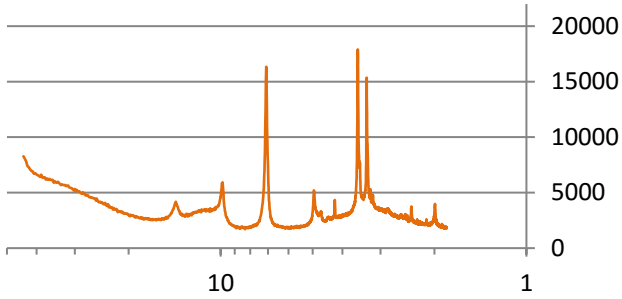
DN10
depth: 167,31 m
Whitby Mudstone Formation
Mulgrave Shale Member – Jet Rock

DN11
depth: 171,41 m
Whitby Mudstone Formation
Grey Shale Member



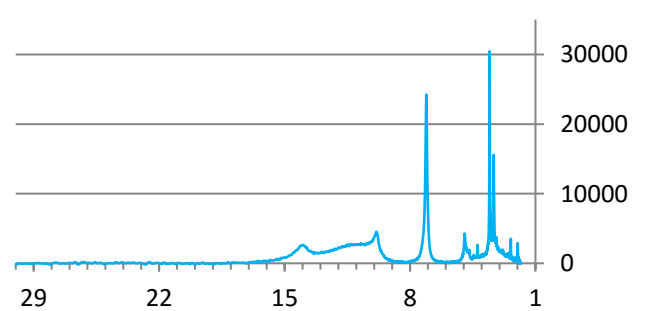
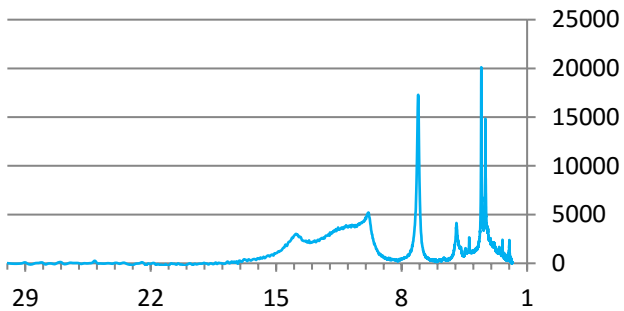
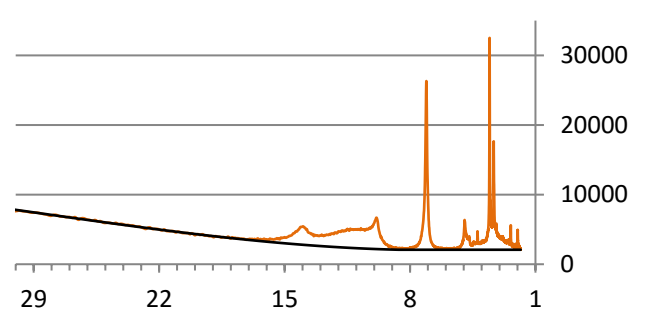
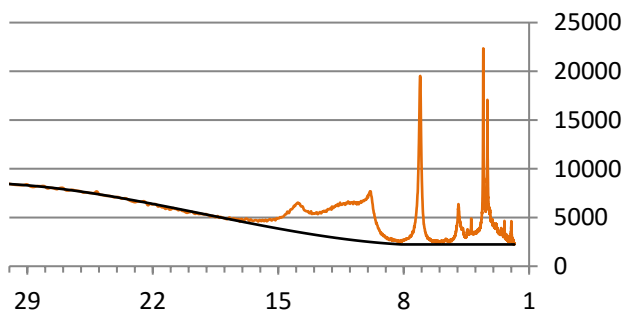
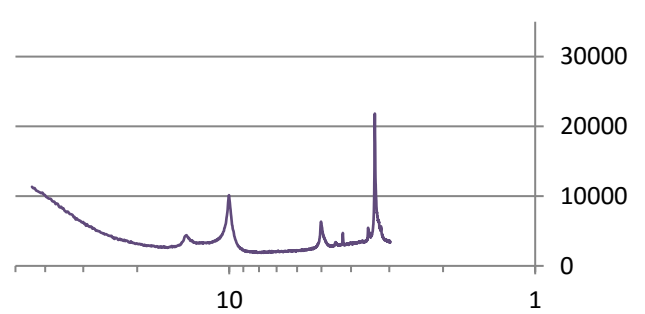
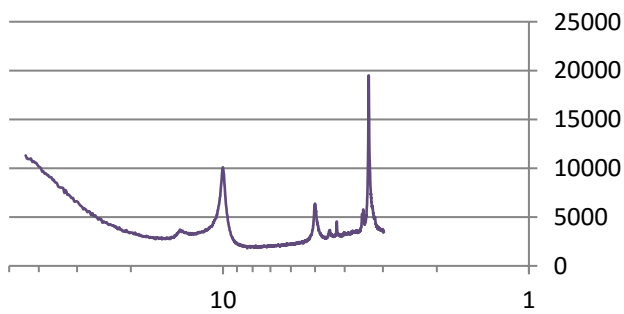
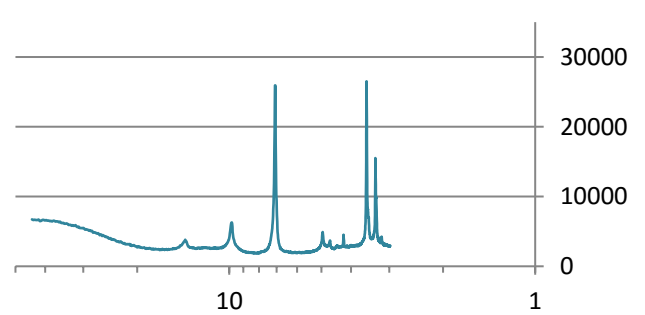
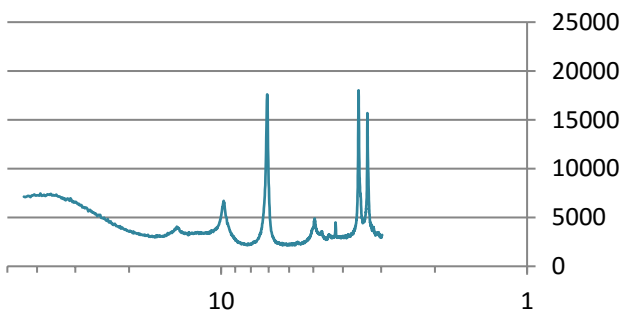
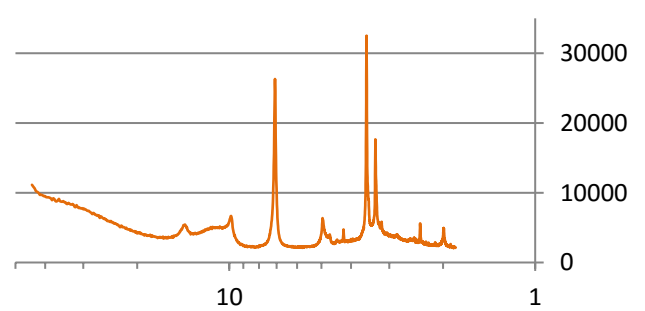
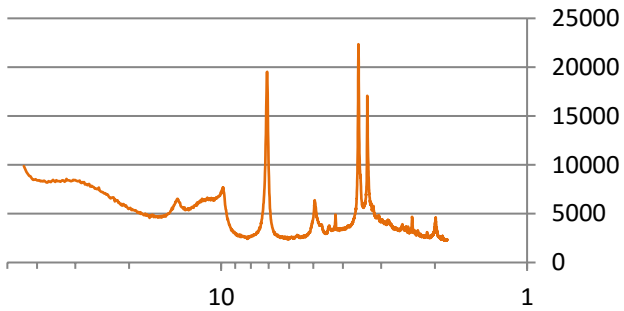
DN12
depth: 175,46 m
Whitby Mudstone Formation
Grey Shale Member

DN13
depth: 179,57 m
Whitby Mudstone Formation
Grey Shale Member



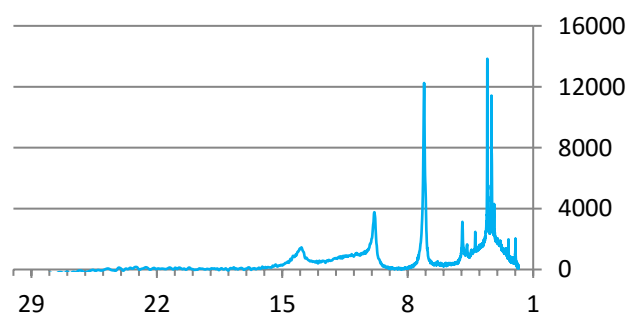
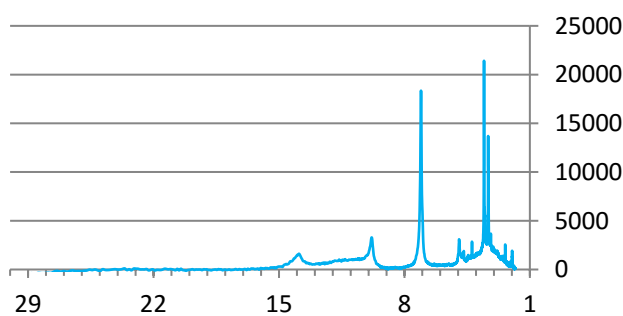
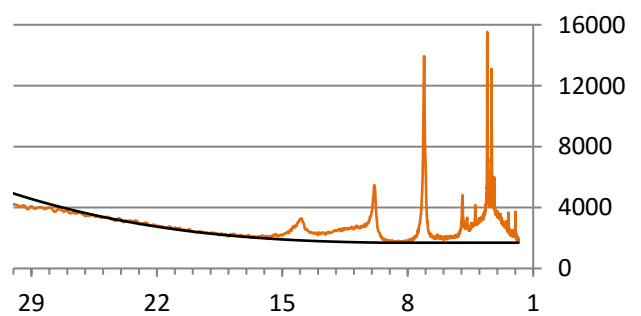
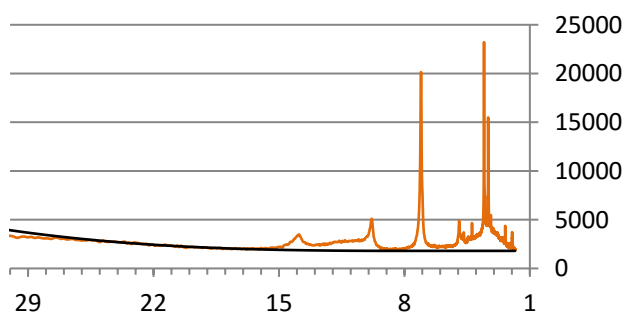
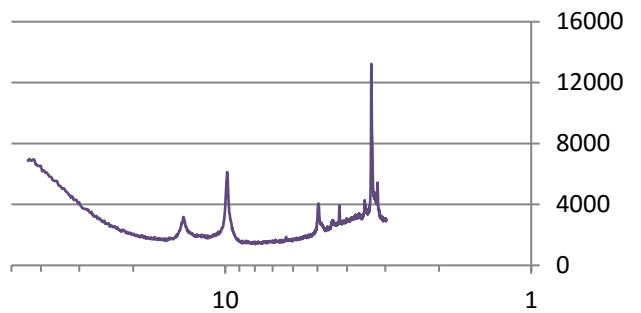
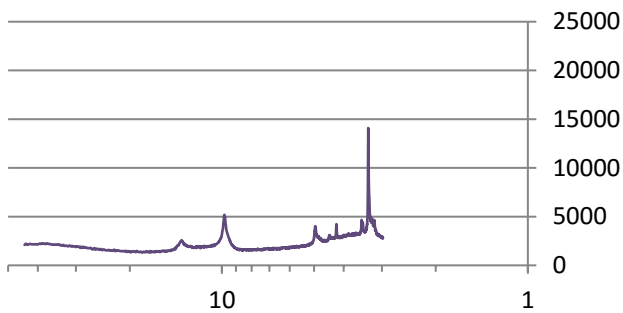
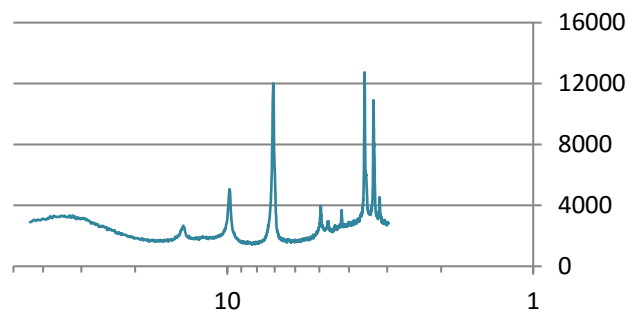
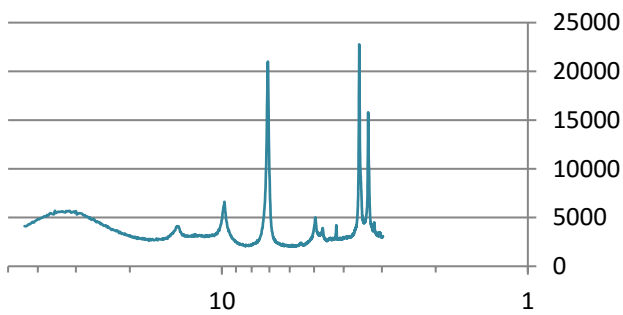
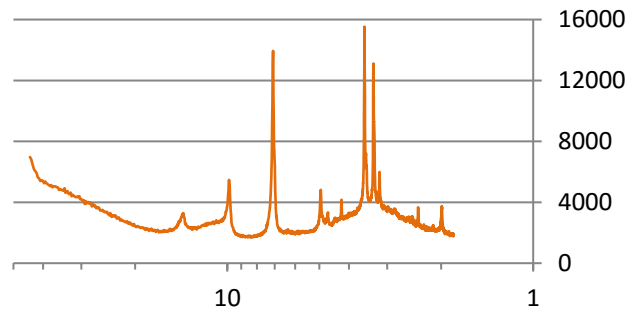
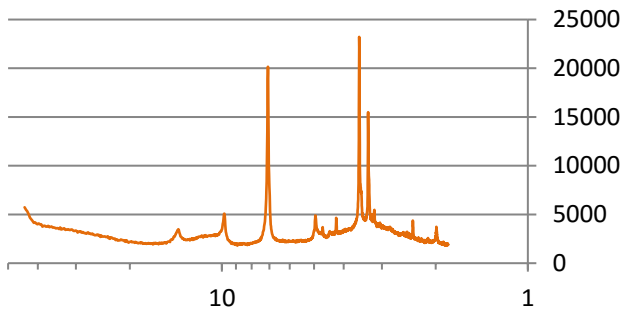
DN14
depth: 183,38 m
Whitby Mudstone Formation
Grey Shale Member

DN15
depth: 187,33 m
Cleveland Ironstone Formation
Kettleness Member



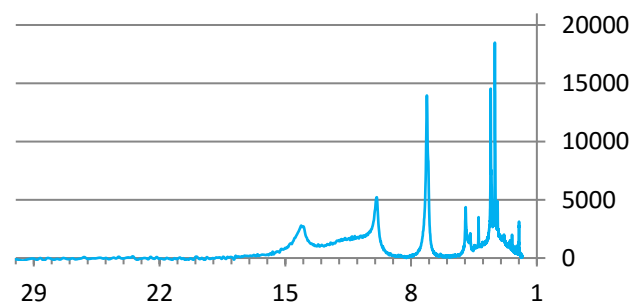
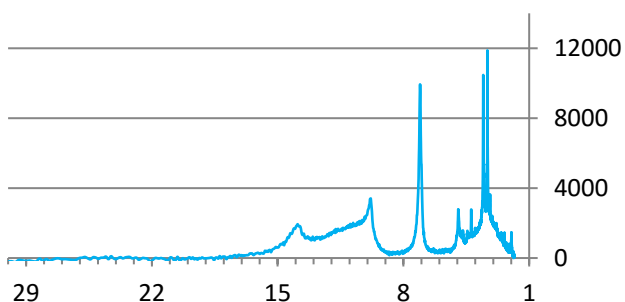
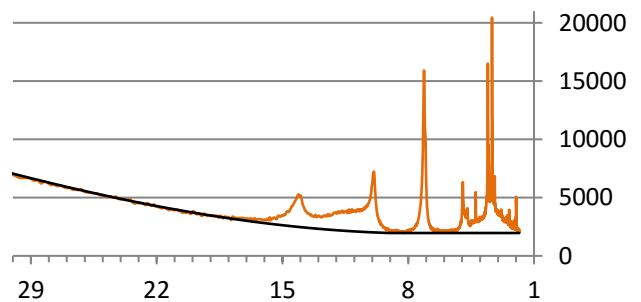
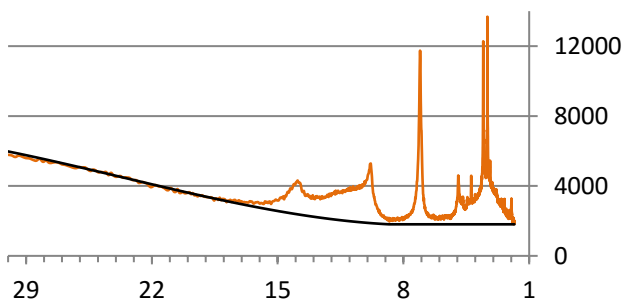
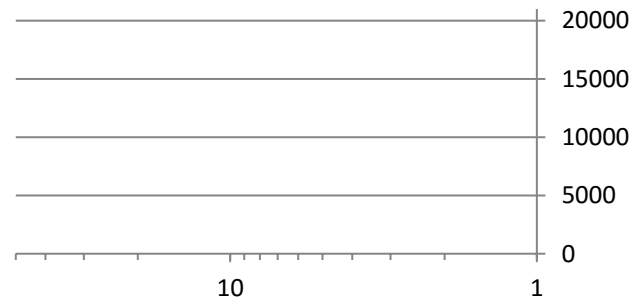
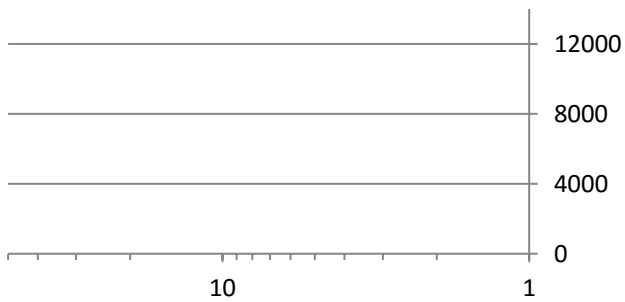
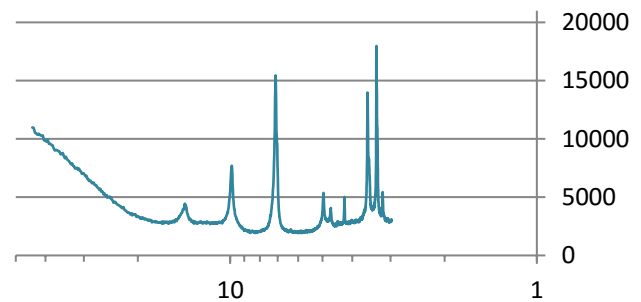
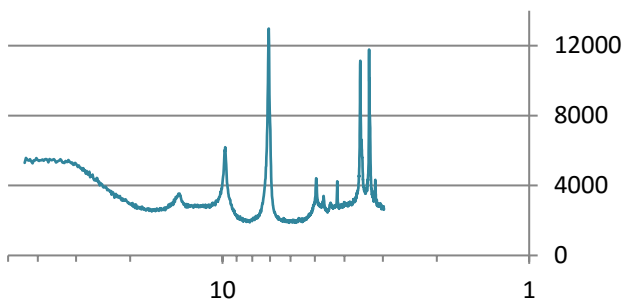
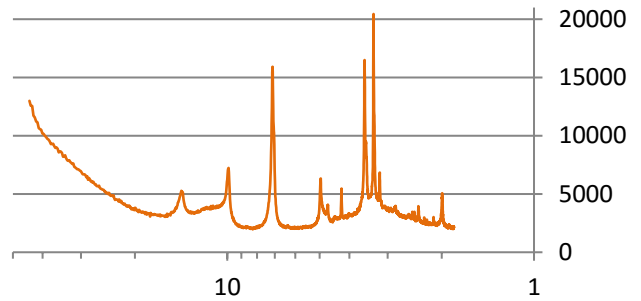
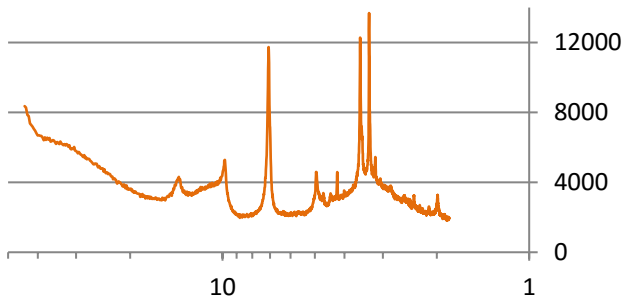
DN16
depth: 191,41 m
Cleveland Ironstone Formation
Kettleless Member

DN17
depth: 195,68 m
Cleveland Ironstone Formation
Penny Nab Member



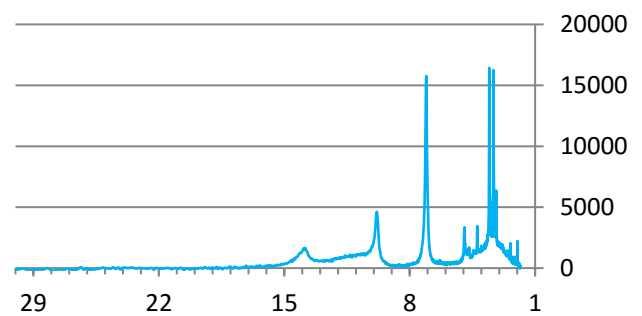
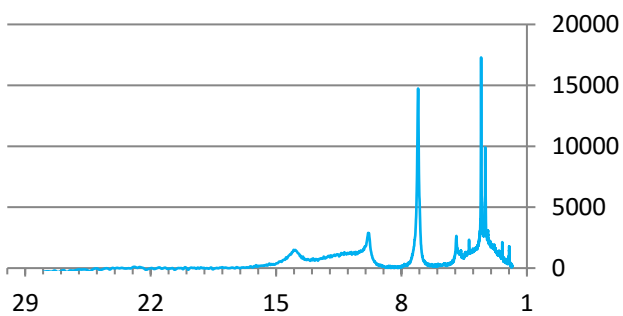
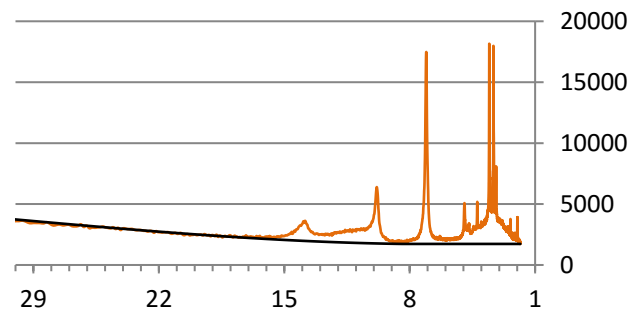
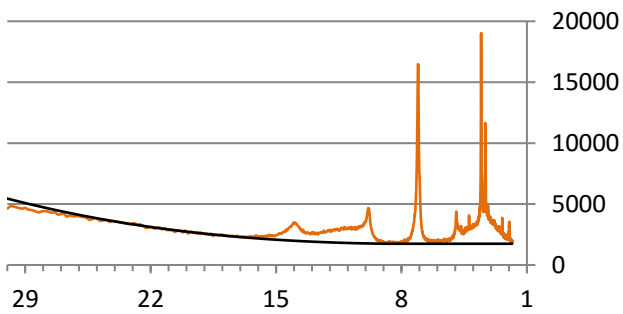
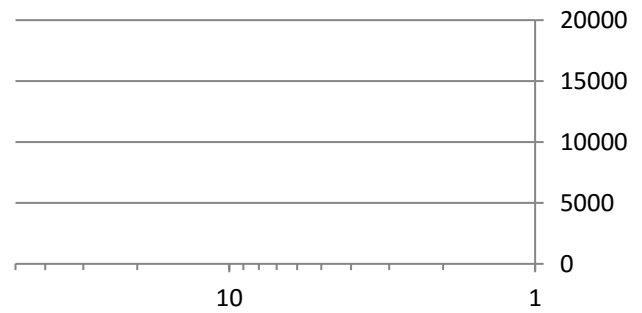
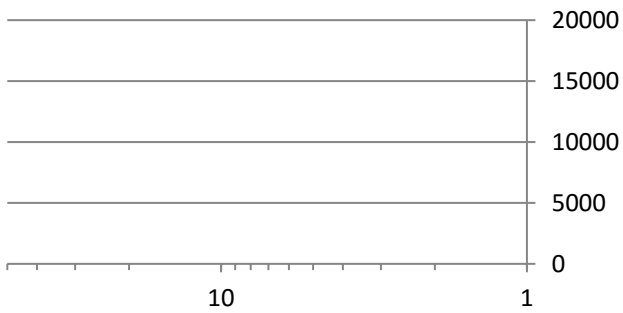
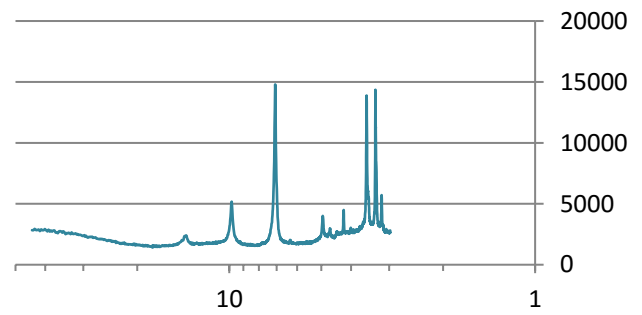
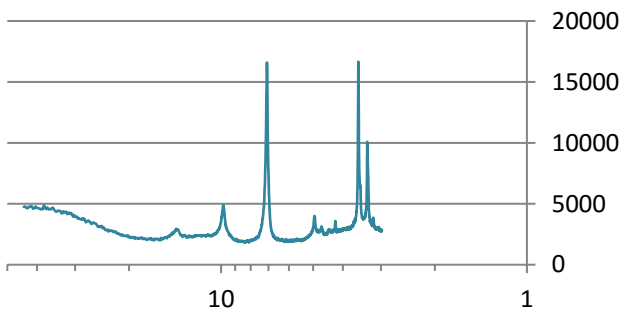
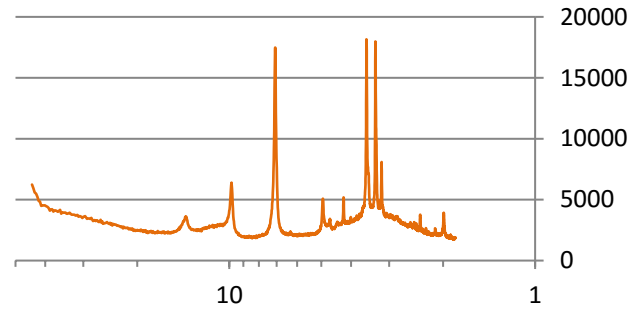
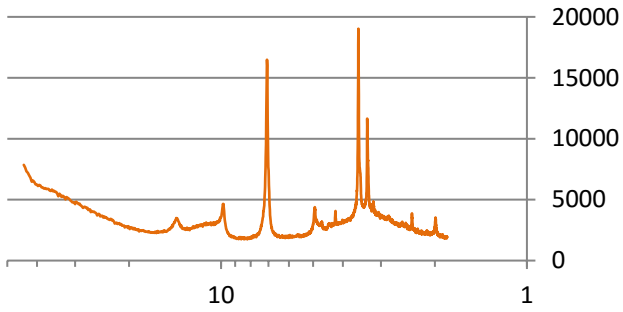
DN18
depth: 199,61 m
Cleveland Ironstone Formation
Penny Nab Member

DN19
depth: 203,58 m
Cleveland Ironstone Formation
Penny Nab Member



DN20
depth: 207,37 m
Cleveland Ironstone Formation
Penny Nab Member

DN21
depth: 211,75 m
Staithes Sandstone Formation



Appendix E - Summary of results

Quartz content and grain size distribution

Moments

depth	area % qtz	mean size (µm)	% clay	% very fine	% fine	% medium	% coarse	grain count	mean size	mean size	standard	skewness	kurtosis	mean
									(Φ)	(Φ → µm)	deviation			cubed
130.75	7.07	4.39	54.53	36.77	8.14	0.56	0	1610	8.26	3.26	1.29	0.93	3.56	3.94
135.10	7.33	4.22	59.03	31.69	8.89	0.40	0	1767	8.36	3.05	1.33	0.87	3.24	4.10
139.25	11.77	3.88	63.81	30.23	5.61	0.36	0	3368	8.50	2.76	1.36	0.87	3.01	4.41
143.65	7.90	3.83	64.14	30.42	5.10	0.34	0	2334	8.54	2.69	1.39	0.86	2.91	4.56
147.32	8.89	3.70	66.00	29.42	4.50	0.07	0	2753	8.57	2.63	1.37	0.88	2.94	4.53
151.55	13.18	3.74	66.50	27.85	5.48	0.15	0.02	4033	8.56	2.65	1.35	0.86	2.99	4.27
155.3	8.48	3.40	72.89	24.29	2.74	0.09	0	3290	8.69	2.42	1.35	0.89	2.92	4.36
159.54	10.48	3.63	68.42	27.33	4.20	0.06	0	3480	8.58	2.62	1.33	0.91	3.09	4.28
163.52	14.45	3.98	63.25	29.55	6.71	0.46	0.03	3712	8.46	2.84	1.35	0.85	3.11	4.17
167.31	6.46	4.40	58.45	30.69	9.73	1.13	0	1326	8.28	3.23	1.27	0.83	3.52	3.42
171.41	6.29	4.61	54.70	32.14	12.16	1.00	0	1201	8.24	3.31	1.34	0.82	3.24	3.97
175.46	8.66	4.45	58.60	28.25	11.93	1.23	0	1710	8.34	3.08	1.41	0.77	2.91	4.25
179.57	7.27	4.84	55.45	30.26	12.09	2.20	0	1183	8.24	3.31	1.43	0.73	2.91	4.24
183.38	8.09	5.76	50.30	26.25	18.83	4.62	0	823	8.13	3.57	1.62	0.62	2.36	5.29
187.33	8.17	5.20	56.73	25.10	13.55	4.62	0	996	8.21	3.37	1.48	0.59	2.61	3.83
191.41	14.87	5.37	59.75	23.31	11.09	5.01	0.85	1416	8.33	3.10	1.63	0.52	2.23	4.57
195.68	8.88	5.62	49.37	27.67	19.08	3.35	0.52	954	8.14	3.53	1.60	0.64	2.40	5.26
199.61	8.31	4.32	56.92	33.72	8.72	0.63	0	1892	8.32	3.13	1.34	0.89	3.32	4.27
203.58	7.29	5.02	53.69	29.08	14.86	2.37	0	1097	8.24	3.31	1.51	0.70	2.61	4.83
207.37	6.57	4.83	57.91	26.87	12.24	2.89	0.10	1005	8.34	3.09	1.55	0.66	2.47	4.86
211.75	9.97	4.33	60.71	28.66	9.19	1.45	0	2003	8.37	3.02	1.37	0.77	3.01	3.98

XRD (semi-) quantitative results

Depth (m)	PIHR (Peak-area Integration with Height Ratios) method				PHHW (Peak-Height Half-Width) method			
	% kaolinite	% interstratified	% illite	% vermiculite	% kaolinite	% interstratified	% illite	% vermiculite
131.75	23.46	76.54	45.32	31.22	29.35	70.65	22.56	48.08
135.10	26.70	73.30	45.64	27.67	31.37	68.63	19.73	48.91
139.25	25.53	74.47	43.86	30.61	31.86	68.14	20.92	47.22
143.65	24.56	75.44	45.63	29.81	29.91	70.09	19.13	50.95
147.32	27.99	72.01	44.87	27.14	35.51	64.49	19.81	44.69
151.55	24.71	75.29	46.47	28.82	34.46	65.54	20.78	44.76
155.30	22.64	77.36	46.52	30.84	30.55	69.45	25.27	44.18
159.54	26.17	73.83	47.74	26.09	36.88	63.12	25.70	37.42
163.52	26.68	73.32	47.59	25.74	32.49	67.51	22.42	45.09
167.31	26.81	73.19	63.35	9.85	36.99	63.01	41.04	21.97
171.41	26.75	73.25	54.20	19.05	38.66	61.34	30.25	31.09
175.46	28.22	71.78	48.20	23.58	36.75	63.25	31.19	32.07
179.57	29.74	70.26	47.70	22.57	36.23	63.77	30.21	33.56
183.38	20.74	79.26	50.11	29.14	28.89	71.11	23.87	47.24
187.33	27.12	72.88	45.85	27.04	38.22	61.78	20.22	41.56
191.41	39.91	60.09	40.21	19.88	42.76	57.24	23.87	33.38
195.68	32.99	67.01	48.32	18.69	38.61	61.39	28.42	32.97
199.61	23.75	76.25	48.62	27.62	31.71	68.29	19.49	48.80
203.58	24.19	75.81	49.42	26.40	33.69	66.31	28.76	37.55
207.37	32.68	67.32	44.35	22.98	37.61	62.39	28.40	33.99
211.75	35.64	64.36	47.41	16.95	42.13	57.87	27.94	29.93